

DETERMINATION OF PROTON RADII OF NEUTRON-RICH
OXYGEN ISOTOPES FROM CHARGE-CHANGING CROSS
SECTION MEASUREMENTS

by

Satbir Kaur

Submitted in partial fulfillment of the requirements
for the degree of Doctor of Philosophy

at

Dalhousie University
Halifax, Nova Scotia
July 2018

© Copyright by Satbir Kaur, 2018

dedicated to my parents

Table of Contents

List of Tables	v
List of Figures	x
Abstract	xi
Acknowledgements	xii
Chapter 1 Introduction	1
1.1 Exotic phenomena of neutron-rich nuclei: halos and skin	4
1.1.1 Neutron halos	4
1.1.2 Neutron skin	5
1.2 Motivation to study proton radii of $^{16-24}\text{O}$	6
1.2.1 Drip line of oxygen isotopes and $3N$ forces	7
1.2.2 Proton radii: A test for <i>ab initio</i> approaches	10
1.2.3 The shell evolution in oxygen isotopes	10
1.2.4 Neutron skin in oxygen isotopes	14
1.3 Conventional methods to determine proton radii	14
1.3.1 Electron scattering	14
1.3.2 Isotope shift	16
1.3.3 Muonic Atom X-Ray Spectroscopy	17
1.4 Charge-changing cross section measurement	18
1.5 Finite range Glauber model	19
1.5.1 R_p determined from σ_{cc}	20
1.6 This Work	21
Chapter 2 Experiment Description	22
2.1 The fragment separator	22
2.2 Principle of measuring charge-changing cross section	27
2.3 The detector setup	28
2.3.1 Multiple-sample ionization chambers	29
2.3.2 Time projection chambers	31
2.3.3 Plastic scintillators	33
2.3.4 Veto scintillator	33

Chapter 3	Data Analysis	35
3.1	Detector calibration	35
3.1.1	Calibration of the MUSIC detectors	35
3.1.2	Time of flight calibration	36
3.1.3	TPC calibration	41
3.2	Particle identification	43
3.2.1	Location of focal planes	44
3.3	Incident beam selection	49
3.4	Z identification after the target	50
3.5	The target position dependence of transmission ratios	52
Chapter 4	Discussion	55
4.1	The transmission ratios and σ_{cc}	55
4.2	Uncertainty of the measured cross section	58
4.2.1	Statistical uncertainty	59
4.2.2	Uncertainty from contaminants in the same Z events after the target	60
4.3	Secondary beam energies	61
4.4	MUSIC42 detection efficiency correction	62
4.5	Table of charge-changing cross sections	64
4.6	Proton radii determination	64
4.7	Discussion of results	66
4.7.1	Comparison with theory	68
4.8	Neutron skin thickness determination	71
4.9	Summary	72
Bibliography		75

List of Tables

Table 2.1	The beam intensity for each fragment setting of the FRS. . . .	26
Table 3.1	The parameters for TAC calibration for the Scintillator detectors.	40
Table 3.2	The position calibration parameters for anodes and delay lines of TPC ₁₋₆	43
Table 4.1	The measured σ_{cc} of $^{16,18-24}\text{O}$ with statistical uncertainties. . . .	57
Table 4.2	The energy losses in materials placed between SC41 and the carbon reaction target at F4.	62
Table 4.3	The MUSIC42 detection efficiency corrections to σ_{cc} for $^{16-18,24}\text{O}$.	63
Table 4.4	The measured σ_{cc} with the uncertainties and secondary beam energies in front of the target.	64
Table 4.5	The measured R_p^{cc} of $^{16-18,24}\text{O}$ extracted from the measured σ_{cc} . The $R_p^{(e^-)}$ for $^{16-18}\text{O}$ are from Ref. [37].	66

List of Figures

Figure 1.1	Mayer-Jensen’s shell model scheme predicted with harmonic oscillator potential and the spin-orbit force [6, 7]. Figure adapted from [8].	2
Figure 1.2	The nuclear landscape where each square represents a nucleus. The valley of stability is shown by black, unstable nuclei are represented by yellow and green region shows theoretically predicted bound nuclei.	3
Figure 1.3	(a) A schematic illustration of neutron skin. (b) ΔR_{rms} as a function of ΔE_F of various isotopes obtained by the RMF Model. The empirical values are shown in shadowed boxes. Right figure adapted from [22].	6
Figure 1.4	Chiral effective field theory for nuclear forces. The different contributions at successive orders are shown diagrammatically. Nucleons and pions are represented by solid and dashed lines, respectively. Figure adapted from [26].	8
Figure 1.5	(a) The binding energies (b) R_p from Ref. [34] using the $NNLO_{sat}$ interaction (red symbols) and the EM interaction (black symbols) calculated in three different many-body approaches. The blue stars are R_p from Ref. [27] calculated using coupled-cluster calculations. The experimental R_p derived from the e^- scattering experiments [37] are shown by blue open circles.	9
Figure 1.6	One-neutron separation energy for different isospin chains. Figure taken from [39].	11
Figure 1.7	The shell model scheme of ^{24}O	11
Figure 1.8	(a) The first excited stated of different isotopes plotted as a function of the neutron number. Figure taken from [40]. (b) The one-neutron knockout cross sections and widths of the fragment longitudinal-momentum distributions as a function of the neutron number. Figure taken from [47]	13
Figure 1.9	The neutron skin calculated using the calculated R_p and R_m . The plusses represent ΔR calculated using radii with IMSRG many-body approach with EM interaction (black) and $NNLO_{sat}$ interaction (red), taken from Ref. [34]. The stars represent ΔR found from the radii calculated with coupled-cluster calculations from Ref. [27].	15

Figure 1.10	The radii of point nucleon distribution in (a) Li isotopes (b) He isotopes (c)Be isotopes. Figures adapted from [68].	17
Figure 1.11	(a) The measured R_m (circles) and measured R_p^{cc} (triangles) for $^{12-17}\text{B}$ (b) The measured R_m (open circles) and measured R_p^{cc} (filled circles) for $^{12-19}\text{C}$. The blue symbols represent the measured R_p derived from e^- scattering. Figure taken from [82,84].	21
Figure 2.1	The schematic view of the GSI-FRS facility. Figure from [88].	22
Figure 2.2	A photograph of FRS at GSI.	23
Figure 2.3	The schematic view of ion optics of the FRS.	25
Figure 2.4	The position distributions in x of the various isotopes at the F4 using the LISE code (a) without degrader (b) with a wedge degrader.	26
Figure 2.5	(a) A schematic view of the experimental setup at the FRS with the detector arrangement at the final focus F4. Fig. taken from [82].(b)A flowchart of measurements performed with the different detectors.	29
Figure 2.6	The detector setup at F2 and F4 with detector distances.	29
Figure 2.7	A picture of the MUSIC detector (left). Schematic view of the MUSIC detector (right).	30
Figure 2.8	A picture of the detector on the left. A schematic view of a Time-Projection Chamber (TPC) (right). Figure adapted from [94].	31
Figure 2.9	The control sum distribution using the delay line 1 and anode 1 for TPC6.	32
Figure 2.10	A photograph of the veto plastic scintillator.	34
Figure 2.11	The energy loss in left PMT of the veto detector.	34
Figure 3.1	(a) The uncalibrated MUSIC41 spectrum for the ^{12}C secondary beam. Each peak is fitted with a Gaussian function (red curve). (b) A linear fit of Z^2 versus the mean channel number of the peaks. (c) The calibrated Z spectrum of the MUSIC41 detector.	36

Figure 3.2	(a) The uncalibrated MUSIC42 spectrum for the ^{12}C setting. Each peak is fitted with a Gaussian function (red curve). (b) A linear fit of Z^2 versus the mean channel number of the peaks. (c) The calibrated Z spectrum of the MUSIC42 detector.	37
Figure 3.3	The TAC spectrum for 10 ns pulses from the TAC calibrator (a) TOF_{RR} in channels (R_C) (b) TOF_{LL} in channels (L_C).	38
Figure 3.4	(a) The linear fit of R_{ns} (TOF_{RR} in ns) versus mean R_C (TOF_{RR} in channels). (b) The linear fit of L_{ns} (TOF_{LL} in ns) versus mean L_C (TOF_{LL} in channel).	39
Figure 3.5	Linear fit of $TOF \times \beta$ versus β . The slope of the linear fit is the TOF offset (O) and intercept (S) is the flight path.	40
Figure 3.6	The scheme of scintillator plastic fibers used for the calibration of TPCs.	41
Figure 3.7	(a) The TPC delay line 1 spectrum with no condition. (b) The delay line spectrum with the scintillator grid coincidence with peaks fitted with a three-Gaussian function (red curve). (c) The linear fit of the mean of the peaks in channels vs. corresponding position in mm.	42
Figure 3.8	The calibrated correlation plot of x (mm) vs. y (mm) of TPC 6 showing the structure of scintillator grid.	43
Figure 3.9	The correlation between the angle x (mrad) and the x position (mm) at (a) One meter before the focal plane (b) One meter after the focal plane (c) At the focal plane at F4 region.	45
Figure 3.10	(a) The identification plot for the ^{23}O setting. The black circle shows an example of background events.	46
Figure 3.11	The correlation of $Veto_L$ vs. $Veto_R$ for the ^{23}O secondary beam.	47
Figure 3.12	The identification plot for the ^{23}O secondary beam after the veto rejection.	48
Figure 3.13	The correlation of (a) TPC4 energy signal vs MUSIC41 energy signal after the veto rejection. The events inside of the black contour represents the selection of good events.	48
Figure 3.14	The correlation of (a) MUSIC41 energy signal vs. TPC5 energy signal (b) MUSIC 41 energy signal vs. SC41 energy signal (c) TOF_{LL} vs. TOF_{RR} . The events inside black contour represents the selection of good events. The spectra show events after veto rejection.	49

Figure 3.15	The identification plot for the ^{23}O before the reaction target. The black contour represents the ^{23}O incident beam selection.	50
Figure 3.16	The MUSIC41 Z spectrum where the blue histogram represents the ^{23}O selection and the red histogram is the total Z spectrum normalized for ^{23}O .	50
Figure 3.17	The MUISC42 Z spectrum with the target (red) and without the target (blue) to identify the particles with unchanged Z after the reaction.	51
Figure 3.18	(a) The beam x position at the target (X_{target}) (b) Transmission ratio for different X_{target} positions where green vertical lines represent the selection region of constant R .	52
Figure 3.19	(a) The beam y position at the target (Y_{target}) (b) Transmission ratio for different Y_{target} positions where green vertical lines represent the selection region of constant R .	52
Figure 3.20	(a) The x angle of the beam at the target in mrad (b) Transmission ratio for different x angles where green vertical lines represent the selection region of constant R .	53
Figure 3.21	(a) The y angle of the beam at the target in mrad (b) Transmission ratio for different y angles where green vertical lines represent the selection region of constant R .	53
Figure 4.1	The transmission ratios for $^{16,18-24}\text{O}$ (a) with the reaction target (R_{in}) (b) without the reaction target (R_{out}).	56
Figure 4.2	The σ_{cc} found by varying the x position, y position, x angle and y angle of the beam at the target location for two sets of data for ^{24}O .	57
Figure 4.3	The measured σ_{cc} of $^{16-18,24}\text{O}$ with statistical uncertainties.	58
Figure 4.4	The MUSIC42 detector spectrum for the ^{23}O secondary beam. The red curve shows an exponential function fit of the tail of the $Z = 7$ peak.	60
Figure 4.5	The measured velocity (β) of the particles at SC41 for the ^{23}O secondary beam.	61
Figure 4.6	(a) The TPC detector energy loss vs. SC42 energy loss. The black geometric cut represents the selection of oxygen nuclei. (b) The energy loss spectrum of MUSIC after the detector with a selection cut from the left figure.	63

Figure 4.7	The σ_{cc} for ^{16}O calculated using three different harmonic oscillator widths for the density distributions with different R_p . The blue horizontal line represents the central value of the measured σ_{cc} . The black lines represent the uncertainties. The vertical lines show the rms proton radii corresponding to the measured σ_{cc} .	65
Figure 4.8	The measured point proton radii (R_p) where the black circles represent R_p^{cc} and the red squares represent $R_p^{(e^-)}$.	68
Figure 4.9	R_p from Ref. [34] calculated using $NNLO_{sat}$ interaction with three different many-body approaches compared to the measured R_p^{cc} (blue circles).	69
Figure 4.10	The comparison of the measured R_p^{cc} (blue circles) to R_p from Ref. [34] calculated using the EM interaction with three different many-body approaches and R_p from Ref. [27] computed using the coupled-cluster calculation.	70
Figure 4.11	The experimental neutron skin (blue circles) determined from measured R_p^{cc} and the measured R_m from Ref. [55, 56]. ΔR calculated using IMSRG approach with EM interaction (black symbols) and $NNLO_{sat}$ interaction (red symbols) from Ref. [34] is shown by plusses and ΔR calculated using radii from coupled-cluster calculation is shown by blue stars.	72

Abstract

The nuclear charge radius is an important bulk property of the nucleus for investigating nuclear structure. The nuclei lying close to the boundaries of the nuclear chart (the drip lines) have revealed new exotic features like the halo and skin. Another new phenomenon that has emerged in the neutron-rich region is the changing or vanishing of magic numbers. The systematic study of the proton radii along an isotopic chain is crucial for understanding the halo and skin formation and also the shell evolution in neutron-rich nuclei near the drip-line. We present the first determination of the proton radii of neutron-rich oxygen isotopes. The proton radii of $^{16,18-24}\text{O}$ were measured using the charge-changing cross sections, σ_{cc} , which is the total cross section for the change of the atomic number of the projectile nucleus due to any interaction with the protons in the projectile nucleus. The experiment was performed at the fragment separator (FRS) at GSI, Germany, at a relativistic beam energy of around 900 MeV. The proton radii were extracted from the measured σ_{cc} using the finite range Glauber model analysis. The measured proton radii of stable isotopes of oxygen, ^{16}O and ^{18}O , are consistent with the proton radii derived from the electron scattering experiments. A decrease in proton radii of ^{22}O and ^{24}O was observed, showing signatures of the unconventional shell closures at $N = 14$ and $N = 16$. This thesis also reports the first determination of neutron skin thickness (ΔR) in neutron-rich oxygen isotopes, determined using the measured proton radii reported in this work and measured matter radii available from the literature. ΔR rapidly increases from $^{22-24}\text{O}$ approaching the neutron drip-line, establishing a thick neutron surface for the neutron-rich oxygen isotopes. We have compared the measured proton radii to the predictions reported using various *ab initio* approaches with different interactions. The experimental proton radii presented have challenged these predictions.

Acknowledgements

I would like to thank my supervisor Dr. Rituparna Kanungo for her guidance, ideas, patience, support and motivation for the work done in this thesis. I consider myself very fortunate for being able to work with a very considerate and encouraging professor like her. It was a great learning experience to work under her supervision.

I would like to express my gratitude to my thesis committee members Dr. Scott Chapman, Dr. Adam Sarty and Dr. David Hornidge for their support during my research.

Special thanks go to the previous and current collaborators at FRS, GSI Germany. Working with all of you has been the most educational and enjoyable experience of my life. I owe my thanks to all of the members of FRS collaboration including physicists, engineers and technicians who worked hard, day and night, to make the experiment successful.

I am deeply thankful to Soumya who was always there for helping me out with all kind of problems with his suggestions and discussions. I would like to thank Preet and Gurpreet for all the fun times. I would also like to thank my special friends Daisy and Anwinder.

Thank you Mom and Dad, for all of the unconditional love and encouragement. This thesis would have been simply impossible without your support. I thank my siblings Manbir and Taran for their constant support in all phases of my life. I would like to express my gratitude to Manbir and Gary for answering all my queries whether it was programming, writing and other aspects like dealing with the stress. A special thanks to Rajveer for all of the moral support, love and care. It would have been a lot harder without you to get through this PhD.

In retrospect, there are so many great people to give thanks to. Without them, I would not have been able to come this far or complete this thesis. Though I cannot print out all of the names, it is worthy noting that many great people helped me in different ways along this journey. I thank them all here.

Satbir Kaur

Chapter 1

Introduction

The discovery of the nucleus goes back to 1909 when Geiger and Marsden irradiated gold foils with alpha particles and observed the backscattered alpha particles [1]. This led Rutherford to postulate that most of the mass is located in a small, dense center of the atom, a nucleus. There was a disparity between an element's atomic number (protons = electrons) and its atomic mass. Therefore, it seemed there must be something else in the nucleus, in addition to protons. Chadwick solved the puzzle about the constituents in the atomic nucleus when he discovered the neutron [2].

However, the fundamental question was: what's holding the nucleus together despite the Coulomb repulsion of the protons? In 1935, Yukawa proposed that the nucleons exchange particles and this mechanism creates the force. He suggested that according to the uncertainty principle, the exchange particle for the nuclear force should be a charged particle with rest mass ~ 200 MeV [3]. Later, this particle, the pion, was discovered [4] and its mass was found to be close to the mass predicted by Yukawa. The mass of the lightest meson observed set the nuclear force range to be ~ 1 fm. As this range is even smaller than the size of the nucleus, the nucleons should mainly interact with their nearest neighbors. In addition, it was evident from the measured nuclear binding energies that the nuclear interaction saturates, resulting in a nearly constant interior nucleon density. On the basis of these properties of the nuclear force, the nucleus was considered analogous to a drop of a liquid [5]. The liquid drop model examines the global properties of nuclei, such as binding energies, sizes and shapes. It provides a good fit to the measured nuclear binding energies to the first order, however, deviations were observed at certain proton or neutron numbers which pointed out the existence of closed shells at these numbers. The observed neutron separation energies with respect to neutron number and the first excited states of even-even nuclei (even N and even Z) in stable isotopes exhibited discreet jumps at certain specific nucleon numbers called "magic numbers". The relative abundance

of elements with the magic number of protons is higher and they have relatively low neutron absorption cross sections. These observations provided an evidence for the shell closures at the following nucleon numbers:

$$2, 8, 20, 28, 50, 82, 126$$

On the basis of these observations, the independent particle shell model was proposed, where each nucleon inside the nucleus was assumed to move independently from the others in a spherically symmetric potential produced by all of the nucleons. The

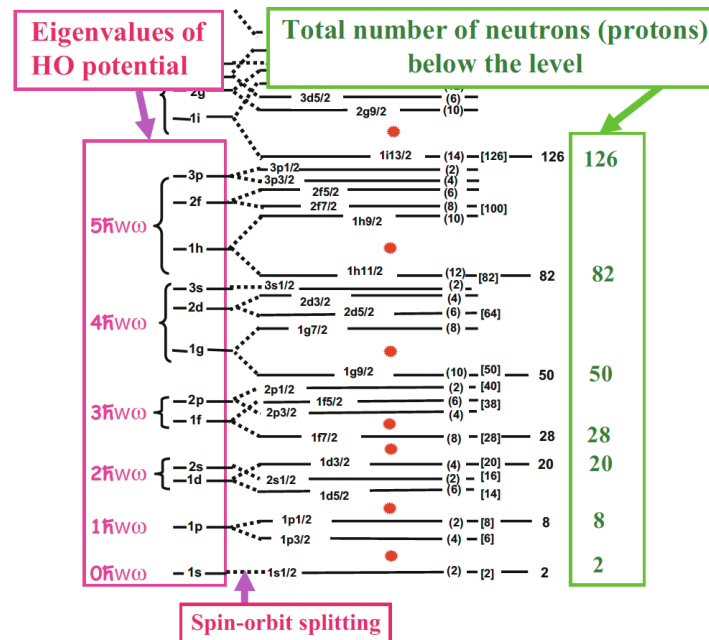


Figure 1.1: Mayer-Jensen's shell model scheme predicted with harmonic oscillator potential and the spin-orbit force [6, 7]. Figure adapted from [8].

energy levels predicted by considering a harmonic oscillator (HO) potential are shown in figure 1.1 in the pink box. Unfortunately, except for the lowest few, these shells do not correspond to the empirical magic numbers. Mayer [6] independent of Haxel, Jensen and Suess [7] added a spin-orbit interaction to the HO potential that enabled it to reproduce the empirical magic numbers. In general, the shell model provides an excellent reproduction of measured excitation energies, spin/parities for the ground state and low-energy excited states. However, the shell model could not predict magnetic dipole moments, electric quadrupole moments and the spectra of excited

states for some nuclei. Therefore, various models to account for the collective motion of nucleons were proposed.

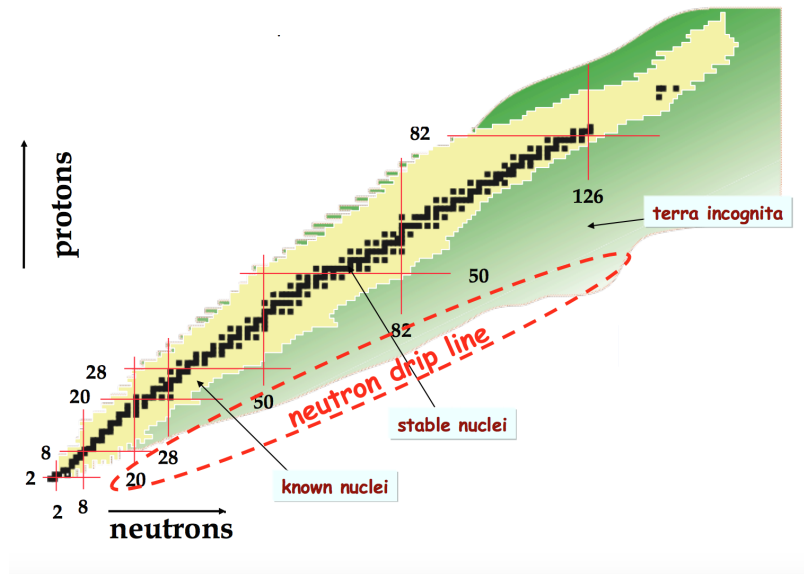


Figure 1.2: The nuclear landscape where each square represents a nucleus. The valley of stability is shown by black, unstable nuclei are represented by yellow and green region shows theoretically predicted bound nuclei.

The nuclear models discussed so far were formulated based largely on data of around 300 stable nuclei. One can add neutrons or protons to a nucleus until the nuclear drip-line is reached, where the binding energy is not enough to prevent the last nucleon from “dripping” off the nucleus. The proton and neutron drip-lines form the boundaries of nuclear existence. Modern day nuclear physics facilities can produce over 3000 unstable nuclei. The evolution of the nuclear chart is shown in figure 1.2 where the black nuclides are stable and the yellow nuclides are the unstable nuclei. The red lines indicate the traditional magic numbers and red dashed curve shows the location of the neutron drip-line. The nuclei lying close to the neutron drip-line, neutron-rich nuclei, have revealed new features that differ from those lying close to the valley of stability. These nuclei with $N/Z \gg 1$ exhibit exotic phenomena like the existence of a neutron halo or skin. Another new phenomenon that has emerged in the neutron-rich region is the changing or vanishing of some of the magic numbers [9, 10]. Progress in understanding nuclear structure can be made by collecting new experimental data and comparing them to theoretical predictions.

The charge radius of a nucleus is among the important inputs that are needed to investigate the nuclear structure and test the newly developing theoretical models. The evolution of charge radii along an isotopic chain can show signatures of shell closures as local minima [11]. The proton radii together with the knowledge of the matter radii (radii of nucleon distribution in nuclei) are also important to deduce the neutron skin thickness in the neutron-rich nuclei. The neutron-rich oxygen isotopes are particularly interesting nuclei, with a new magic number ($N = 16$) [9, 10, 12, 13] at the neutron drip-line [14–19]. The objective of this dissertation is to determine the proton radii, R_p , of $^{16,18-24}\text{O}$ from the charge-changing cross section (σ_{cc}) measurements. R_p is defined as the rms radius of proton density distribution inside a nucleus with protons considered as point particles (henceforth referred to as point proton radii). The point proton radii of neutron-rich oxygen isotopes ($^{19-24}\text{O}$) have not been measured till date. The following sections of the introduction start with a brief description of concepts like neutron halo and skin. After that, the objective of the work is discussed, followed by a brief discussion on conventional methods that are used to measure the charge radii and their limitations for measuring the charge radii of neutron-rich nuclei. The introduction concludes with a description of the charge-changing cross sections and discussion of the Glauber Model, a theoretical tool used to extract the proton radii from the measured σ_{cc} .

1.1 Exotic phenomena of neutron-rich nuclei: halos and skin

1.1.1 Neutron halos

The term “nuclear halo” refers to one or two weakly bound neutrons forming an extended low density surface around a core, which has a compact density with similar density distributions for protons and neutrons. Nuclear halos are of quantum mechanical origin and therefore can only be understood by considering the probability distribution of the least bound nucleon. In a simple model, the interaction potential between the halo neutron and the core can be assumed as a square well and the wave function of the neutron outside the potential is written as

$$\psi(r) = \left(\frac{2\pi}{\kappa}\right) \left(\frac{-e^{\kappa r}}{r}\right) \left[\frac{e^{\kappa R}}{(1 + \kappa R)^{1/2}}\right] \quad (1.1)$$

where R is the width of the potential and κ is the slope of the density tail [20]. Using this wavefunction, the density distribution of the neutron is related to the wave function as

$$\rho(r) = |\psi(r)|^2 \quad (1.2)$$

and κ is related to the separation energy of the neutron (E_s) as,

$$(\hbar\kappa)^2 = 2\mu E_s \quad (1.3)$$

where μ is the reduced mass of the core and the neutron. As E_s decreases, κ decreases and thus the tail of the distribution becomes longer. However, in addition to a small separation energy, a small orbital angular momentum of the state is also a necessary condition for a nucleus to form a halo state. The higher angular momentum provides an additional centrifugal barrier which lowers the probability of tunneling to a larger radius, leading to less extension of the wave function. Therefore, the halos are expected to most likely appear when the valence neutrons are in the s and p states. The presence of the Coulomb barrier in the proton-rich nuclei makes proton halos less pronounced than neutron halos.

1.1.2 Neutron skin

A neutron skin is formed when the half density radius of neutrons is greater than that of the protons with the surface density slope for the neutrons being similar to the protons. The neutron density actually extends out significantly further than that of the protons, resulting in a mantle of neutrons as shown in figure 1.3 (a). The neutron skin thickness ($\Delta R = R_n - R_p$) is defined as the difference between the root mean square radii of the neutron and proton distributions. Recently some studies have focused on ^{208}Pb , which is a stable nucleus with 126 neutrons and 82 protons. The observed neutron skin thickness ($\Delta R = 0.15 \pm 0.03(stat) \pm 0.01(sys)\text{fm}$) [21] is relatively small. However, in the case of neutron-rich nuclei ($N/Z \gg 1$), the observed neutron skins are significantly thicker. For example $\Delta R = 0.9\text{ fm}$ was observed in ^8He from a cluster-type model analysis of the measured interaction cross sections, the two-neutron removal cross sections, and the four-neutron removal cross section of $^{4,6,8}\text{He}$ [22]. Matter radii of He isotopes determined in Ref. [22] showed a drastic

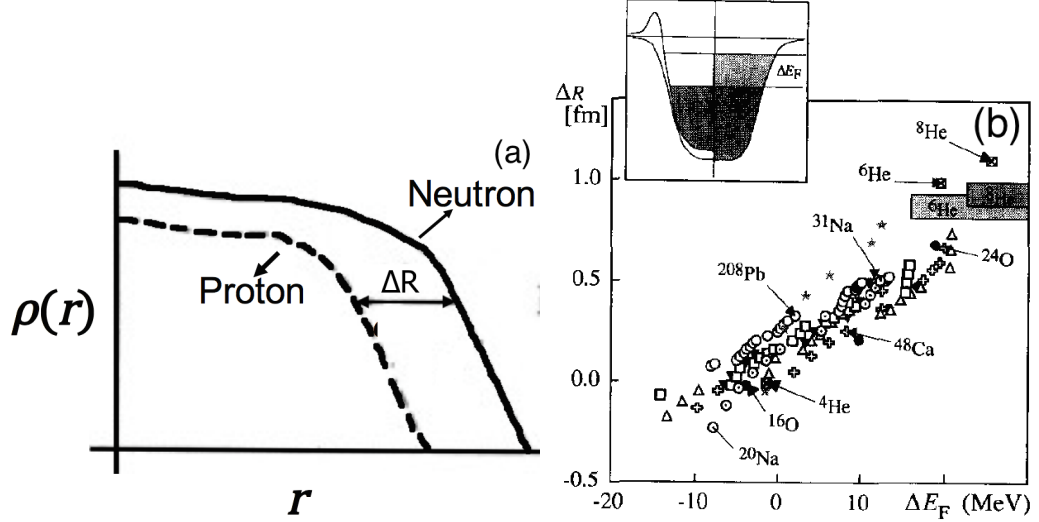


Figure 1.3: (a) A schematic illustration of neutron skin. (b) ΔR_{rms} as a function of ΔE_F of various isotopes obtained by the RMF Model. The empirical values are shown in shadowed boxes. Right figure adapted from [22].

increase from ${}^4\text{He}$ (1.57 ± 0.05 fm) to ${}^6\text{He}$ (2.48 ± 0.03 fm) and ${}^8\text{He}$ (2.52 ± 0.03 fm). The empirically deduced proton and neutron density distributions were well reproduced by the Relativistic Mean Field (RMF) calculations. The RMF model calculations were applied to other nuclei near the drip-line and are shown in figure 1.3 (b), which shows the difference in proton and neutron rms radii (ΔR) as a function of the difference in Fermi energies of protons and neutrons (ΔE_F). As shown in figure 1.3 (b), all nuclei with ΔE_F larger than ~ 10 MeV have ΔR values larger than 0.5 fm. Therefore, the origin of thick neutron skin in neutron-rich nuclei can be understood to be arising from a large ΔE_F which is a consequence of neutrons filling higher shells or sub-shells. As seen in figure 1.3(b), the most neutron-rich isotope of oxygen, ${}^{24}\text{O}$, was predicted to have a very thick neutron skin based on these calculations. The results, however, were model-dependent and were therefore somewhat qualitative since no measurement for the proton distribution of ${}^{24}\text{O}$ was performed at that time.

1.2 Motivation to study proton radii of ${}^{16-24}\text{O}$

Oxygen isotopes with a closed shell of protons ($Z = 8$) are good candidates to examine the evolution of shells approaching the neutron drip-line and investigate the effects of nuclear forces. The most abundant stable isotope of oxygen, ${}^{16}\text{O}$, is a doubly magic

nucleus with $Z = 8$ and $N = 8$ shell closures. In exotic nuclei far away from the region of stability, a new shell closure ($N = 16$) at the neutron drip-line has recently been observed in the oxygen isotopes.

1.2.1 Drip line of oxygen isotopes and $3N$ forces

Oxygen isotopes are a subject of interest because the neutron drip-line of oxygen isotopes is found to be at ^{24}O whereas the Nucleon-Nucleon (NN) potentials predicted the drip-line to be at ^{28}O (the expected doubly magic nucleus). Oxygen is the heaviest element for which the neutron drip-line has been confirmed experimentally. The evidence of neutron drip-line at ^{24}O comes from following measurements. In 1985 Langevin et al. found ^{25}O is unbound [14] and five years later it was found that ^{26}O is unbound as well [15]. The expected doubly magic nucleus ^{28}O ($N = 20$) was found to be unbound by Tarasov et al. indicating the disappearance of conventional shell closure at $N = 20$ [16]. The first spectroscopy of ^{25}O was done by Hoffman et al. who found that ^{25}O is unbound by 770 keV with a decay width of 172(30) keV [17]. The upper limit on the ground state energy of ^{26}O was found by Lunderberg et al. who found that ^{26}O is unbound by less than 200 keV [18]. A recent experiment at the SAMURAI facility at RIKEN precisely determined the ground state energy of ^{26}O to be 18 ± 3 keV above the two neutron decay threshold [19]. The energy and width of the unbound ground state of ^{25}O were also determined precisely in this experiment as 749 ± 10 keV and 88 ± 6 keV, respectively.

The neutron drip-line at $N = 16$ could not be reproduced using the NN potentials. Fujita and Miyazawa, considering the fact that nucleons are composite particles, extended Yukawa's meson exchange idea to three nucleons ($3N$) [23]. One example of the $3N$ mechanism is an exchange of two pions between three nucleons with one nucleon virtually exciting a second nucleon to the Δ resonance, which is de-excited by scattering off a third nucleon. Otsuka et al. [24] suggested that the drip-line of oxygen isotopes can be explained by including the contribution from the $3N$ forces ($3NF$ s). Otsuka et al. [24] included the $3NF$ s among two valence neutrons and one nucleon in the ^{16}O core within the sd -shell model and found that the inclusion of $3NF$ s lead to the drip-line at $N = 16$ for the oxygen isotopes in agreement with the experiments. Three-nucleon interactions arise naturally in the chiral effective field

theory (χ EFT) [25] which is a systematic approach to derive the nuclear force from the underlying theory of strong forces, quantum chromodynamics (QCD). At the low energies relevant to nuclear physics, the QCD coupling constant is large. Therefore, a perturbative expansion of nuclear processes becomes non-convergent. In χ EFT, nucleons and pions are taken as relevant degrees of freedom. The QCD Lagrangian is expanded in powers of Q/Λ_χ with a momentum $Q \sim m_\pi$ and the chiral-symmetry breakdown scale $\Lambda_\chi \sim m_\rho$, which makes Q/Λ_χ a small quantity. A diagram of this expansion of the nuclear interaction is shown in figure 1.4 where LO is the leading order term, NLO is next-to-leading order term and so on. The hierarchy of nuclear forces, i.e. NN interactions should be more important than three-nucleon ($3N$) interactions, which in turn should be more important than four-nucleon ($4N$) forces, and so on, is illustrated in figure 1.4. The high-energy physics is included in the theory via renormalization and absorbed into coefficients called low-energy constants. The LECs are fitted on experimental data; usually nucleon-nucleon phase shifts, binding energies and other few-body observables.

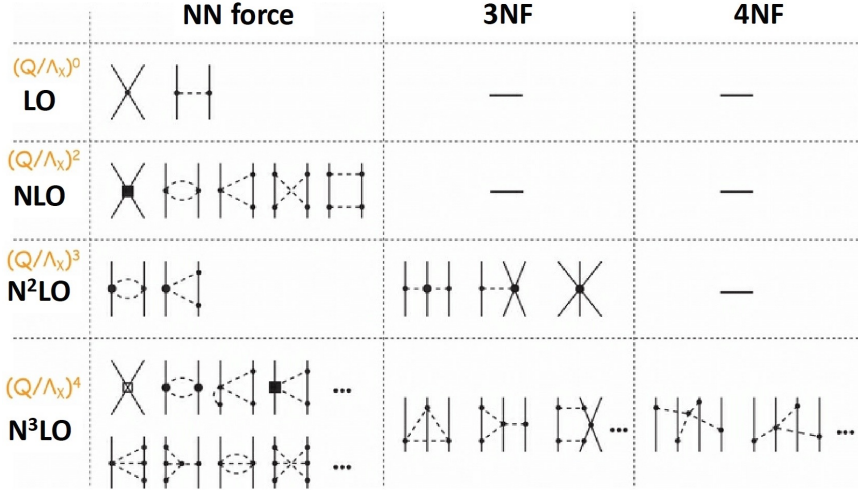


Figure 1.4: Chiral effective field theory for nuclear forces. The different contributions at successive orders are shown diagrammatically. Nucleons and pions are represented by solid and dashed lines, respectively. Figure adapted from [26].

The *ab initio* models have made tremendous progress where several calculations have successfully reproduced the neutron drip-line at ^{24}O [27–34]. In Refs. [27,28,31–33] the ground state energies of oxygen isotopes were calculated with Entem and Machleidt (EM) interaction [35] using several types of many-body approaches. In EM interaction

the NN interaction was taken up to N^3LO whereas the three-nucleon interaction was taken upto $NNLO$. The low-energy coupling constants (LEC) were derived from nucleon-nucleon scattering and the properties of the $A = 3$ and $A = 4$ nuclei. The binding energies for the oxygen isotopes obtained with the EM interaction are consistent with each other and with the experimental data within 1% of the total binding energies.

V. Lapoux et al. [34] studied the binding energies and R_p in oxygen isotopes by performing *ab initio* calculations with $NNLO_{sat}$ nuclear interaction [36], which is a simpler interaction as it includes contributions up to NNLO for both two and three-nucleon interactions. In $NNLO_{sat}$ interaction, the NN and $3N$ forces are optimized simultaneously in contrast to the EM interaction [35] in which the $3NFs$ are optimized subsequently. The determination of the low-energy coupling constants in $NNLO_{sat}$ interaction includes data on binding energies and radii of ^3H , $^3,4\text{He}$, ^{14}C and ^{16}O isotopes, in addition to the low energy NN data. The binding energies calculated with the $NNLO_{sat}$ interaction (red symbols) and the EM interaction (black symbols) using different many-body approaches are shown in figure. 1.5 (a). The stars represent Self Consistent Greens Function (SCGF) calculations by Gorkov (GGF), the triangles represent the Dyson SCGF (DGF) calculations and the plusses represent the in-medium similarity renormalization group (IMSRG) calculations. The experimental binding energies represented by blue symbols agree with these various *ab initio* approaches.

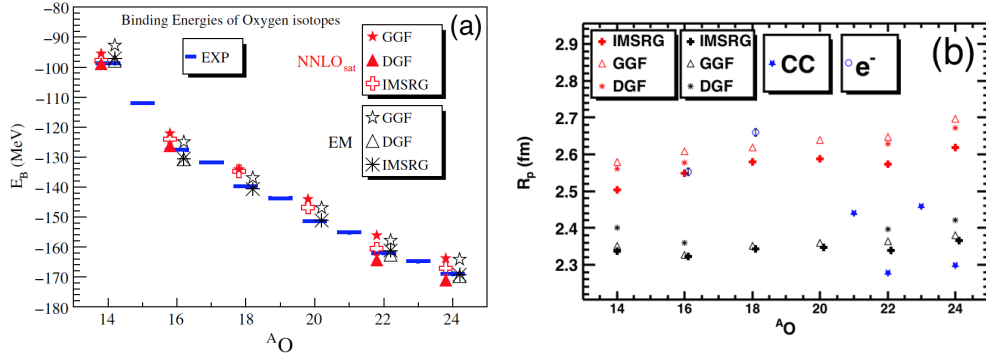


Figure 1.5: (a) The binding energies (b) R_p from Ref. [34] using the $NNLO_{sat}$ interaction (red symbols) and the EM interaction (black symbols) calculated in three different many-body approaches. The blue stars are R_p from Ref. [27] calculated using coupled-cluster calculations. The experimental R_p derived from the e^- scattering experiments [37] are shown by blue open circles.

1.2.2 Proton radii: A test for *ab initio* approaches

The reliability of various *ab initio* models depends on their description of other fundamental observables like charge radius in addition to the binding energies. Figure 1.5(b) shows the proton radii calculated using the $NNLO_{sat}$ (red symbols) and the EM interaction (black symbols). The stars represent Dyson SCGF (DGF), the plusses represent the in-medium similarity renormalization group (IMSRG), and the triangles represent the Gorkov SCGF (GGF) calculations from Ref. [34]. The R_p calculated using the coupled-cluster calculation with EM interaction from Ref. [27] are also shown in figure 1.5(b) (blue stars). The open circles represent the measured R_p found using the charge radius (R_{ch}) from the e^- scattering experiments [37] using the equation:

$$\langle R_{ch}^2 \rangle = \langle R_p^2 \rangle + \langle r_p^2 \rangle + \frac{N}{Z} \langle r_n^2 \rangle + \frac{3\hbar^2}{4m_p^2 c^2} \quad (1.4)$$

where r_p and r_n are the charge radii of a proton and a neutron and the last term is the Darwin-Foldy relativistic correction [38]. As seen in figure 1.5 (b), there is a clear discrepancy between radii calculated using two different interactions, the measured R_p of ^{16}O is closer to R_p calculated by $NNLO_{sat}$, however, it should be considered that the LEC in $NNLO_{sat}$ includes the R_{ch} of ^{16}O . There is no data on the proton radii of the neutron-rich oxygen isotopes, which is required in order to provide constraints on these theoretical predictions.

1.2.3 The shell evolution in oxygen isotopes

Another remarkable feature of oxygen isotopes is that there is a new shell closure ($N = 16$) at the neutron drip-line. The first experimental indication of the $N = 16$ shell closure came from a study of the neutron separation energies (S_n), the amount of energy needed to remove the outer-most neutron from a nucleus as a function of isospin $T_z = \frac{N-Z}{2}$ [9]. The measured S_n values for nuclei with odd N and even Z as a function of the neutron number in an isospin chain are shown in figure 1.6. The S_n systematics as a function of neutron number for nuclei with low isospin ($T_z < 5/2$) show drops in energy following the magic numbers $N = 8$ and 20 , indicated by black upward arrows in figure 1.6.

However, for the neutron-rich nuclei ($T_z \geq 5/2$) a new break appears at $N = 16$ indicated by the brown downward arrow. The systematic study of beta decay Q values and the energies of the first excited state also showed sharp discontinuities and confirmed the shell closure at $N = 16$ [10]. The sixteen neutrons of the drip-line nucleus, ^{24}O , should fill the neutron levels ($1s_{1/2}1p_{3/2}1p_{1/2}1d_{5/2}2s_{1/2}$) as shown in figure 1.7. The spectroscopic factor (S), which is the probability to occupy a final single-particle state when a nucleon is removed from or added to the target nucleus was measured through the neutron removal reaction of ^{24}O [12]. A nearly pure $2s_{1/2}$ neutron spectroscopic factor of 1.74 ± 0.19 was determined, which established that the last two neutrons in ^{24}O exhibit single particle behaviour and that the nature of the shell closure is spherical. A small quadrupole deformation parameter

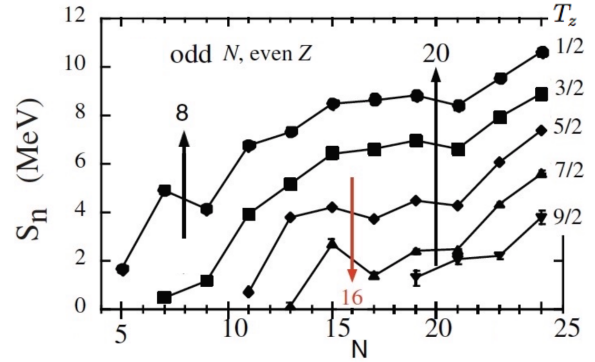


Figure 1.6: One-neutron separation energy for different isospin chains. Figure taken from [39].

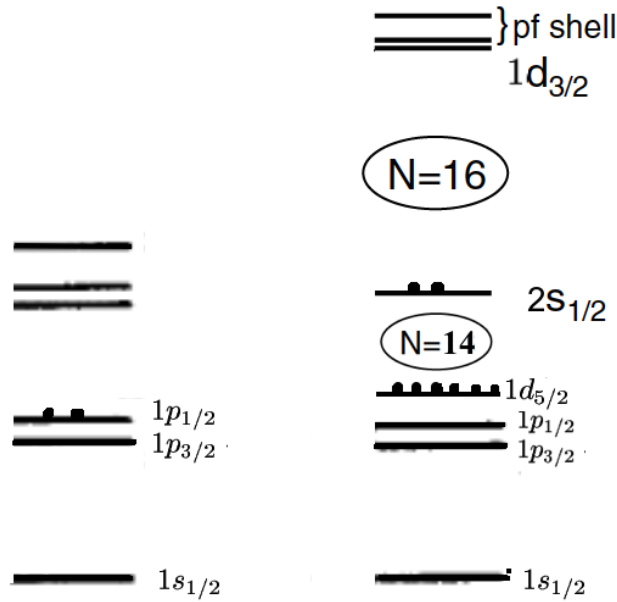


Figure 1.7: The shell model scheme of ^{24}O .

($\beta_2 = 0.15 \pm 0.04$) of the first 2^+ excited state of ^{24}O , determined by proton inelastic

scattering [13], also confirmed the spherical nature of this shell closure. The $N = 16$ shell gap implies an increased energy gap between the $2s_{1/2}$ and $1d_{3/2}$ orbitals (figure 1.7). A large shell gap was obtained (~ 4.8 MeV) in ^{24}O from the excitation energy of the 2^+ state (figure 1.8 (a), black symbols) observed through neutron removal reactions from ^{26}F to ^{24}O [40].

One proposed mechanism for the emergence of this new magic numbers in neutron-rich oxygen isotopes is thought to be related to the monopole interaction of the nuclear force [41, 42]. The tensor component of nuclear interaction is written as

$$V_{\tau\sigma} = \tau \cdot \tau\sigma \cdot \sigma f_{\tau\sigma}(r) \quad (1.5)$$

with “ \cdot ” denoting the scalar product between the isospin (τ) and spin (σ) operators. $f_{\tau\sigma}(r)$ is a general function of the interaction distance r . In the long range limit, $f_{\tau\sigma}(r) = 1$ and $V_{\tau\sigma}$ produces a strong attraction between a spin- and isospin-flip pair of orbitals i.e. between $j_>(l + 1/2)$ and $j_<(l - 1/2)$ and between the proton and the neutron orbitals. It should be observed that in figure 1.8 (a) the first excited state of neon ($Z = 10$, red symbols) and magnesium isotopes ($Z = 12$, green symbols) do not show any increase at $N = 16$. This is because, for these isotopes the protons in the $1d_{5/2}$ orbital interact strongly with the neutrons in the $1d_{3/2}$ orbital, pulling these orbitals down. However, in oxygen isotopes the proton $1d_{5/2}$ orbit is vacant, thus the attraction is missing which causes the neutron $1d_{3/2}$ orbital to remain high in energy. This creates the shell gap at $N = 16$. It is observed in figure 1.8 (a) that the first excited states of the carbon, neon and magnesium isotopes at $N = 14$ remain relatively constant in contrast to the oxygen isotopes, for which it rises sharply. The high-lying first excited state in ^{22}O at 3.17 MeV [43, 44] suggests that $N = 14$ is another possible shell gap in oxygen isotopes. The shell gap between neutron $1d_{5/2}$ and $2s_{1/2}$ orbitals of ^{22}O was derived from the observation of an unbound $1d_{5/2}$ hole state at 2.79(13) MeV in Ref. [45]. This finding was also supported by a small deformation factor (β) = 0.26(4) for ^{22}O which was derived from the phenomenological analysis of proton inelastic scattering [46]. The effect of the $N = 14$ shell closure is seen in the systematic trend of one-neutron knockout cross sections and widths of the fragment longitudinal-momentum distributions with increasing neutron number, shown in figure 1.8 (b). For the oxygen isotopic chain (represented by green symbols),

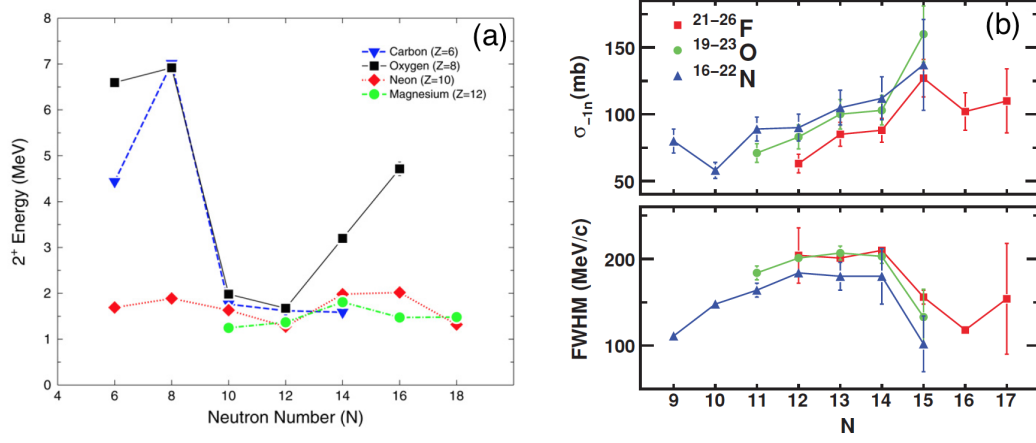


Figure 1.8: (a) The first excited states of different isotopes plotted as a function of the neutron number. Figure taken from [40]. (b) The one-neutron knockout cross sections and widths of the fragment longitudinal-momentum distributions as a function of the neutron number. Figure taken from [47]

the valence neutrons occupy a $1d_{5/2}$ orbit up to $N = 14$, while for $N = 15$ and 16 , the valence neutrons occupy the $2s_{1/2}$ level (figure 1.7). The observed narrowing of momentum distribution at $N = 15$ in figure 1.8 (b) supports the single particle s orbital occupancy of the valence neutron in ^{23}O . An increase in one-neutron knockout cross sections observed at $N = 15$ for oxygen isotopes (shown in figure 1.8 (b) by green symbols) indicates that the valence neutron occupies $2s_{1/2}$ orbital above the shell gap [47]. The $2s_{1/2}$ spectroscopic factor was found to be 0.97(19) in Ref. [48] from one-neutron knockout of ^{23}O and 0.78(13) from the Coulomb dissociation [49] indicating a $2s_{1/2}$ single particle structure of ^{23}O and therefore a shell gap at $N = 14$. The shell gap in oxygen isotopes could be caused by the strong attractive monopole interaction between the proton $1p_{1/2}$ and neutron $1d_{5/2}$ which pulls these orbitals down, thus creating the energy gap. The removal of protons from the $1p_{1/2}$ orbital weakens the $N = 14$ shell closure, therefore it is less pronounced for nitrogen and disappears altogether for carbon isotopes [50–54].

The shell gaps can also be visible as local minima in the radii along an isotopic chain [11]. Therefore, the evolution of the proton radius of neutron-rich oxygen isotopes with increasing neutron number will help us establish the shell closure at $N = 14$ and also understand the cause of its emergence in neutron-rich nuclei.

1.2.4 Neutron skin in oxygen isotopes

The proton radii of neutron-rich oxygen isotopes are also important to determine the neutron skin thickness, ΔR , which is the difference between the root mean square radii of the neutron and proton distributions. The root mean square matter radii, R_m , are related to the root mean square proton radii, R_p , and the root mean square neutron radii, R_n , according to relation given below

$$R_m^2 = \left(\frac{N}{A}\right)R_n^2 + \left(\frac{Z}{A}\right)R_p^2 \quad (1.6)$$

where Z = atomic number, A = mass number and N = neutron number.

R_n and the neutron skin can be determined from the measured matter radii and proton radii using equation 1.6. The calculated matter and proton radii from Ref. [34] were used to calculate the neutron skin thickness (ΔR), which is shown in figure 1.9. The plusses represent the IMSRG calculations with the EM interaction (black symbols) and the $NNLO_{sat}$ interaction (red symbols). The calculated (ΔR) using the calculated radii with the coupled-cluster approach from Ref. [27] are also shown in figure 1.9 by the blue symbols. As seen in figure 1.9, a thick neutron skin is expected in the neutron-rich oxygen isotopes. The predicted skin thickness for ^{24}O shows a difference between the coupled-cluster and IMSRG calculations. A thick neutron skin in ^{24}O has also been predicted in Ref. [22]. Therefore, the measurement of R_p of neutron-rich oxygen isotopes is needed to determine the neutron skin experimentally.

1.3 Conventional methods to determine proton radii

The matter radii have been determined for a wide range of unstable nuclei [55, 56] mainly by using the measured interaction cross sections. On the other hand, the data regarding the proton radii is rather limited for the unstable nuclei. A brief description of various techniques for measuring the proton radii is given below.

1.3.1 Electron scattering

The scattering of electrons from nuclei has given the most precise information on nuclear and nucleon structure. Electron scattering avoids the complexity of the strong interaction between the projectile and the target and provides precise information

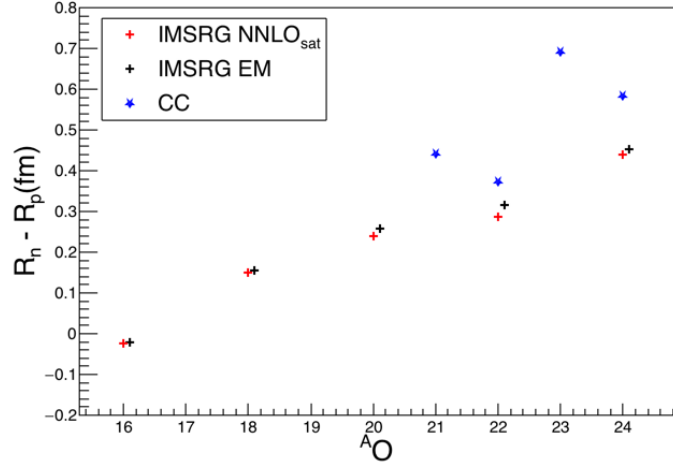


Figure 1.9: The neutron skin calculated using the calculated R_p and R_m . The plusses represent ΔR calculated using radii with IMSRG many-body approach with EM interaction (black) and $NNLO_{sat}$ interaction (red), taken from Ref. [34]. The stars represent ΔR found from the radii calculated with coupled-cluster calculations from Ref. [27].

about the charge distribution in the nucleus. Since the charge distribution of the nuclei is the subject, only elastic electron scattering is discussed. The differential cross section for elastic scattering from a spin less nucleus under a Plane-Wave Impulse-Approximation (PWIA) is given as,

$$\frac{d\sigma}{d\Omega} = \frac{d\sigma_{Mott}}{d\Omega} |F_c(q)|^2 \quad (1.7)$$

where $d\sigma_{Mott}/d\Omega$ is the Mott cross section and $F_c(q)$ is the charge form factor [57]. The Mott cross section is the elastic scattering cross section from a point particle of charge Z .

$$\frac{d\sigma_{Mott}}{d\Omega} = \frac{(Z\alpha)^2 \cos^2(\theta/2)}{4e^2 \sin^4(\theta/2)} \quad (1.8)$$

where e is the electron energy, θ is the scattering angle and α is the fine-structure constant. The form factor is a Fourier transform of the charge distribution ($\rho_c(r)$), for momentum transfer, q ,

$$F_c(q) = \frac{1}{2\pi^{3/2}} \int \rho_c(r) e^{-i\vec{q}\cdot\vec{r}} r d\vec{r} \quad (1.9)$$

One can determine $\rho_c(r)$ of a target nucleus by an inverse Fourier transformation of the experimentally determined charge form factor.

Electron scattering has been successfully applied to stable nuclei and the charge distribution data is compiled in Ref. [58]. Some unstable nuclei have also been studied by elastic electron scattering, namely ^3H and ^{14}C [59,60]. The study of unstable nuclei with electron scattering require long half-lives to allow preparation of sufficiently thick radioactive targets. The short-lived nuclei located far from the β stability line have not been studied so far by electron scattering. The SCRIT (Self-Confining RI Ion Target) electron scattering facility project has been commissioned at RIKEN RI beam factory to conduct electron scattering of rare isotopes [61]. The principle is to trap the target ions along the electron beam axis which reduces the required number of target nuclei significantly. An experiment has recently been performed in order to study the nuclear shape of the stable ^{132}Xe [62]. This facility aims to conduct the electron scattering of the short-lived neutron-rich nuclei in the near future.

1.3.2 Isotope shift

Isotope shift is the change in energy of atomic transition levels when we move from one isotope to another. The change can be due to the change of mass (mass shift) and due to change in the charge distribution inside the nucleus (volume shift or the field shift). The difference in the volume shift of two isotopes determines the difference in their charge radii. The measurement of charge radii using isotope shift measurements in Na isotopes provided the first direct evidence of neutron skin [63]. The matter radii were determined from the interaction cross section measurements. A gradual growth of neutron skin thickness up to 0.4 fm was observed in neutron-rich β unstable Na isotopes. However, in the case of light nuclei, the mass-based isotope shift is 10,000 times larger than the volume shift. Therefore, the charge radii of light nuclei, could not be extracted from isotope shift measurements until the new accurate atomic calculations of mass shifts together with high precision mass measurements were made. The charge radii of He [64,65], Li [66] and Be [67] isotopes determined by this technique are shown in figure 1.10. The charge radius decreases from ^6Li to ^9Li and then increases for ^{11}Li . In the He isotopes, it increases significantly from ^4He to ^6He and decreases from ^6He to ^8He . In Be isotopes, there is an increase in the charge radius

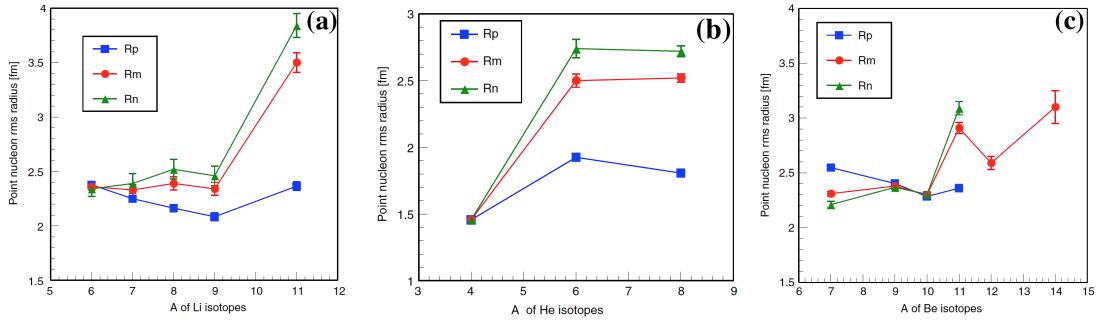


Figure 1.10: The radii of point nucleon distribution in (a) Li isotopes (b) He isotopes (c) Be isotopes. Figures adapted from [68].

from ^{10}Be to ^{11}Be . Therefore, it can be concluded that the charge radius increases when a neutron halo is formed as ^{11}Li , ^6He , ^{11}Be are confirmed halo nuclei from study of the narrow momentum distribution and enhancement of interaction cross-section measurements [68]. Such an increase may originate from the fact that in the halo nuclei the valence neutron in the $2s_{1/2}$ orbital has extended density distribution. This causes the center-of-mass (*c.m.*) of the nucleus to be different from that of the core leading to *c.m.* motion smearing of the core density and hence a larger proton radius. The decrease in charge radius in ^8He can be explained if the four excess neutrons are considered to be distributed in a more spherically symmetric fashion around ^4He core and the smearing of the charge in the core is correspondingly less as compared to ^6He . Recently, charge radii of $^{41,51,52}\text{Ca}$ were measured using isotope shift [69]. The charge radius of ^{52}Ca is much larger than theoretical predictions and has opened new intriguing questions on the evolution of nuclear sizes away from stability. However, the isotope shift measurements have not been extended to other light neutron-rich isotopes so far because the production of low energy and high intensity beams of short-lived isotopes of these elements is difficult. The other main challenge is that the atomic physics calculations become arduous due to many-body correlations between the electrons in the atoms.

1.3.3 Muonic Atom X-Ray Spectroscopy

A different approach to determine the charge distribution inside the nucleus is to measure the X-ray transition energy of muonic atoms [70]. The muon is 207 times more massive than the electron. When a negative muon is captured by the nucleus,

it can form a muonic atom. The atomic Bohr radius is inversely proportional to the mass of the orbiting lepton. Therefore, in muonic atoms the negative muon moves around the nucleus with an atomic Bohr radius about 200 times smaller than in the corresponding electronic atom. An increase in the energy shift for a muonic atom over a normal atom can be estimated to be as $(m_\mu/m_e)^3$ [71]. Muonic X-ray spectroscopy has been applied to almost all stable elements and the determined charge radii are available in the Refs. [37, 72]. Since the experimental method requires several tens of milligrams of target, no muonic X-ray spectroscopic investigation has yet been performed so far for short-lived nuclei, although researchers start to consider [73] this opportunity. The idea is to stop both μ^- and nuclear beams simultaneously in a solid deuterium film, followed by the application of the direct muon transfer reaction to higher Z nuclei to form radioactive muonic atoms.

1.4 Charge-changing cross section measurement

Charge-changing cross section (σ_{cc}) is the cross section for the change in the atomic number of the projectile nucleus due to any interaction with protons in the projectile nucleus. σ_{cc} is related to the distribution of protons in a nucleus. It is therefore a useful method from which the point-proton radius can be derived using the Glauber model theory. The σ_{cc} of stable isotopes were measured by Webber et al. [74] and Cummings et al. [75] to interpret the interstellar production of secondary fragments during cosmic-ray propagation in the galaxy, and so to determine elemental and isotopic components of cosmic rays. Two years later, Blank et al. [76] measured the σ_{cc} of neutron-rich lithium isotopes to investigate the proton distribution of these isotopes by comparing their results to Glauber model calculations. But no attempt to determine the proton radii was made. Further measurements of σ_{cc} for the light stable and neutron-rich nuclei (^{14}Be , $^{10-19}\text{B}$, $^{12-20}\text{C}$, $^{14-23}\text{N}$, $^{16-24}\text{O}$, and $^{18-27}\text{F}$) were done by Chulkov et al. [77]. The σ_{cc} values of all the stable nuclei in Ref. [77] are however greater than those of ref. [74] and also cannot be explained using the proton radii derived from electron scattering. Therefore, the data of Ref. [77] seems to have some systematic uncertainty. The proton radii were not determined from the measured σ_{cc} in Ref. [77]. The proton radii can be extracted from measured charge-changing cross-sections using the Glauber model framework. In the following section, the finite

range Glauber model theory is presented.

1.5 Finite range Glauber model

The proton radii can be extracted from the σ_{cc} using the Glauber model formalism [78]. The reaction cross section (σ_R) for a projectile-target collision is calculated by integrating the reaction probability with respect to the impact parameter \mathbf{b} and is given by

$$\sigma_R = \int [1 - T(\mathbf{b})] d\mathbf{b} \quad (1.10)$$

where $T(\mathbf{b})$ is the transmission function. It is the probability that, at the impact parameter \mathbf{b} , the projectile will pass through the target without interacting. The charge changing cross sections, on the other hand, involve the interaction of only the protons of the projectile nucleus, therefore σ_{cc} is given by

$$\sigma_{cc} = \int d\mathbf{b} P_{cc}(\mathbf{b}). \quad (1.11)$$

where $P_{cc}(\mathbf{b})$ is the probability of charge changing reaction at the impact parameter \mathbf{b} . $P_{cc}(\mathbf{b})$ is calculated using Optical Limit Approximation (OLA) [78, 79]. This model assumes that at sufficiently high energies, the nucleons carry sufficient momentum that they undergo small angle scattering (i.e. nearly undeflected) as the nuclei pass through each other. According to the Glauber model framework described in [80], $P_{cc}(\mathbf{b})$ is given by

$$P_{cc}(\mathbf{b}) = 1 - \exp \left(-2 \sum_{N=p,n} \iint d\mathbf{s} d\mathbf{t} T_P^{(p)}(\mathbf{s}) T_T^{(N)}(\mathbf{t}) \times \text{Re} \Gamma_{pN}(\mathbf{b} + \mathbf{s} - \mathbf{t}) \right) \quad (1.12)$$

where, \mathbf{s} is the two dimensional vector of the projectile's single-particle coordinate, \mathbf{r} , measured from the projectile's c.m. coordinate, and \mathbf{t} is defined for the target nucleus in a similar way. $T_P^{(p)}(\mathbf{s})$ is the thickness function of the projectile's proton density $\rho_P^{(p)}(\mathbf{r})$,

$$T_P^{(p)}(\mathbf{s}) = \int_{-\infty}^{\infty} dz \rho_P^{(p)}(\mathbf{r}) \quad ; \quad \mathbf{r} = (\mathbf{s}, z) \quad (1.13)$$

We evaluated the σ_{cc} with the finite-range profile function $\Gamma_{NN}(\mathbf{b})$ parametrized as [81]

$$\Gamma_{NN}(\mathbf{b}) = \frac{1 - i\alpha_{NN}}{4\pi\beta_{NN}} \sigma_{NN}^{tot} \exp\left(-\frac{\mathbf{b}^2}{2\beta_{NN}}\right) \quad (1.14)$$

The parameter α_{NN} is the ratio of the real to the imaginary part of the NN scattering amplitude, β_{NN} is the slope parameter of the NN elastic differential cross-section which in other words is the finite range parameter and σ_{NN}^{tot} is the total cross section for NN collisions. The values of α_{NN} , β_{NN} and σ_{NN}^{tot} are given in Ref. [81] for a wide range of energies. Hence, the proton radii of the projectile nuclei can be determined using these measured parameters of nucleon-nucleon cross sections and a target with a well known density distribution.

1.5.1 R_p determined from σ_{cc}

The proton radii determined from σ_{cc} are denoted by R_p^{cc} in what follows. Estrade et al. [82] deduced the R_p^{cc} of $^{10-17}\text{B}$ using a finite-range Glauber model analysis of σ_{cc} . A thick neutron skin of 0.51 ± 0.11 fm was observed in ^{17}B . A measurement of the charge-changing cross sections at 300A MeV had been done by Yamaguchi et al. [83]. In this case, the proton radii of ^{9-10}Be , $^{14-16}\text{C}$ and $^{16-18}\text{O}$ were determined using the zero range Glauber Model. They had to introduce a universal scaling of σ_{cc} to reproduce the proton radii from electron scattering measurements. However, in Ref. [82] no scaling was required to produce proton radii consistent with electron scattering measurements. The R_p^{cc} for $^{12-14}\text{C}$ [84] and ^{14}N [85] determined using the Glauber Model framework are consistent with point proton radii derived from electron scattering. These demonstrate the successful use of the finite range Glauber model to extract radii at 800-900A MeV. The measured R_p for carbon isotopic chain are shown in figure 1.11 (b). It is evident from the trend of proton radii determined from this measurement that there is an evolution of thick neutron surface from ~ 0.5 fm in ^{15}C to ~ 1 fm in ^{19}C . The halo radius of ^{19}C was determined to be 6.4 ± 0.7 fm, which is comparable to ^{11}Li . The radii of $^{13-18}\text{C}$ are also consistent with *ab initio* calculations based on the chiral nucleon-nucleon and three-nucleon forces.

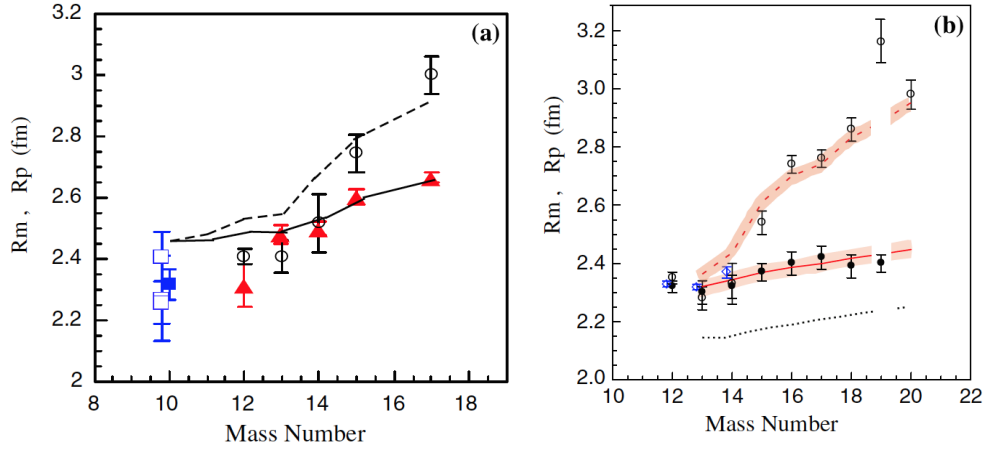


Figure 1.11: (a) The measured R_m (circles) and measured R_p^{cc} (triangles) for $^{12-17}\text{B}$ (b) The measured R_m (open circles) and measured R_p^{cc} (filled circles) for $^{12-19}\text{C}$. The blue symbols represent the measured R_p derived from e^- scattering. Figure taken from [82, 84].

1.6 This Work

We have measured the σ_{cc} of $^{16,18-24}\text{O}$ at energies of 800-900 MeV to determine the proton radii of these isotopes. The experiment was performed at high energy radioactive ion beam facility, GSI, in Germany. σ_{cc} were measured using the transmission type measurement. The details of the measurement principle, and the experimental setup are given in chapter 2.

The analysis of the data is discussed in chapter 3, which begins with the calibration of detectors followed by a discussion of all the physical observables required for the determination of σ_{cc} .

The chapter 4 describes the method employed to obtain the σ_{cc} using the measured physical observables. The extraction of the proton radii from the measured σ_{cc} using the Glauber model analysis is also discussed in this chapter. The chapter concludes with a discussion on the observed evolution of the proton radii as a function of the neutron number.

Chapter 2

Experiment Description

The experiment was performed at the fragment separator (FRS) [86] at GSI to measure the charge-changing cross sections of the oxygen isotopes [87]. GSI is a high energy radioactive ion beam facility in Darmstadt, Germany. It consists of a linear accelerator, UNILAC, coupled to a heavy-ion synchrotron, SIS. The primary beams, ^{40}Ar and ^{22}Ne , were accelerated in the UNILAC (2-20A MeV) and then re-accelerated in the SIS heavy ion synchrotron up to 1A GeV. A schematic view of the GSI-FRS facility is shown in figure 2.1. The $^{16-24}\text{O}$ secondary beams were produced by fragmentation

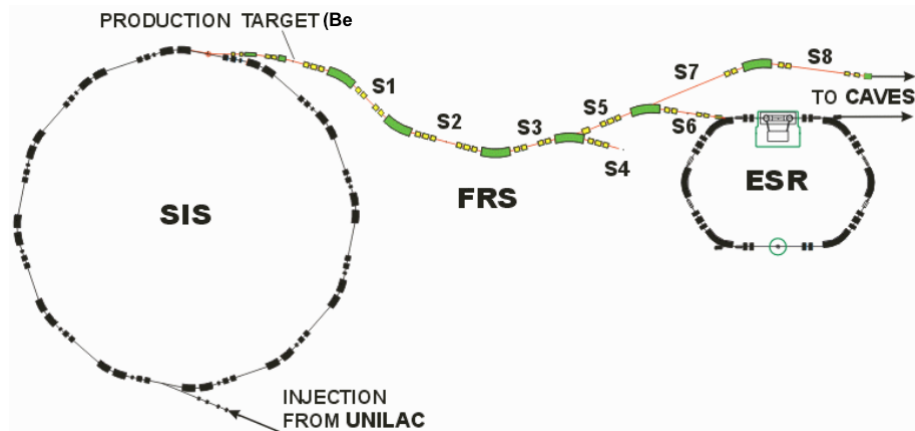


Figure 2.1: The schematic view of the GSI-FRS facility. Figure from [88].

reaction ($^{40}\text{Ar} + ^9\text{Be}$) using a 6.3 g/cm^2 thick Be target placed at the entrance of the Fragment Separator (FRS). The FRS is used to separate and identify the isotope of interest from the various nuclei produced in the fragmentation reaction. A description of the separation technique is given in the following section.

2.1 The fragment separator

The FRS is a high-resolution magnetic spectrometer designed to efficiently separate projectile fragments in their mass and nuclear charge with a maximum magnetic

rigidity of 18 Tesla meters (Tm). It consists of four independent stages. Each stage is comprised of a 30° dipole magnet and a set of quadrupoles placed before and after the dipoles. The quadrupole magnets in front of the dipole magnets are adjustable to illuminate the field volume of the dipole magnets to achieve a high resolving power. The quadrupole magnets following the dipole magnets determine the focusing ion-optical conditions. Sextuple magnets are placed directly in front of and behind each dipole magnet to correct for the second-order aberrations. The image of the FRS is shown in figure 2.2 which shows the magnetic dipoles (green) and the quadrupole magnets (yellow). The motion of the ions in the magnetic field is governed by the

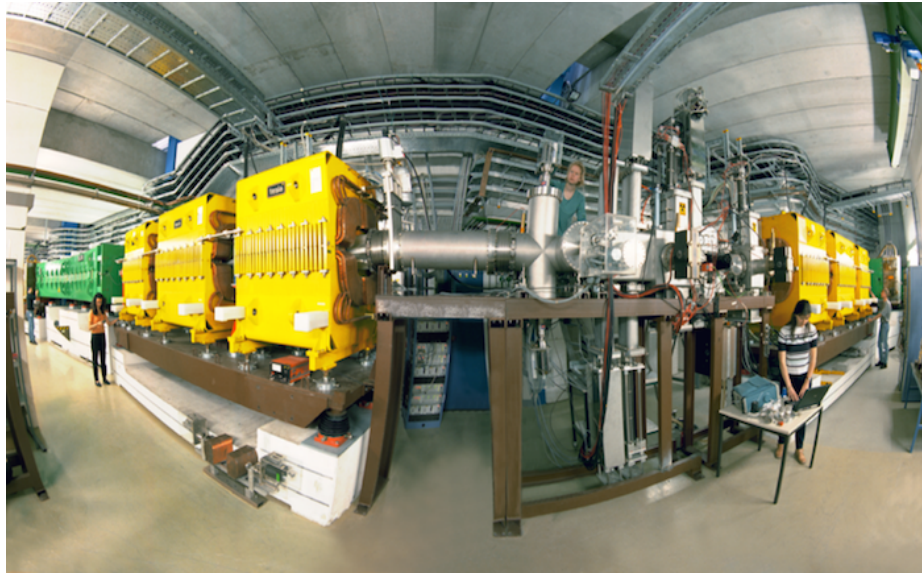


Figure 2.2: A photograph of FRS at GSI.

Lorentz force. The magnetic fields inside the dipoles are uniform and perpendicular to the velocity (v) of the fragments. Therefore, the Lorentz force (F) is given by:

$$F = qvB = \frac{mv^2}{\rho} = \frac{\gamma m_0 v^2}{\rho} \quad (2.1)$$

where q is the ionic charge state of the fragment, B is the magnetic field in the dipole, ρ is the radius of the trajectory, m_0 is its rest mass, and $\gamma = \sqrt{(1 - \beta^2)^{-1}}$ is the relativistic factor with $\beta = v/c$ (c is the speed of light). Equation 2.1 can be rearranged as:

$$\frac{m_0}{q} \approx \frac{A}{Z} = \frac{B\rho}{u\beta\gamma c} \quad (2.2)$$

where u is the atomic mass unit and charge, q , is equal to Z as we worked with fully stripped nuclei. The product $B\rho$ is the magnetic rigidity (χ) of a beam, a parameter defined as following

$$\chi = B\rho = \frac{p}{q} \quad (2.3)$$

where p is the magnitude of the particle momentum. The ratio of p to q describes the ‘stiffness’ of a beam, which can be considered as a measure of how much resistance to curvature or bending occurs when a particle travels through a given magnetic field. For a specific magnetic field, the greater the momentum of a particle, the less its path will be bent as it travels through that field. The greater the charge of a particle, the more its path will be bent as it travels through a given magnetic field.

The projectile-like fragments that enter the FRS are separated according to their magnetic rigidities and therefore according to their A/Z ratio. Fragments having higher velocities (larger A/Z ratio) follow the trajectory with a larger radius than the fragments having lower velocities according to equation 2.1. The FRS was operated in the dispersion matched mode where the dispersion of the first stage is matched with the dispersion of the second stage. The first stage χ is set for a particular A/Z and the second stage χ is set to converge the transmitted isotopes back to the same horizontal position. The combination of both stages becomes an achromatic system. It is useful to operate the FRS in this mode because rare isotopes have the small production cross sections, therefore the FRS must be able to capture a large fraction of the angular and energy range of the selected fragment. The schematics of basic principle of the FRS in dispersion matched mode is shown in figure 2.3. As the primary beam reacts with the target, the projectile fragments originate from a small beam spot at the target. The blue lines show the momentum spread of the fragments in figure 2.3 (top). The momentum spread of the fragment is dispersed in position at the dispersive focal plane (F2), which converges back to same horizontal position at achromatic focus (F4). Figure 2.4 shows the horizontal x position at F4 calculated using LISE code [89] for FRS centered for ^{16}O . In figure 2.4 (a) all fragments with same A/Z converge at nearly the same x position.

Such an ion-optical arrangement cannot separate different isotopes with the same A/Z ratio. A degrader is used to separate particles with the same A/Z ratio according to their Z values. The energy loss of the particles is roughly proportional to Z^2/v^2 ,

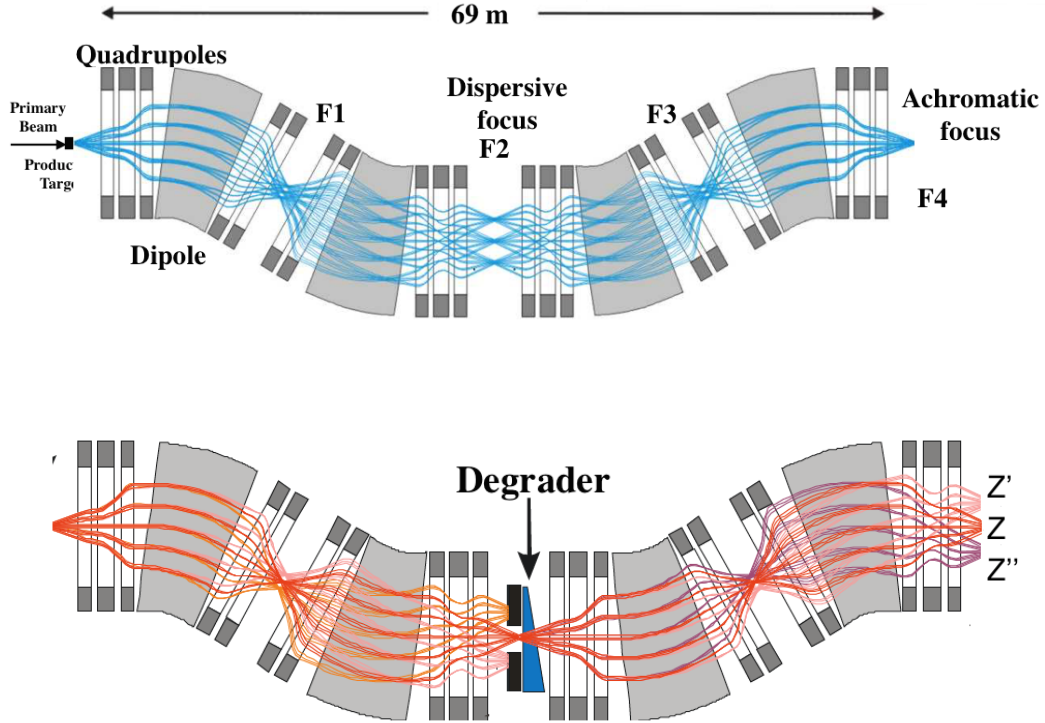


Figure 2.3: The schematic view of ion optics of the FRS.

therefore the isotopes with different Z will have different velocities after passing through the degrader as shown in figure 2.3 (bottom). Figure 2.4 (b) shows the x position at F4 with a wedge degrader added to the LISE calculation [89] where the same A/Z fragments are clearly separated in position. The wedge shaped degrader was used so that the fragments at a higher velocity pass through more degrading material and the lower velocity fragments pass through less material. In this way, the achromatic condition for the selected isotopes is preserved. The slits at four planes of the FRS are used to further cut down on the remaining contaminants. The optimum wedge thickness and slit conditions were found for each isotope using the LISE code to get a maximum yield of the desired isotope. The beam intensities for each setting of the FRS is given in the Table 2.1.

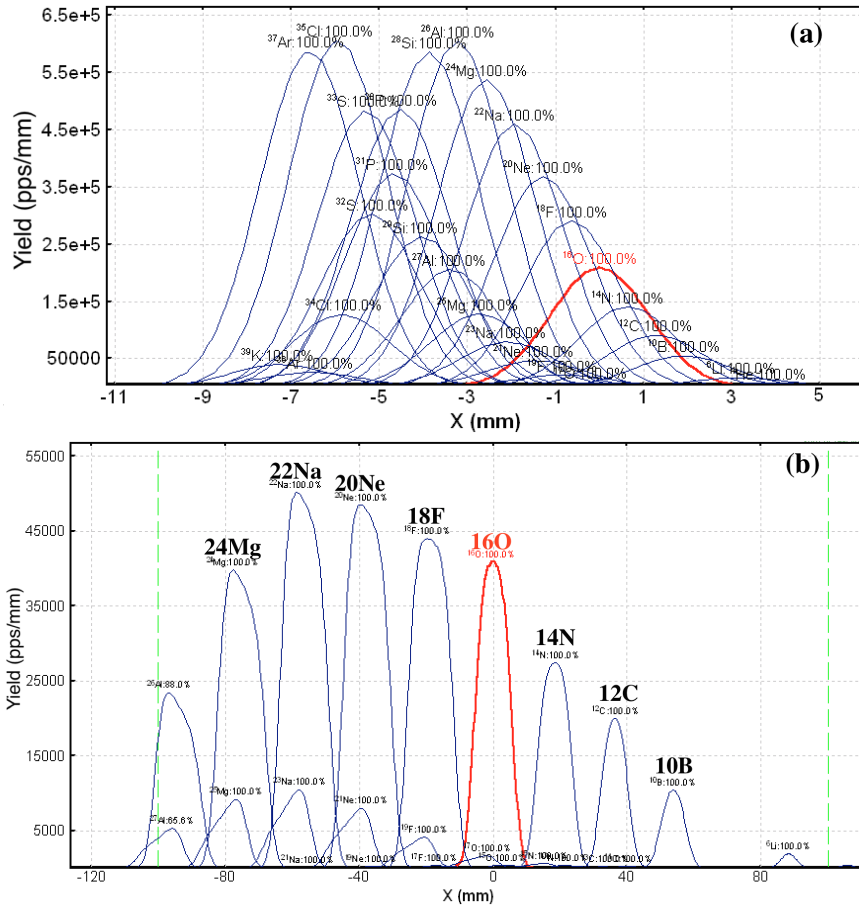


Figure 2.4: The position distributions in x of the various isotopes at the F4 using the LISE code (a) without degrader (b) with a wedge degrader.

Fragment setting	Spill length	Free trigger	Accepted trigger	Total SC41 rate	Isotope rate
	s	<i>counts/spill</i>			counts/s
^{16}O	10	7400	5500	7900	497
^{18}O	10	6600	5380	6250	415
^{20}O	5	3200	2600	3600	269
^{22}O	5	1601	1327	1601	37
^{23}O	5	2705	2349	4938	8
^{24}O	2	1702	1405	2402	3

Table 2.1: The beam intensity for each fragment setting of the FRS.

2.2 Principle of measuring charge-changing cross section

As discussed previously, σ_{cc} is the cross-section for reactions that decrease the atomic number of the projectile nucleus. σ_{cc} were measured by using the transmission method. In this method, the number of incident nuclei, identified in mass and charge, are counted event-by-event. After the reaction target, we count the number of nuclei whose Z numbers are unchanged, i.e. the number of nuclei transmitted without the charge-changing interactions.

As a beam of particles passes through matter, its intensity will be attenuated. The number of collisions per unit time per unit area is then proportional to the number of incident particles N_0 and the number of target particles. Then by definition, the constant of proportionality is the reaction cross-section σ_R . The reaction cross section σ_R is defined by [90]

$$N = N_0 e^{-\sigma_R t} \quad (2.4)$$

where N is the number of particles of the unreacted beam, t is the number of target nuclei per cm^2 . The charge-changing cross section σ_{cc} is defined analogously:

$$N_0 - N_Z = N_0 e^{-\sigma_{cc} t} \quad (2.5)$$

Here, N_Z denotes the number of particles per unit time that undergo a charge-changing reaction. $N_0 - N_Z$ consequently corresponds to the number of particles that emerge with unchanged charge which can be denoted as $N_{\text{same}Z}$. Thus, equation 2.5 can be written as

$$N_{\text{same}Z} = N_0 e^{-\sigma_{cc} t} \quad (2.6)$$

Counting the number of incoming projectiles N_0 and emerging $N_{\text{same}Z}$ particles, the total charge-changing cross section can be obtained by rearranging equation 2.6:

$$\sigma_{cc} = \frac{1}{t} \ln \frac{N_0}{N_{\text{same}Z}} \quad (2.7)$$

However, nuclear reactions may also occur in the non-target materials in the beamline and this effect is accounted for by taking measurements without the target in the

setup, therefore the σ_{cc} can be written as

$$\sigma_{cc} = \frac{1}{t} \ln \frac{R_{out}}{R_{in}} \quad (2.8)$$

where $R_{in} = N_{samez}/N_0$ is the transmission ratio with the reaction target and R_{out} denotes the transmission ratio without the reaction target. The main advantage of the method is the event-by-event counting of the selected incident beam. Therefore, no uncertainty exists in N_0 .

2.3 The detector setup

In order to count the incident nuclei before the reaction target, we needed to identify them. The nuclei of interest were identified using their magnetic rigidity, time of flight (F2 to F4) and energy loss. Details about how the particles were identified are given in section 3.3. The magnetic rigidity determination requires horizontal x position measurement at F2 and F4 for which the Time Projection Chambers (TPC) were used. The time of flight was measured using the plastic scintillator detectors at F2 and F4 and the energy loss was measured with a Multi-Sampling Ionization Chamber (MUSIC) placed at F4. The measurements performed with these detectors are summarized in figure 2.5 (b). σ_{cc} were measured with a 4.010 g/cm^2 thick carbon reaction target placed between the MUSIC detectors at F4. The detector setup and the carbon reaction target are shown in figure 2.5 (a). The detailed schematics of the detector setup at F2 and F4 along with detector distances is shown in figure 2.6, in which the detectors are labeled by the scripted names that will be used throughout the following chapters. The SC21 denotes the first scintillator detector at F2, SC41 denotes the first scintillator at F4 and SC42 denotes the second scintillator at F4. The MUSIC41 denotes the MUSIC before the target and MUSIC42 represents the MUSIC after the target. The TPC1, TPC2 and TPC3 are the three TPC's placed at F2. TPC4 and TPC5 were placed before the reaction target at F4 and TPC6 was placed after the reaction target at F4. The TPC and the plastic scintillator detectors placed after the reaction target provided additional information regarding Z of the particles. The correlation of energy loss in these detectors with the energy loss of MUSIC42 was used to determine the detection efficiency of MUSIC42. The detector

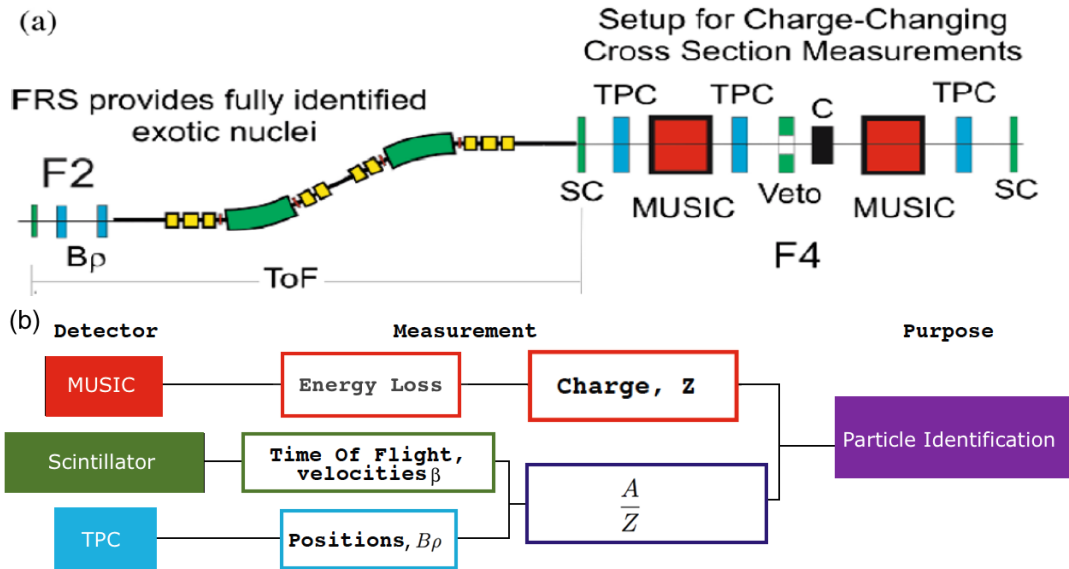


Figure 2.5: (a) A schematic view of the experimental setup at the FRS with the detector arrangement at the final focus F4. Fig. taken from [82].(b)A flowchart of measurements performed with the different detectors.

distances were measured from last quadruple at F4 and from the first quadruple at the end of F2. In the following sections, the characteristics of the detectors used in this experiment are described.

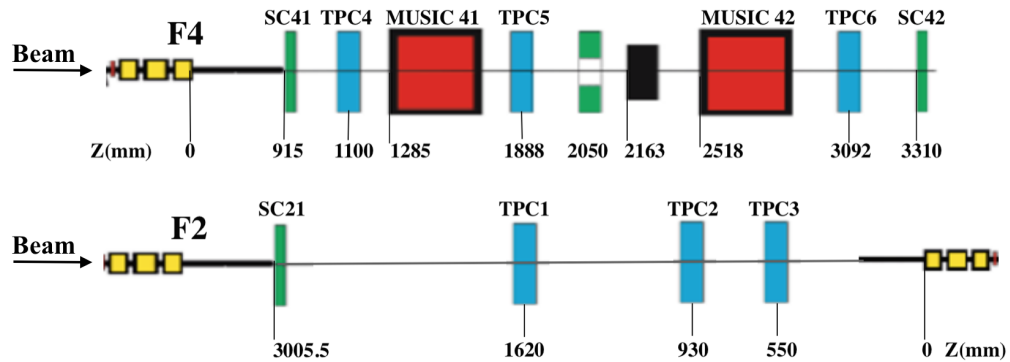


Figure 2.6: The detector setup at F2 and F4 with detector distances.

2.3.1 Multiple-sample ionization chambers

The charge of the particles were measured using MUSICs [91] placed before (MUSIC41) and after (MUSIC42) the carbon reaction target at F4. The MUSIC detector is an

ionization chamber with an active length of 400 mm along the beam axis, segmented into eight anode strips. Both the MUSIC detectors were filled with CF₄ gas and were operated at room temperature and atmospheric pressure. A side view of the detector

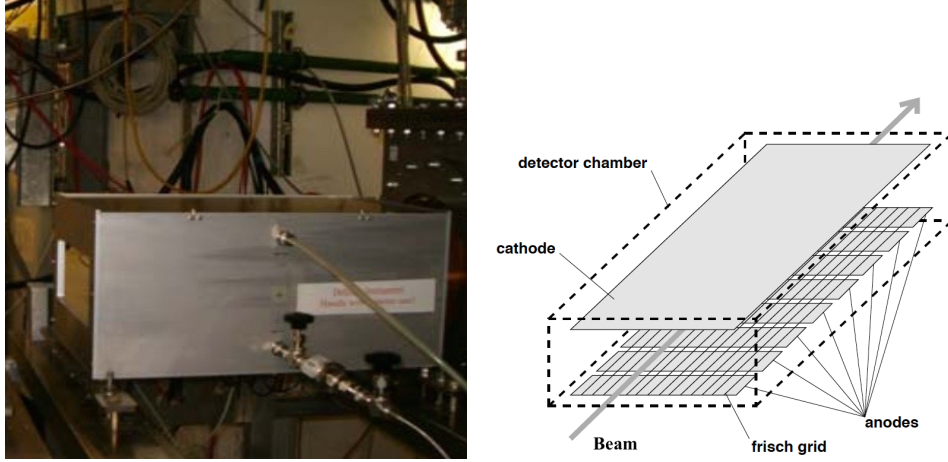


Figure 2.7: A picture of the MUSIC detector (left). Schematic view of the MUSIC detector (right).

and a schematic view of the internal geometry are shown in figure 2.7. The ionizing particles lose energy creating electron-ion pairs as they penetrate the gas. The number of electrons created is, to first order, proportional to the square of the charge of the penetrating particle. The specific energy loss of charged particles in a material as described by Bethe-Bloch is given by,

$$\frac{-dE}{ds} = \frac{4\pi Z_p^2}{m_e c^2 \beta^2} \left(\frac{e^2}{4\pi\epsilon_0} \right)^2 Z_t N_t \left(\ln \frac{m_e v^2}{I} - \ln(1 - \beta^2) - \beta^2 \right) \quad (2.9)$$

where s represents the path length of the particle in the absorber, Z_p and β correspond to the charge and the velocity of the penetrating particle. Z_t , N_t and I are the proton number, the particle density and the mean excitation potential of the material, respectively. Finally, e and m_e are the charge and mass of the electron [92]. Electrons start drifting towards segmented anodes in the electric field and get collected there. The charge-sensitive preamplifiers convert their charge into a proportional signal amplitude. The geometric average of the eight anode signals was taken to obtain charge information.

2.3.2 Time projection chambers

The particle positions in the horizontal (x) and vertical (y) directions were measured using TPC [93]. Six TPCs were placed along the FRS: three were placed at the dispersive focus (F2) and three at the achromatic focus (F4). These detectors have a good spatial resolution with best achieved internal resolution of $\sigma_x \approx 88 \mu\text{m}$ and $\sigma_y \approx 38 \mu\text{m}$ for ^{40}Ar beam. The TPC detector has a smaller volume of matter in the path of the beam. This is useful because they are placed at F2 and every layer of matter at F2 degrades the resolution of the spectrometer. The schematic layout and a picture of the detector are shown in figure 2.8. The red grid shown in front of the detector in figure 2.8 (right) is made of scintillator strips used for the position calibration of the detector. Each TPC is a gas detector that is comprised of two different parts -

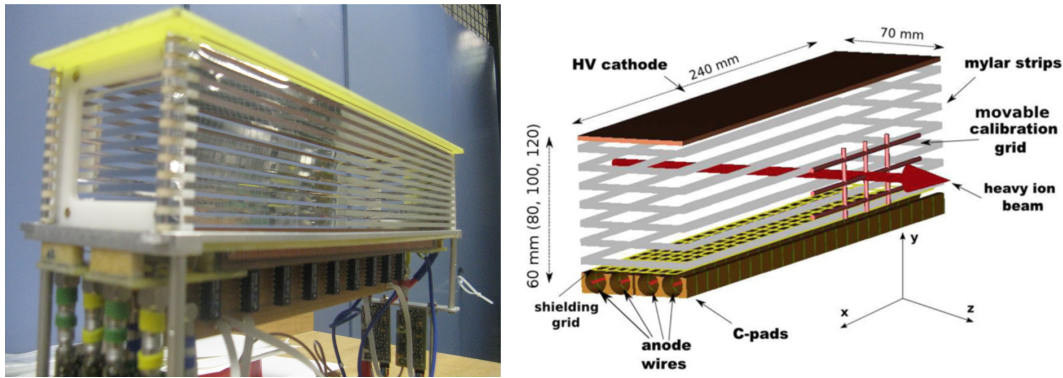


Figure 2.8: A picture of the detector on the left. A schematic view of a Time-Projection Chamber (TPC) (right). Figure adapted from [94].

a drift space and a proportional area. The drift space is formed by a high-voltage cathode and field-forming mylar strips. The mylar strips are connected to a high resistance divider. A voltage of up to 400 V/cm is applied to the divider to form a uniform electric field inside the drift volume. The drift volume is filled with Ar + 10% CH₄ (P10) gas mixtures at atmospheric pressure and room temperature. The proportional part is placed under the drift space and is separated by a shielding grid. It consists of four anode wires (20 mm in diameter) placed inside C-pad cathodes as shown in figure 2.8 (right). Each C-pad is connected to an integrated passive delay line chip. As an ionizing particle passes through the detector, it creates a shower of electrons along its track that drift towards the anode wires. A common start is provided by the FRS trigger, which was the time signal from SC41 for this experiment.

The electrons drift towards the anode, creating the stop signals in the anodes. Each

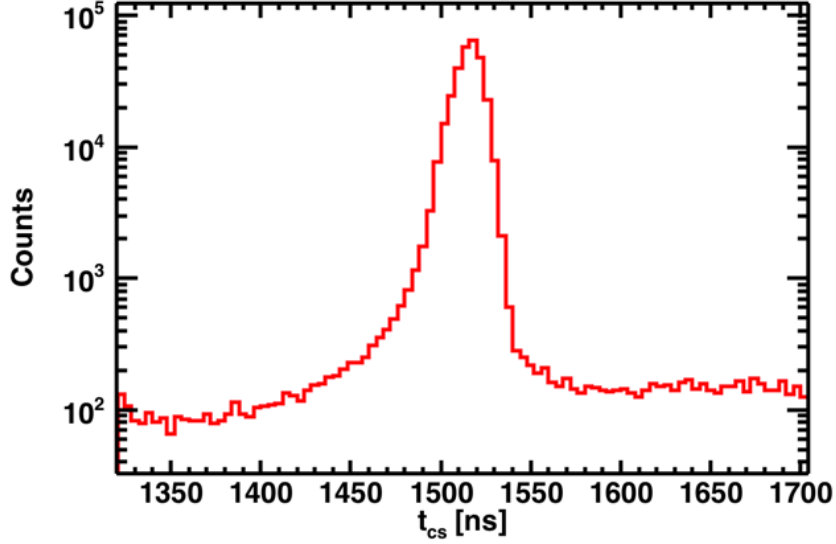


Figure 2.9: The control sum distribution using the delay line 1 and anode 1 for TPC6.

TPC measures four anode times t_{a1} , t_{a2} , t_{a3} , t_{a4} . The electron drift times are used to measure the y -coordinate of the ionizing particle. The induced signals in the delay line travel to the left and the right and give the stop signals of the delay lines. The x -coordinate of the ionizing particle is determined by using the time difference between the induced signal from the left and the right side of each delay line. Two independent x measurements are produced by two independent delay lines times $t_{dl}(left)$ and $t_{dr}(right)$. The detailed description of how position information is obtained from time signals in TPC is discussed in section 3.1.3 in the next chapter. The time signals are also used to discard noisy signals as the total delay line length is a constant (C). The control sum which is given by equation 3.7

$$t_{csi} = t_{dl} + t_{dr} - 2t_{ai} = C \quad (2.10)$$

should therefore be equal to the total delay line length. t_{csi} can be computed for each of the four anode times t_{ai} ($i = 1, 4$) separately. The control sum distribution using the delay line 1 and anode 1 for TPC6 is shown in figure 2.9. The RMS of the control sum distribution is $\sigma_{cs} \approx 7$ ns. This width is mainly due to the two-dimensional (total)

resolution of the TPC. The events which fulfil the control sum within $3\sigma_{cs}$ were used. The particle position was accepted if at least one of the four control sums was within $3\sigma_{cs}$.

2.3.3 Plastic scintillators

The time-of-flight measurement (TOF) was performed using the plastic scintillator detectors [95]. A scintillator detector absorbs the energy of an incoming particle and re-emits the absorbed energy in the form of light. A light sensor collects the light and converts it into electric pulses that can give us information about the time and energy deposited of ionizing particles. Three plastic scintillators were used for the experiment: one was placed at F2 (SC21) and other two were placed at F4, one before (SC41) and another after (SC42) the reaction target. The organic scintillator BC420 was used, which provides a high light output (67% Anthracene) and a fast rise time (0.5 ns). The readout was obtained with two Photo-Multiplier Tubes (PMTs) each attached on the left and the right side of each plastic scintillator. The anode signals of the PMTs were fed into the constant-fraction discriminators (CFD). The digital outputs of these units served to start and stop the time-to-analog converters (TAC). An analog signal corresponding to the time difference between the two signals is generated which is digitized by the amplitude-to-digital converter (ADC) and processed by the data acquisition. In order to limit the data just to events where the scintillator signal from both the detectors at F2 and F4 are present, the SC41 signal was used as the start signal while SC21 was delayed and used as the stop signal in the TAC. The details of TOF measurement and TAC calibration are given in chapter 3. The attenuated analog signals of the photomultipliers, available as outputs from the CFD, were used to measure the energy loss of the particles in the plastic scintillator.

2.3.4 Veto scintillator

A scintillator was placed right in front of the carbon reaction target, which acted as an active veto detector to remove the unwanted events from the off-line analysis. The veto scintillator has a central aperture slightly smaller than the reaction target area. An image of veto scintillator is shown in figure 2.10 where the area marked on white paper shows the location and area of the aperture. The readout was obtained from



Figure 2.10: A photograph of the veto plastic scintillator.

PMTs attached to the left and right side. The beam passed through the aperture and

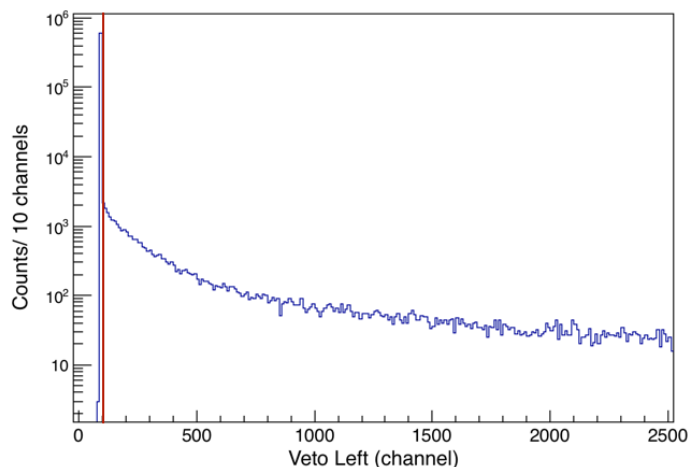


Figure 2.11: The energy loss in left PMT of the veto detector.

reacted with the target. The signals detected in either PMT correspond to the events incident near the edge of the reaction target and should be rejected. The signals might also come from particles scattered by nuclear reactions in matter upstream. The energy loss signal from left PMT of the veto detector for the ^{16}O is shown in figure 2.11. The events on the right-hand side of the red line represent events above the pedestal. The signals detected above the pedestal in either PMT were rejected from the selection of incident beam events for each isotope.

Chapter 3

Data Analysis

The raw data collected from the detectors is stored in the form of digital signals in ADC (Analog to Digital converters), TAC (Time to Analog converters) or TDC (Time to Digital converters) etc. In order to get physical observables of interest, one needs to find the conversion constants between the ADC channel numbers and the energy deposited in a particular detector, i.e. to perform detector calibrations. In the first few sections of this chapter, the calibration procedures of all of the detectors are discussed. The determination of σ_{cc} requires the identification of particles before and after the reaction target. All of the physical observables required for particle identification are discussed in detail in this chapter. In the last section of the chapter, the phase space restriction of the incident beam on the target is discussed.

3.1 Detector calibration

At first, the calibration of the MUSIC detectors is discussed, followed by the time of flight and TPC calibration.

3.1.1 Calibration of the MUSIC detectors

The MUSIC detectors were used for Z -identification of the particles passing through them. The calibration of the MUSIC detectors was done to associate the energy loss in channels with Z of the particles using a ^{12}C secondary beam ($A/Z = 2$). As discussed earlier, the energy lost by the incident particle in the MUSIC is proportional to the square of its charge. Therefore, the channel number (*ch.no.*) is related to Z^2 according to the following equation

$$Z^2 = g(\text{ch.no.}) + o \quad (3.1)$$

where g is the factor that converts channel into energy and o is the offset. The ^8Be nucleus is unbound, therefore the missing peak in energy loss spectrum when the FRS

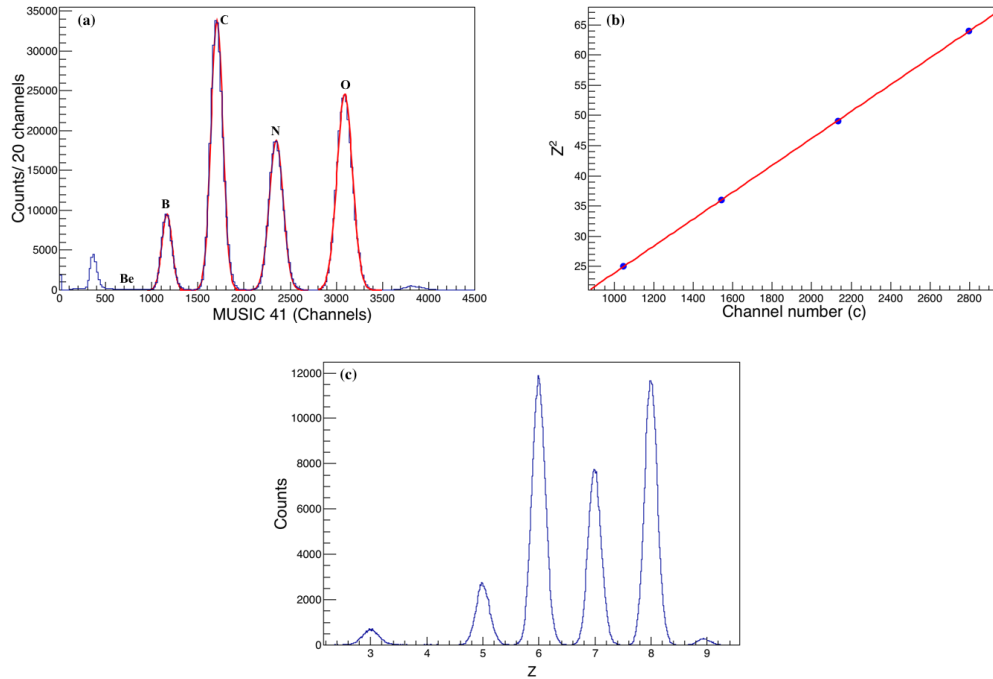


Figure 3.1: (a) The uncalibrated MUSIC41 spectrum for the ^{12}C secondary beam. Each peak is fitted with a Gaussian function (red curve). (b) A linear fit of Z^2 versus the mean channel number of the peaks. (c) The calibrated Z spectrum of the MUSIC41 detector.

is set for $A/Z = 2$, should correspond to $Z = 4$. This was used as a reference to identify the Z number associated with the energy loss peaks of the different particles. As we see in figure 3.1 (a) the four peaks after the missing peak should correspond to B, C, N and O. In order to get the mean, each peak was fitted with a Gaussian function shown by the red curve in figure 3.1 (a). The linear fit of Z^2 vs the mean channel number is shown in figure 3.1 (b). The calibrated Z spectrum of MUSIC41 using the slope and intercept from the linear fit is shown in figure 3.1 (c). The Z resolution of this detector was $\Delta Z = 0.11$ (in σ) for oxygen. Similarly, MUSIC42 detector was calibrated and the calibration is shown in figure 3.2. The Z resolution of MUSIC 42 was also found to be $\Delta Z = 0.11$ (in σ) for oxygen.

3.1.2 Time of flight calibration

As mentioned in the previous chapter, the time of flight (TOF) of the fragments was determined with PMTs attached on the left and the right side of the scintillator

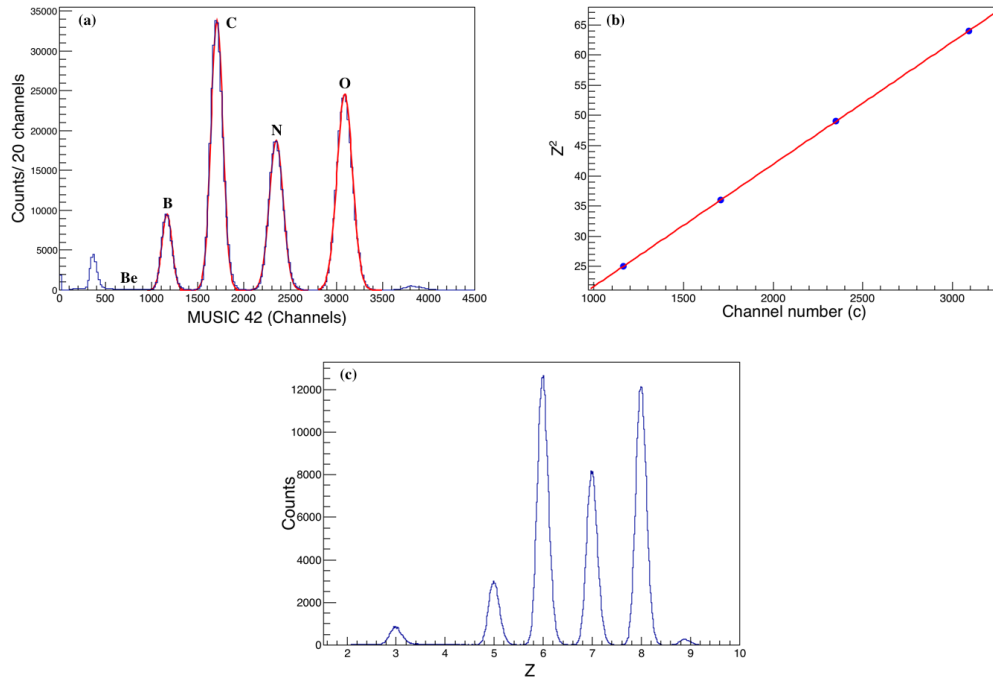


Figure 3.2: (a) The uncalibrated MUSIC42 spectrum for the ^{12}C setting. Each peak is fitted with a Gaussian function (red curve). (b) A linear fit of Z^2 versus the mean channel number of the peaks. (c) The calibrated Z spectrum of the MUSIC42 detector.

detectors. The TOF_{RR} i.e. the TOF from the right PMT of SC41 to the right PMT of SC21 was obtained considering the quantity

$$TOF_{RR} = |T_{41R} - T_{21R}| \quad (3.2)$$

where T_{41R} is the signal detected in the right PMT of SC41 and T_{21R} is the signal detected in the right PMT of SC21. Similarly, TOF_{LL} was obtained using

$$TOF_{LL} = |T_{41L} - T_{21L}| \quad (3.3)$$

where T_{41L} is the signal detected in the left PMT of SC41 and T_{21L} is the signal detected in the left PMT of SC21. The digitized PMT signal T_{41R} gave the start signal, while T_{21R} gave the stop signal in the TAC. The TOF information from the TAC is in the form of channels. The TOF_{RR} in channels is denoted by R_C and TOF_{LL} in channels is denoted by L_C in what follows. An independent measurement with a ORTEC Model 462 time calibrator unit was performed to calibrate the channels of

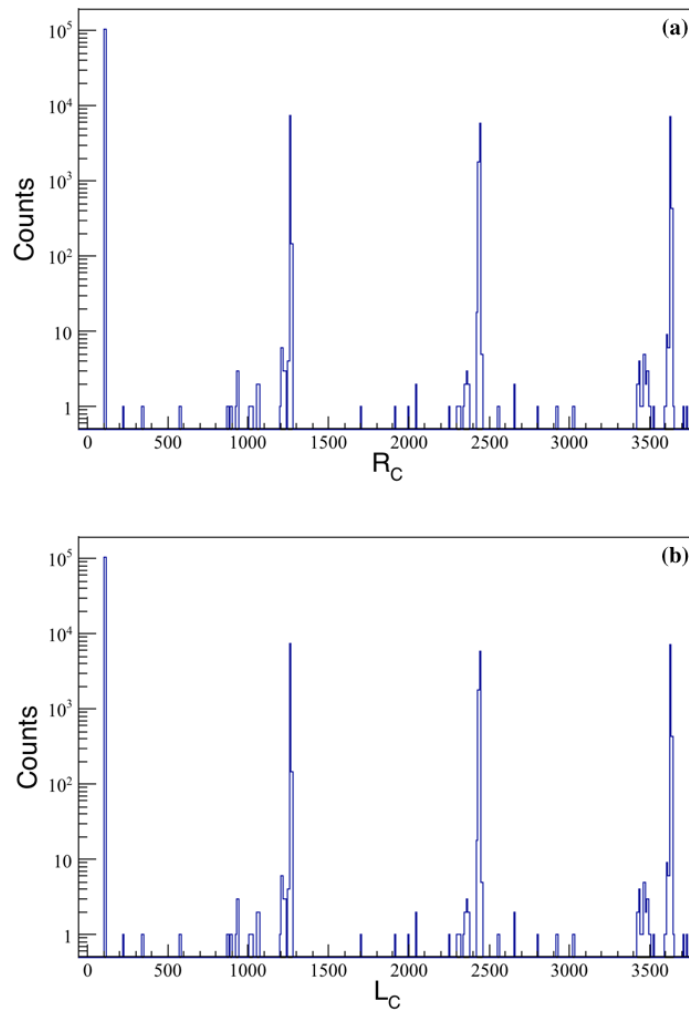


Figure 3.3: The TAC spectrum for 10 ns pulses from the TAC calibrator (a) TOF_{RR} in channels (R_C) (b) TOF_{LL} in channels (L_C).

TAC into nanoseconds. The time calibrator unit has switches to select the interval steps between start and stop signals and also switches to set the calibration time scale. Figure 3.3 (a) and (b) show the TAC spectrum for pulses of 10 ns duration from TAC calibrator unit for R_C and L_C , respectively. The correlation plot of R_C versus TOF_{RR} in nanoseconds (R_{ns}) is shown in figure 3.4 (a). The calibration factors are obtained by a linear fit and are listed in table 3.1. The calibrated TOF is determined using the following equation:

$$R_{ns} = G_R R_C + O_R \quad (3.4)$$

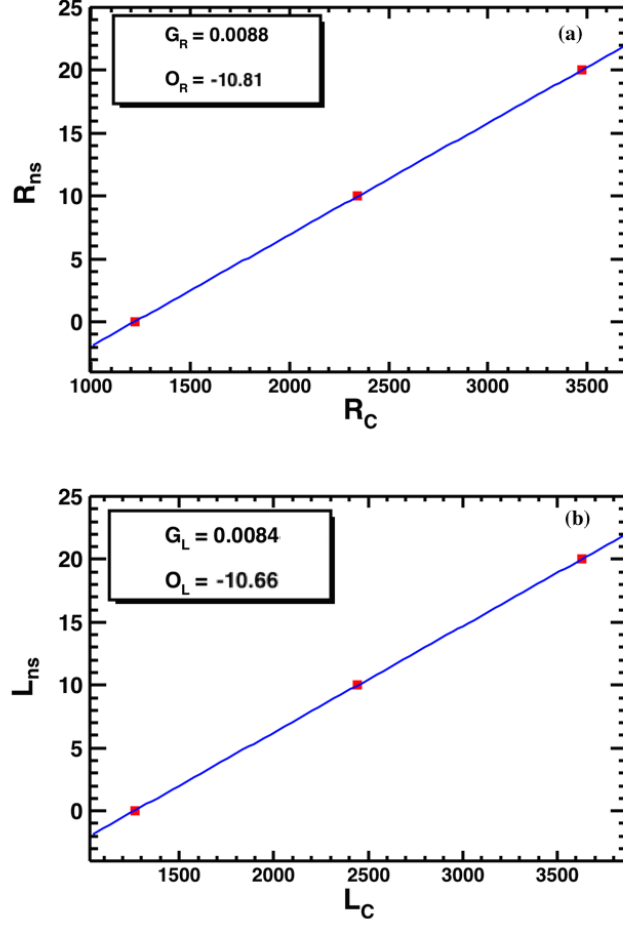


Figure 3.4: (a) The linear fit of R_{ns} (TOF_{RR} in ns) versus mean R_C (TOF_{RR} in channels). (b) The linear fit of L_{ns} (TOF_{LL} in ns) versus mean L_C (TOF_{LL} in channel).

where G_R represents the gain and O_R represents the offset of R_C . A similar, plot for L_C calibration into L_{ns} (TOF_{LL} in ns) is shown in figure 3.4 (b). The time difference in the left and right PMTs of the same scintillator was also calibrated using the procedure mentioned above and the calibration parameters for this time difference of all three scintillator detectors are given in table 3.1. The average of R_{ns} and L_{ns} was used as the final TOF in order to correct for the position of particle interaction in the scintillator.

$$TOF = \frac{R_{ns} + L_{ns}}{2} \quad (3.5)$$

SC Dt	Gain (<i>ns/ch.no.</i>)	offset (<i>ns</i>)
TOF_{LL}	0.0084	-10.662
TOF_{RR}	0.0089	-10.810
SC_{L-R}^{21}	0.0054	-10.440
SC_{L-R}^{41}	0.0056	-5.565
SC_{L-R}^{42}	0.0055	-10.360

Table 3.1: The parameters for TAC calibration for the Scintillator detectors.

To deduce an absolute value of the TOF, an absolute TOF offset (O) must be subtracted from the measured TOF . The TOF offset is determined by the measurement of the TOF of the primary beam with exactly known energy. The TOF of three

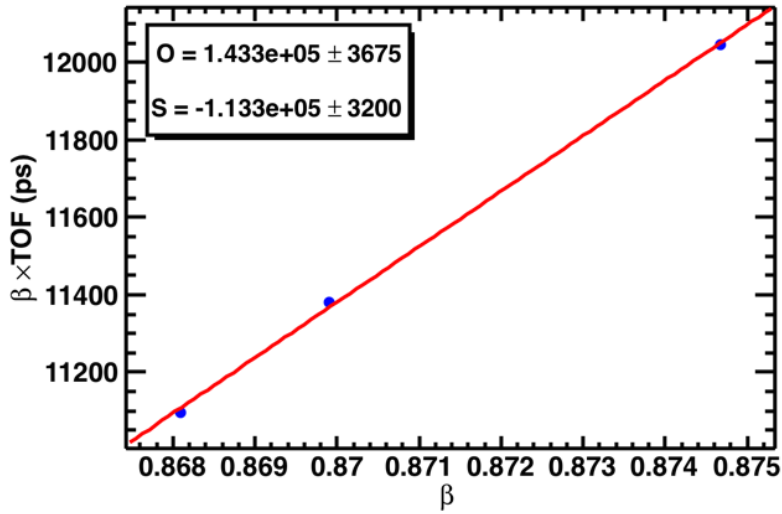


Figure 3.5: Linear fit of $TOF \times \beta$ versus β . The slope of the linear fit is the TOF offset (O) and intercept (S) is the flight path.

different velocities (β) of the ^{22}Ne primary beam was measured and the value of O was determined according to this equation:

$$\frac{S}{\beta} = TOF - O \quad (3.6)$$

where S is the flight path of the particles. If the above equation is rearranged as

$$\beta \times TOF = O\beta - S \quad (3.7)$$

then the linear fit of the product $\beta \times TOF$ versus β can be used to determine O and S as shown in figure 3.5. The slope of the linear fit is the O and intercept is S .

3.1.3 TPC calibration

In our experiment, we used an active scintillator grid to calibrate the TPC detectors.

The active scintillator grid consisted of thin scintillator fibers of 1 mm thickness, three vertical scintillator fibers placed at intervals of 12 mm between them, and three horizontal scintillator fibers placed with interfiber spacings of 6 mm. The scintillator grid was inserted in the path of the beam in front of the TPC only for the calibration that was done before the experiment and was retracted from the beam axis during the experiment. The schematics of the scintillator grid is shown

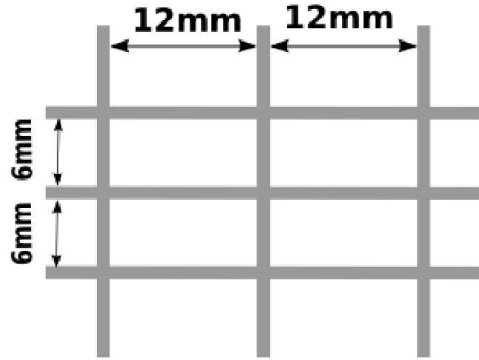


Figure 3.6: The scheme of scintillator plastic fibers used for the calibration of TPCs.

in figure 3.6. The scintillator grid was placed in front of each TPC. As discussed in chapter 2, the y -coordinate is determined by the electron's drift time measured by the anodes, while the x -coordinate is determined by using the difference between the induced signal in the left and the right side of delay lines. Figure 3.7 (a) shows the difference between left and right signals of delay line 1 (dl_1) of TPC6 with no condition from the grid. The same spectrum with scintillator grid coincidence is shown in figure 3.7 (b). The peaks were fitted with a three-Gaussian function which is represented by the red curve. The scintillator grid has x -positions at -12 mm, 0 mm and 12 mm and y -positions at -6 mm, 0 mm and 6 mm. The mean of each peak in figure 3.7 (b) is correlated to the corresponding x -positions of the grid. The linear fit of the correlation plot for the delay line 1 is shown in figure 3.7(c). A similar procedure was followed for each delay line and each anode for all of the six TPCs. Once we have the linear fit parameters, the x and y coordinates in mm are obtained using the following equations:

$$x = \frac{(dl_1 m_1 + c_1) + (dl_2 m_2 + c_2)}{2} \quad (3.8)$$

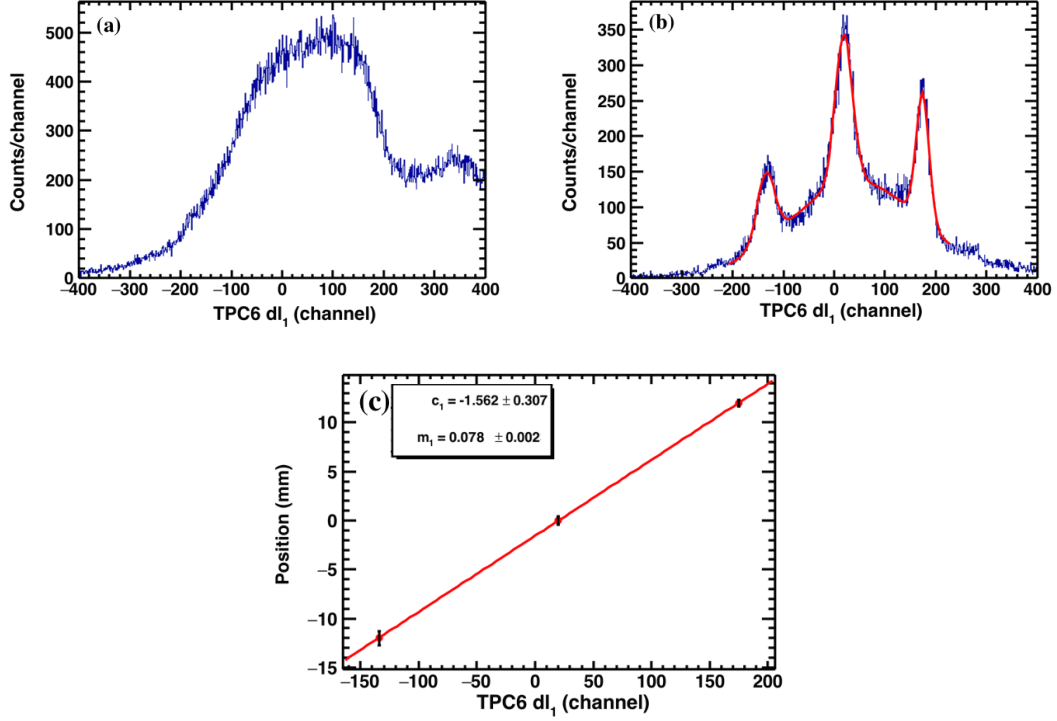


Figure 3.7: (a) The TPC delay line 1 spectrum with no condition. (b) The delay line spectrum with the scintillator grid coincidence with peaks fitted with a three-Gaussian function (red curve). (c) The linear fit of the mean of the peaks in channels vs. corresponding position in mm.

$$y = \frac{(dt_1 a_1 + o_1) + (dt_2 a_2 + o_2) + (dt_3 a_3 + o_3) + (dt_4 a_4 + o_4)}{4} \quad (3.9)$$

where dl_1 and dl_2 are the difference between left and right signal of two delay lines of a TPC and dt_{1-4} are the time signals of the four anodes of a TPC. The $m_{1,2}$ and $c_{1,2}$ represent the linear fit parameters corresponding to the gain and offset of each delay line whereas a_{1-4} and o_{1-4} represent linear fit parameters corresponding to gain and offset of each anode. In figure 3.8 the calibrated x (mm) vs. y (mm) plot for TPC6 is demonstrated where the structure of the grid is visible. It can be observed that after the calibration all of the particles are nicely aligned to their expected positions. The calibration parameters for delay lines and anodes of all of the TPC detectors are given in table 3.2.

TPC	gain (mm/ch.no.)						offset (mm)					
	m1	m2	a1	a2	a3	a4	c1	c2	o1	o2	o3	o4
1	0.070	0.069	-0.036	-0.037	-0.036	-0.036	-0.776	2.735	33.590	33.220	32.720	32.510
2	0.067	0.069	-0.042	-0.042	0.041	0.042	0.640	2.419	34.780	34.870	-42.140	-42.380
3	0.069	0.068	-0.036	-0.035	-0.035	-0.036	1.054	5.106	43.580	43.140	42.900	42.970
4	0.071	0.073	-0.040	-0.040	-0.040	-0.040	1.981	-1.316	32.470	32.370	30.850	30.840
5	0.068	0.068	-0.034	-0.034	-0.033	-0.034	-0.063	0.245	27.020	26.810	26.010	26.070
6	0.078	0.077	-0.039	-0.039	-0.039	-0.039	-1.562	-1.040	30.530	30.590	31.170	31.470

Table 3.2: The position calibration parameters for anodes and delay lines of TPC₁₋₆.

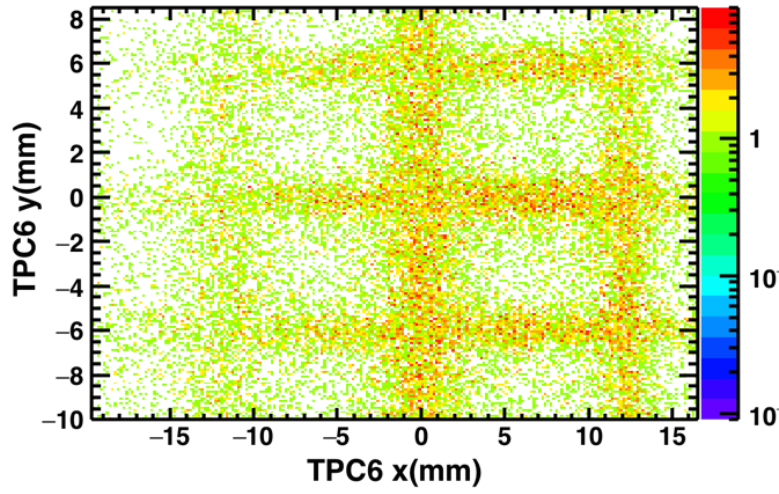


Figure 3.8: The calibrated correlation plot of x (mm) vs. y (mm) of TPC 6 showing the structure of scintillator grid.

3.2 Particle identification

The identification of the incident particles is one of the critical parts of the data analysis. To identify a particular nucleus, its charge and mass number must be known. The Z of the nuclei was determined from energy loss measured with the MUSICs. The mass number information is contained in the mass-to-charge ratio which is related to the motion of the ions in the magnetic dipole fields of the FRS according to equation 2.2. The value of χ was determined event-by-event to identify the nuclei. The magnetic rigidity associated with the trajectories of each of the nuclei for the second stage of FRS, χ_{F2} , is given by

$$\chi_{F2} = \chi_{central} \left(1 - \frac{M_B x_{f2} - x_{f4}}{D_B} \right). \quad (3.10)$$

where $\chi_{central}$ is the magnetic rigidity of the central trajectory, M_B and D_B represent the magnification and the dispersion of the second stage of FRS. The variables x_{f2} and x_{f4} are the horizontal position coordinates of the nuclei at F2 and F4 focal planes. We required only the magnetic rigidity of the second stage of the FRS because the reaction target was placed at F4 and therefore the particle identification was required at F4 only. The location of focal planes was determined by beam tracking using the TPC detectors and is discussed in the following section. The magnetic rigidity of the central trajectory $\chi_{central}$ was determined from the magnetic fields of the dipoles measured by the Hall probes. The effective radius of the central trajectory was calculated using the centered primary beam with a well-known energy. The dispersion (D) corresponds to the change of the horizontal position of the fragment if the magnetic rigidity of the fragment differs by 1%. It is written as the following.

$$D = \frac{dx}{d(B\rho)/(B\rho)} \quad (3.11)$$

The value of dispersion D_A (D_B) in the first (second) stage was determined experimentally with the primary beam. The magnetic field in the first (second) stage of the FRS was changed in small steps, and the corresponding change in x_2 (x_4) positions of the beam was measured. D_A and D_B were found to be -6.47 cm/% and 7.71 cm/% resp. The magnification (M_B) is the ratio of D_B to D_A , which equals 1.19 in our case.

3.2.1 Location of focal planes

The position information from the TPC detectors was used to obtain the horizontal x position of each particle at the F2 and F4 focal planes. The angles were evaluated using the x position from the TPCs and the detector location (z). The angles and coordinates of foci were found in the following way. The position coordinates of six TPC detectors can be considered as (x_i, z_i) where index i represents the TPC number, which runs from 1 to 6. The detector distances are shown in figure 2.6. The equation of a straight line in xz plane at TPC4 (x_4, z_4) can be written as

$$x_4 = m_4 z_4 + c \quad (3.12)$$

The slope of the beam at F4, using the measured positions, x_4 and x_5 of TPC4 and TPC5, respectively, is given by

$$m_4 = \frac{x_5 - x_4}{z_5 - z_4} \quad (3.13)$$

and the intercept can be solved as

$$c = x_4 - m_4 z_4 \quad (3.14)$$

If we consider the coordinates of focal plane at F4 as x_{f4} and z_{f4} then the straight

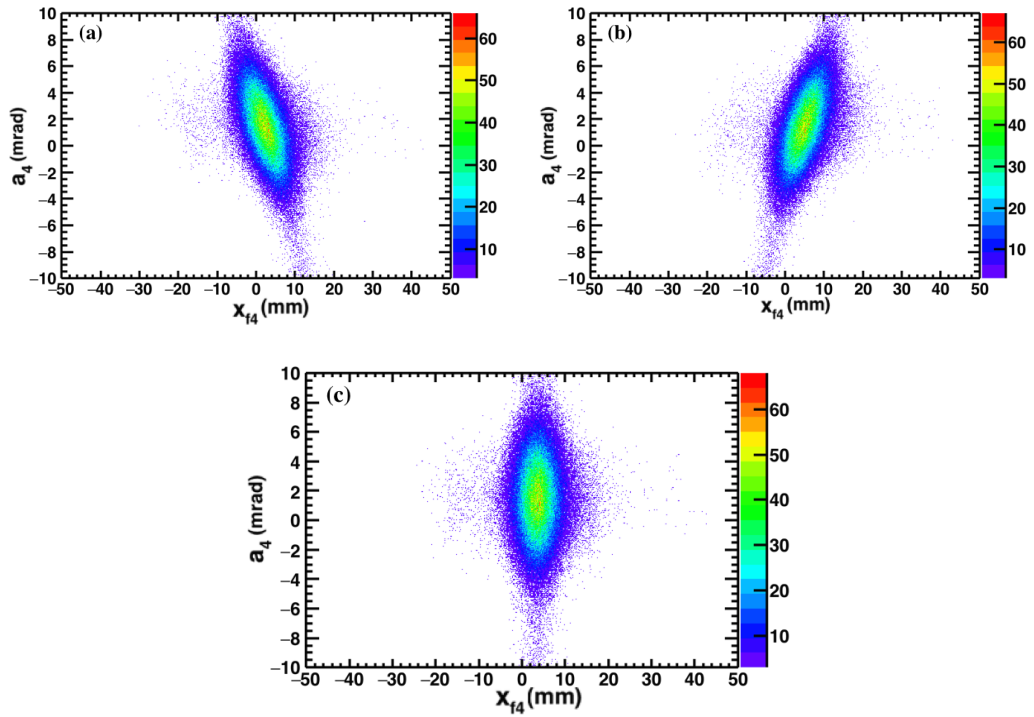


Figure 3.9: The correlation between the angle x (mrad) and the x position (mm) at
(a) One meter before the focal plane (b) One meter after the focal plane (c) At the focal plane at F4 region.

line equation at these coordinates can be written as

$$x_{f4} = m_4 z_{f4} + c \quad (3.15)$$

Using m_4 and c from eq. 3.13 and eq. 3.14, in eq. 3.15, we get x_{f4} as

$$x_{f4} = m_4(z_{f4} - z_4) + x_4 \quad (3.16)$$

In a system with point-to-point imaging, the horizontal position should not depend on the angle. To investigate this, the correlation spectrum of the angle at F4 (a_4) versus x_{f4} of the particle of interest at different z_{f4} locations was observed. If the condition $(x|a) = 0$ is fulfilled, the correlation plot should reflect the position x_{f4} being independent of angle a_4 . Consequently, the x -distribution should be narrowest at this z position. Figure 3.9 shows this correlation spectrum for three different z_{f4} , (a) one meter before the focal plane (b) one meter after the focal plane and (c) at the focal plane for ^{16}O . It can be observed in figure 3.9 (c) that the x distribution is independent of angle.

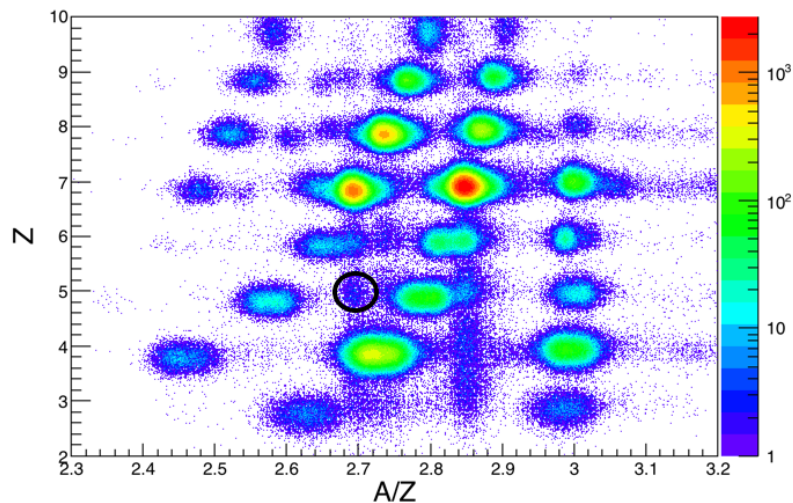


Figure 3.10: (a) The identification plot for the ^{23}O setting. The black circle shows an example of background events.

Therefore, with all of the necessary physical quantities, the A/Z ratio could be determined using Eq. 2.2. The identification of the particles was achieved by using the correlation plot of Z versus A/Z . Figure 3.10 shows the PID plot for the ^{23}O secondary beam. Some background events are clearly visible. One example is shown by the black circle; these events with $Z = 5$ and $A/Z = 2.68$ would result in a non-integer mass number. Therefore, we need to identify and reject such background events from

the PID. There are several reasons which can be accounted for the appearance of these events for example the reactions happening in the scintillator material placed before the target, or multiple scattering events. The first rejection was done using the veto detector. The correlation of the energy loss signal of the left PMT of the veto detector ($Veto_L$) vs the energy loss signal of the right PMT ($Veto_R$) for ^{23}O is shown in figure 3.11. The signals detected above the pedestal in energy loss signal of either PMTs were rejected. The PID spectrum after the veto rejection is shown in figure 3.12.

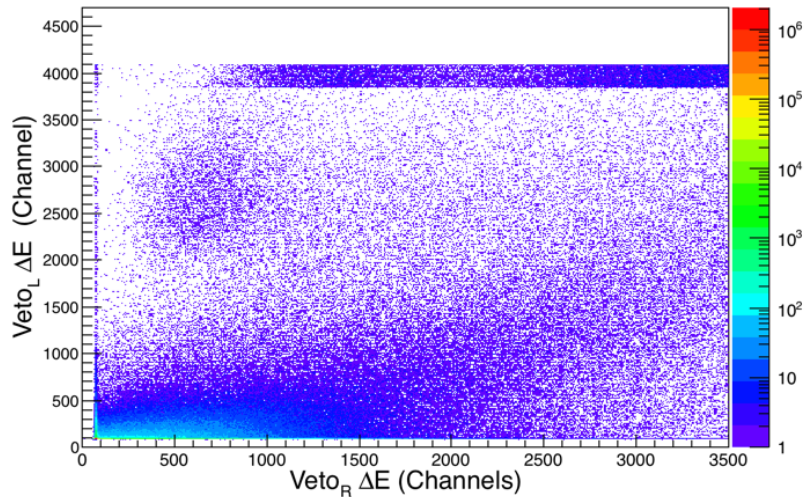


Figure 3.11: The correlation of $Veto_L$ vs. $Veto_R$ for the ^{23}O secondary beam.

After the rejection using the veto detector, the remaining background events were rejected by investigating different correlations of energy and the time signals among different detectors. The energy loss signal of one detector should be linearly correlated to energy loss signal of the other detector for the real events. Figure 3.13 shows the energy loss signal in the MUSIC41 detector vs energy loss signal in the TPC4 detector. The black contour represents the selection region of good events. Similar rejections were done using the energy loss signals from the TPC5 and MUSIC41 detectors as well as the SC41 and MUSIC41 detectors as shown in figure 3.14 (a) and (b), respectively. In addition to the energy loss signal, TOF_{LL} and TOF_{RR} should also be linearly correlated as both represent TOF from SC21 to SC41. The figure 3.14 (c) shows TOF_{LL} vs TOF_{RR} with all of the previous selection conditions applied. The particles seen outside our selection cut (black contour) might originate from artifacts of signal

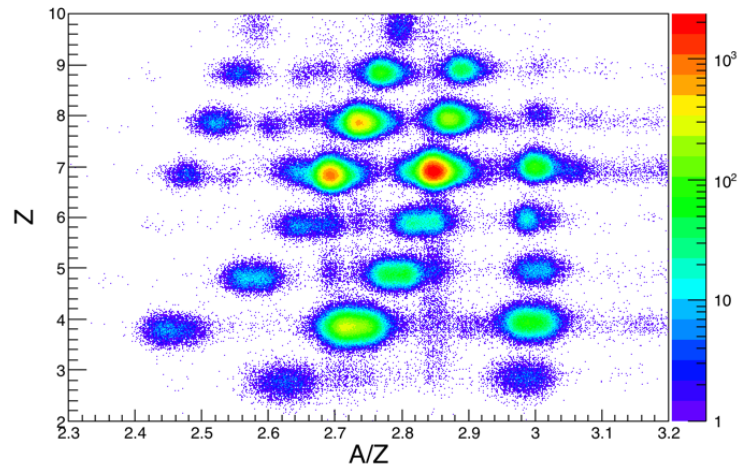


Figure 3.12: The identification plot for the ^{23}O secondary beam after the veto rejection.

processing of the scintillators. The PID plot after all of these rejection conditions is shown in figure 3.15.

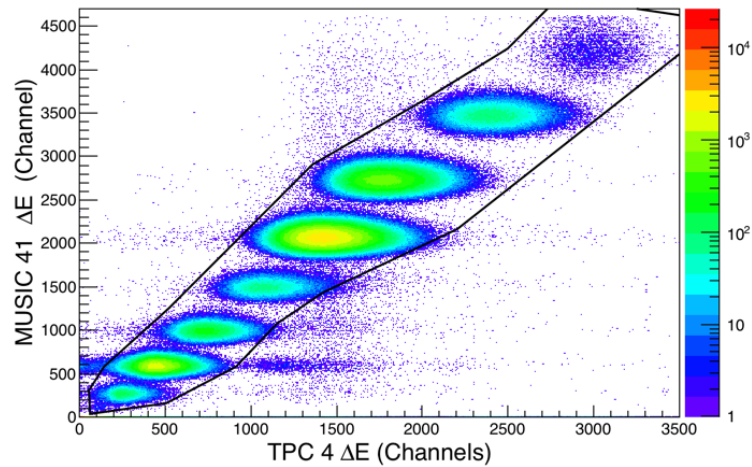


Figure 3.13: The correlation of (a) TPC4 energy signal vs MUSIC41 energy signal after the veto rejection. The events inside of the black contour represents the selection of good events.

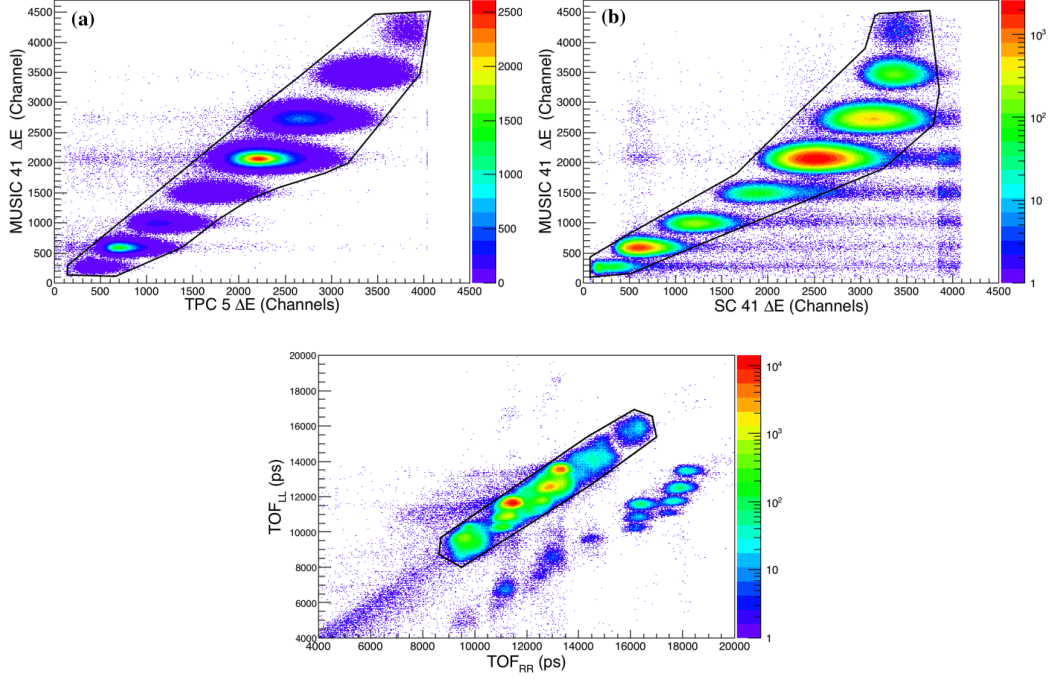


Figure 3.14: The correlation of (a) MUSIC41 energy signal vs. TPC5 energy signal (b) MUSIC 41 energy signal vs. SC41 energy signal (c) TOF_{LL} vs. TOF_{RR} . The events inside black contour represents the selection of good events. The spectra show events after veto rejection.

3.3 Incident beam selection

As discussed in the previous chapter, the σ_{cc} is given by

$$\sigma_{cc} = \frac{1}{t} \ln \frac{R_{out}}{R_{in}} \quad (3.17)$$

where $R_{in} = N_{samez}/N_0$ is the transmission ratio with the target and R_{out} denotes the transmission ratio without the target. The black contour region in figure 3.15 shows the ^{23}O selection before the target for determining the incident beam counts N_0 . This selection should be such that the contamination from neighbouring Z isotopes should be less than 10^{-4} . Figure 3.16 shows the projection of the y-axis of the PID plot, i.e. the Z spectrum of the incident beam. The blue histogram is obtained with the ^{23}O selection condition and the red histogram is the total Z spectrum normalized to the ^{23}O counts. The estimated contamination from $Z = 7$ is 6×10^{-5} and that from

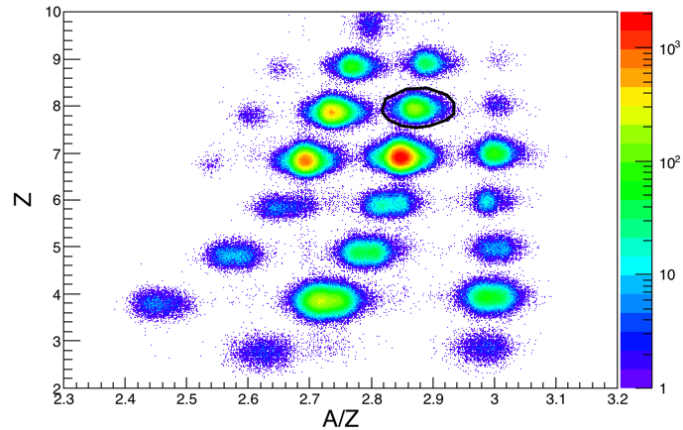


Figure 3.15: The identification plot for the ^{23}O before the reaction target. The black contour represents the ^{23}O incident beam selection.

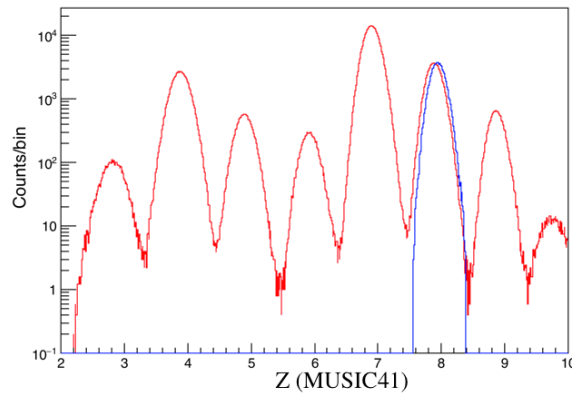


Figure 3.16: The MUSIC41 Z spectrum where the blue histogram represents the ^{23}O selection and the red histogram is the total Z spectrum normalized for ^{23}O .

$Z = 9$ is 2×10^{-5} for this secondary beam. The procedure of background reduction and the selection of the incident beam events as described above was followed for each FRS setting for the different oxygen isotopes.

3.4 Z identification after the target

To determine σ_{cc} we need to count the number of particles that have unchanged charge after the reaction (N_{sameZ}). The energy loss spectrum of MUSIC42 (MUSIC after the target) with the incident beam selected is shown in figure 3.17 using the example of the ^{23}O beam. The red histogram represents the Z spectrum with the reaction target

whereas the blue histogram represents the Z spectrum without the reaction target. In these spectra the production of $Z = 9$ events after the target originate from the charge exchange or proton transfer reactions where one proton is added to the incident nucleus, ^{23}O in this case. These reaction processes do not involve the reactions with

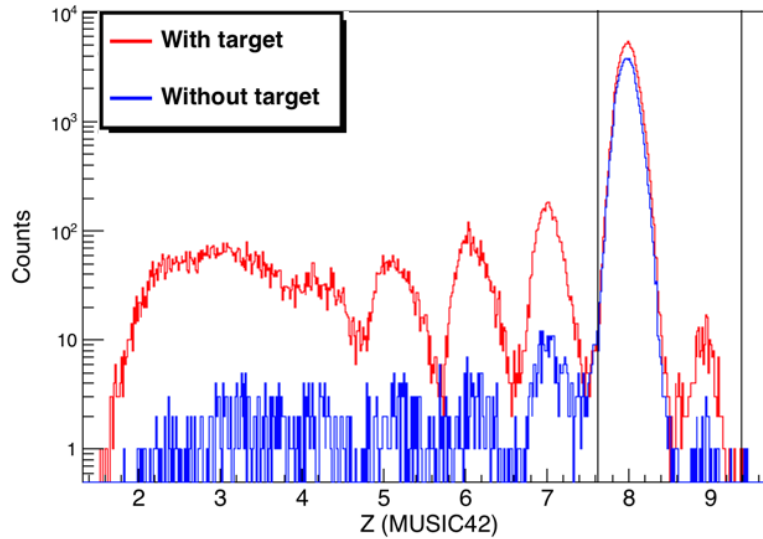


Figure 3.17: The MUSIC42 Z spectrum with the target (red) and without the target (blue) to identify the particles with unchanged Z after the reaction.

the protons in the incident oxygen isotope. Therefore, such reaction events should be subtracted in order to measure the charge-changing cross sections for determining the proton radii and hence we took the total number of counts under $Z = 8$ and $Z = 9$ peaks in our N_{sameZ} selection. As $^{16-18}\text{O}$ isotopes are not in the vicinity of any proton unbound isotopes (the one-proton separation energy of ^{15}O is 7.3 MeV and for ^{17}O is 13.8 MeV) therefore, the effect of proton evaporation from neutron removal cross sections to states above the proton threshold is negligibly small. This effect is negligibly small in $^{19-24}\text{O}$ isotopes because the proton separation energies rapidly increase as move to the neutron-rich nuclei. At beam energies of $\sim 900A$ MeV, nuclear inelastic excitation cross section to states above the proton emission threshold is also negligibly small for the isotopes of interest. The N_{sameZ} selection is marked by black vertical lines in figure 3.17 which covers $\pm 3.5\sigma$ regions of both the $Z = 8$ and $Z = 9$ peaks.

3.5 The target position dependence of transmission ratios

To eliminate losses of N_{sameZ} events after the target due to the large angle scattering of particles out of the detector acceptance, we need to restrict the phase space of the incident beam events at the target. The TPC detectors at F4 were used for beam tracking to determine the beam angle and horizontal (x) and vertical (y) coordinates of the beam event-by-event at the target location. The x position at the target for the

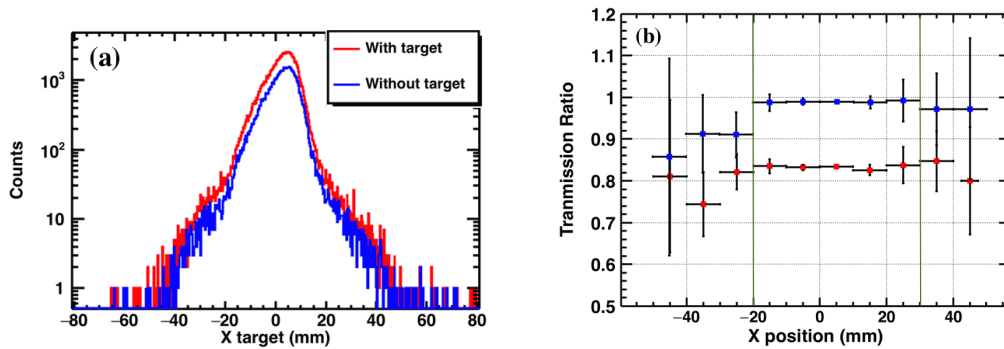


Figure 3.18: (a) The beam x position at the target (X_{target}) (b) Transmission ratio for different X_{target} positions where green vertical lines represent the selection region of constant R .

^{23}O beam is shown in figure 3.18 (a) where the red histogram represents the data taken during the measurement with the reaction target and the blue histogram represents the data taken during the measurement without the reaction target. Figure 3.18 (b)

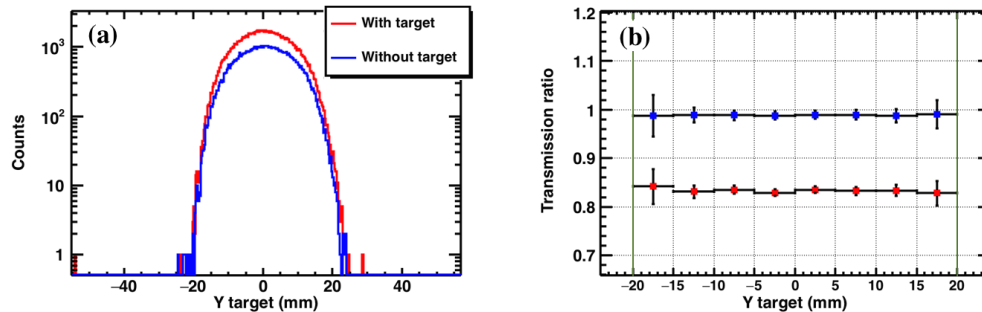


Figure 3.19: (a) The beam y position at the target (Y_{target}) (b) Transmission ratio for different Y_{target} positions where green vertical lines represent the selection region of constant R .

shows the transmission ratio (R) determined for different selection regions of the beam

position X_{target} at 10 mm intervals. The horizontal bars represent the size of the bin and the vertical bars represent the statistical uncertainty in R . As we can see that R_{out} (blue points) is constant from $X_{target} = -20$ mm to $X_{target} = 30$ mm and the R_{in} (red points) is nearly constant from $X_{target} = -30$ to $X_{target} = 40$ mm. We select the region in which both R_{in} and R_{out} are nearly constant (i.e. from $X_{target} = -20$ to 30 mm in this case), to determine the σ_{cc} . Similarly, the y position, the

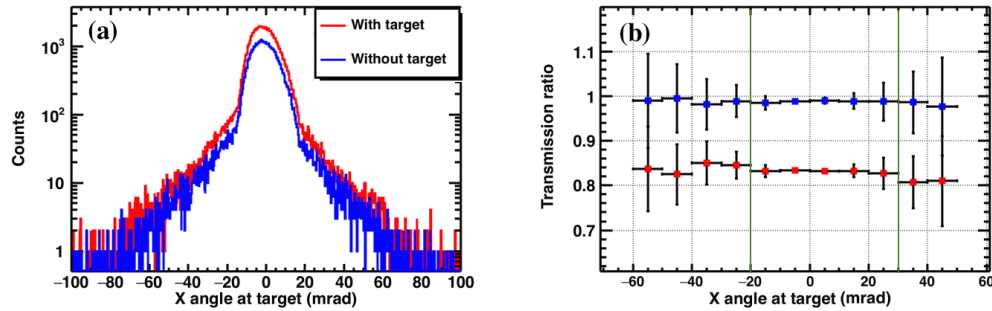


Figure 3.20: (a) The x angle of the beam at the target in mrad (b) Transmission ratio for different x angles where green vertical lines represent the selection region of constant R .

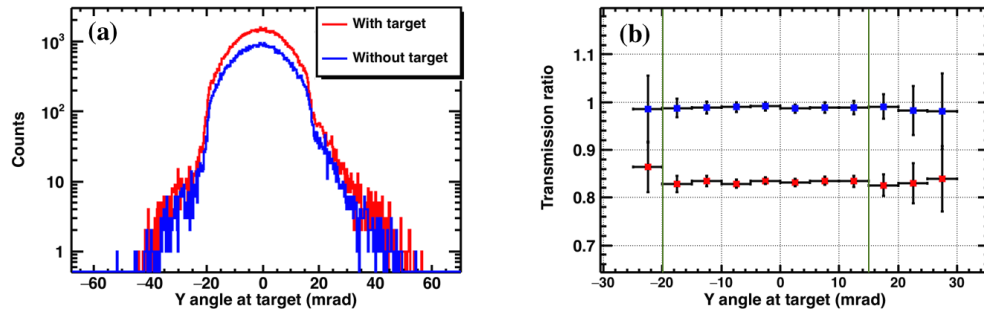


Figure 3.21: (a) The y angle of the beam at the target in mrad (b) Transmission ratio for different y angles where green vertical lines represent the selection region of constant R .

x angle and the y angle of the beam at the target location were determined and the transmission variation for them are shown in figure 3.19, 3.20 and 3.21 with respective selection regions shown by green vertical lines. The phase space restriction conditions were independently determined for each oxygen isotope. After the rejection of events from all of these conditions, the R_{in} and R_{out} were calculated by integrating over

constant transmission region and are discussed in the following chapter along with the σ_{cc} determined from them.

Chapter 4

Discussion

In this chapter, the results and an interpretation is discussed. The chapter begins with a description of the process used for determining the σ_{cc} and their uncertainties. After which is a review of the extraction of the proton radii from the measured σ_{cc} using the Glauber Model analysis. Finally, the trend of the proton radii as a function of the neutron number is analyzed.

4.1 The transmission ratios and σ_{cc}

As stated before, the σ_{cc} is given by

$$\sigma_{cc} = \frac{1}{t} \ln \frac{R_{out}}{R_{in}} \quad (4.1)$$

where $R_{in(out)} = N_{samez}/N_0$ is the transmission ratio with (without) the reaction target and t is the number of target atoms per cm^2 given by

$$t = d \times \left(\frac{N_a}{M_C} \right) \quad (4.2)$$

where $N_a = 6.022 \times 10^{23}$ is Avogadro's number, $M_C = 12.0107u$ is molar mass of carbon, and $d = 4.010 \text{ g/cm}^2$ is the thickness of the carbon reaction target used during the experiment. The R_{in} and R_{out} for $^{16,18-24}\text{O}$ determined from the selection criteria of N_{in} and N_{sameZ} discussed in the previous chapter are shown in the figure 4.1 (a) and (b). There was no data taken for ^{17}O . In figure 4.1 (a) and (b) there are two R_{in} and R_{out} values shown for ^{22}O . The first point represents R_{in} and R_{out} of ^{22}O determined from the data where FRS was centered for ^{22}O (^{22}O set 1) and the second point represents R_{in} and R_{out} of ^{22}O determined from the data where FRS was centered for ^{23}O (^{22}O set 2). R_{in} and R_{out} for both sets of ^{22}O are consistent with each other.

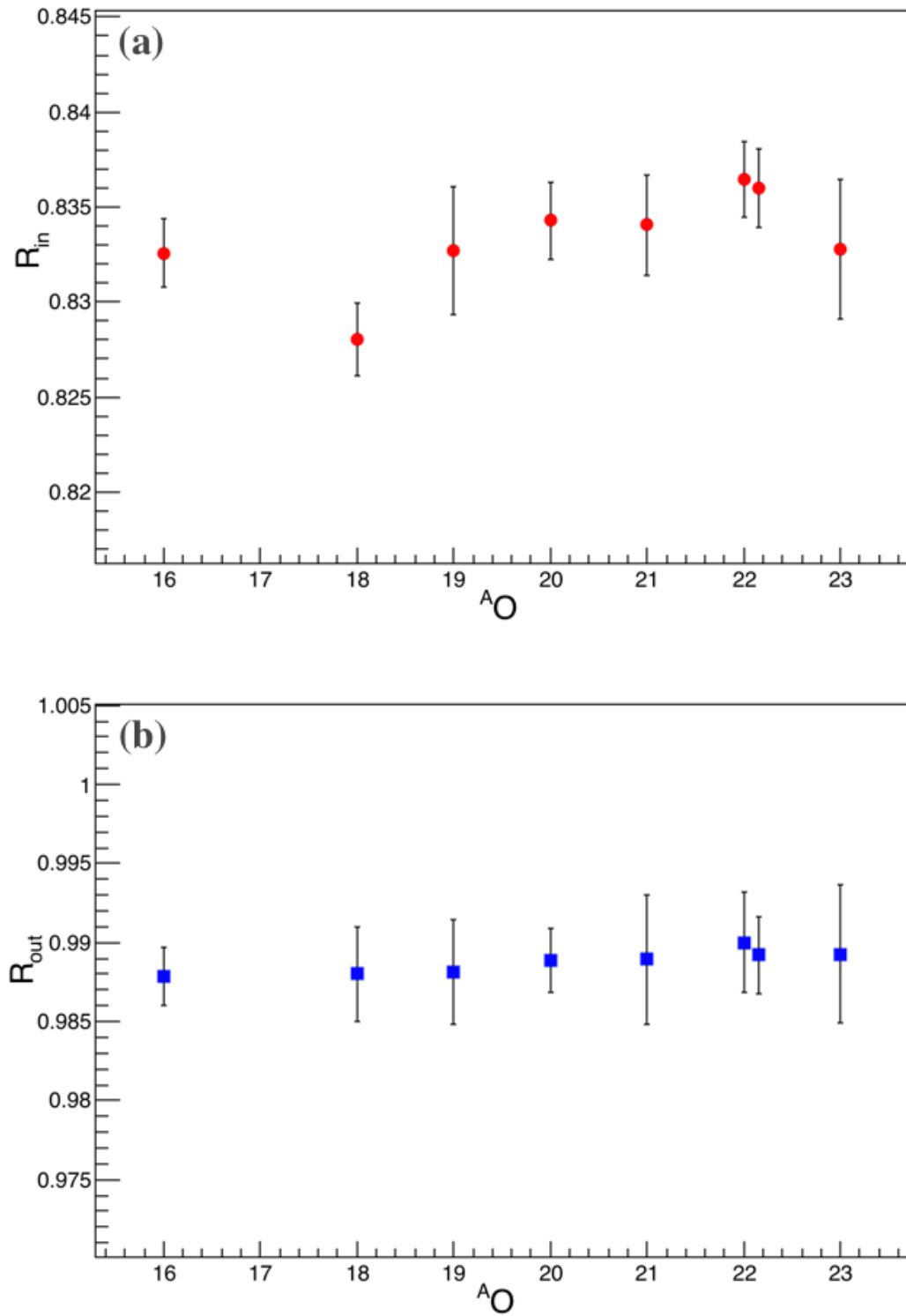


Figure 4.1: The transmission ratios for $^{16,18-24}\text{O}$ (a) with the reaction target (R_{in}) (b) without the reaction target (R_{out}).

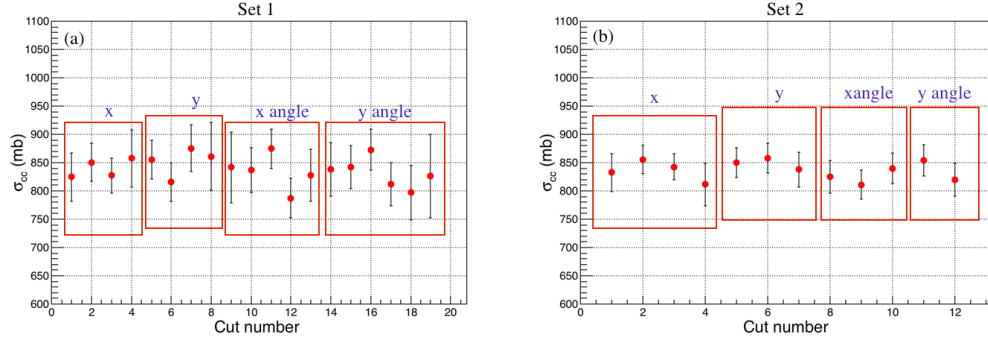


Figure 4.2: The σ_{cc} found by varying the x position, y position, x angle and y angle of the beam at the target location for two sets of data for ^{24}O .

R_{in} and R_{out} of ^{24}O are not shown in the figure 4.1 (a) and (b) and are discussed here. There were two sets of data taken for ^{24}O , one before empty target run for ^{24}O and one after it. The analysis of each set of data was done separately. The central value of σ_{cc} for both sets showed some fluctuation with the changes in the horizontal (x) position, vertical (y) position, the x angle and y angle of the beam at the target location as shown in figure 4.2. The events at the edge of the target have been rejected.

Isotope	σ_{cc} (mb)	$\Delta\sigma_{cc}^{stat}$ (mb)
^{16}O	850	3.8
^{18}O	879	4.4
^{19}O	852	7.1
^{20}O	846	4.5
^{21}O	848	5.8
^{22}O set 1	839	4.3
^{22}O set 2	837	4.4
^{22}O wt.av	838	3.3
^{23}O	857	7.8
^{24}O set 1	843	13.8
^{24}O set 2	835	18.9
^{24}O wt.av	840	11.1

Table 4.1: The measured σ_{cc} of $^{16,18-24}\text{O}$ with statistical uncertainties.

The error bars represent the statistical uncertainties and are discussed in detail in section 4.2. Each red box in figure 4.2 represents the σ_{cc} found by changing each variable (x position, y position, x angle and y angle) of the beam one at a time. The integrated cross sections for all points in each red box were found. The average of all

four integrated σ_{cc} and the standard deviation for both sets are given in the table 4.3 along with the measured σ_{cc} for $^{16,18-24}\text{O}$. The measured σ_{cc} for $^{16,18-24}\text{O}$ as a function of mass number of the oxygen isotopes are shown in figure 4.3. The blue circles represent the weighted average σ_{cc} for ^{22}O and ^{24}O from two independent data sets that are shown by black circles.

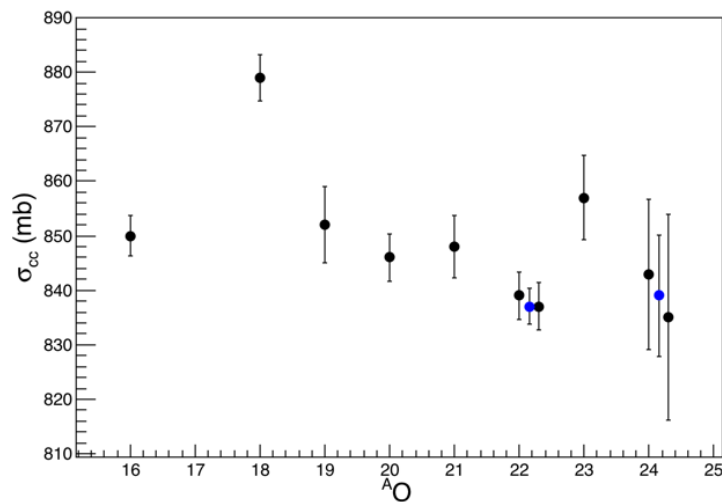


Figure 4.3: The measured σ_{cc} of $^{16-18,24}\text{O}$ with statistical uncertainties.

4.2 Uncertainty of the measured cross section

The uncertainty in the measured σ_{cc} arises from the statistics (number of same Z events after the target), the target thickness measurement and the selection of the same- Z events after the target. The statistical and systematic uncertainties in the measured σ_{cc} are discussed in following sections. There is no statistical uncertainty in the number of incident particles in this measurement as the incident beam counts are from the desired event by event selection of the secondary beam. There is no uncertainty related to dead time losses because the same Data Acquisition system (DAQ) was used to count the incident and the same Z events. The rate per second for stable isotopes is 500 counts/sec and much lower for the neutron-rich isotopes of oxygen. The isotope intensities are given in Table. 2.1. Therefore, the probability of having a multi-hit events is negligible. If there is a multi-hit event for the same Z or nearby Z in MUSIC41, then it should have a much higher pulse height than the

real events and is not taken in our incident beam selection. In order to assess and reject multi-hit events where $Z = 8$ only hit MUSIC41 but both the events hit the MUSIC42 after the target, a veto scintillator was used. The veto scintillator rejection was discussed in section 3.3.

4.2.1 Statistical uncertainty

In this experiment, statistics were the main source of error. The statistical uncertainty of the σ_{cc} was found in the following way. The standard deviation of charge-changing cross sections ($\Delta\sigma_{cc}$) is given by

$$\Delta\sigma_{cc} = \sqrt{\left(\frac{\partial\sigma_{cc}}{\partial R_{in}}\right)^2 \Delta R_{in}^2 + \left(\frac{\partial\sigma_{cc}}{\partial R_{out}}\right)^2 \Delta R_{out}^2 + \left(\frac{\partial\sigma_{cc}}{\partial t}\right)^2 \Delta t^2} \quad (4.3)$$

where ΔR_{in} , ΔR_{out} and Δt are standard deviations of R_{in} , R_{out} and target thickness respectively, and

$$\frac{\partial\sigma_{cc}}{\partial R_{in}} = \frac{1}{t} \frac{1}{R_{in}}, \quad \frac{\partial\sigma_{cc}}{\partial R_{out}} = \frac{1}{t} \frac{1}{R_{out}}, \quad \frac{\partial\sigma_{cc}}{\partial t} = \frac{1}{t^2} \ln \frac{R_{out}}{R_{in}} \quad (4.4)$$

Substituting the derivatives given above (eq. 4.4), in eq. 4.3, the $\Delta\sigma_{cc}$ can be expressed as

$$\frac{\Delta\sigma_{cc}}{\sigma_{cc}} = \sqrt{\left[\left(\frac{\Delta R_{in}}{R_{in}}\right)^2 + \left(\frac{\Delta R_{out}}{R_{out}}\right)^2\right] \left(\ln \frac{R_{out}}{R_{in}}\right)^{-2} + \left(\frac{\Delta t}{t}\right)^2} \quad (4.5)$$

There is no uncertainty in the number of incident particles, ΔR_{in} (ΔR_{out}) were obtained using the variance of a binomial distribution and are given below:

$$\left(\frac{\Delta R_{in}}{R_{in}}\right)^2 = \frac{N_0^{in} R_{in} (1 - R_{in})}{(N_0^{in} R_{in})^2} = \frac{1 - R_{in}}{N_0^{in} R_{in}} \quad (4.6)$$

$$\left(\frac{\Delta R_{out}}{R_{out}}\right)^2 = \frac{1 - R_{out}}{N_0^{out} R_{out}} \quad (4.7)$$

where $N_0^{in(out)}$ denotes incident beam counts with(without) the target. The uncertainty of the cross section, $\Delta\sigma_{cc}$, can therefore be written as

$$\left(\frac{\Delta\sigma_{cc}}{\sigma_{cc}}\right)^2 = \left[\frac{1 - R_{in}}{N_0^{in} R_{in}} + \frac{1 - R_{out}}{N_0^{out} R_{out}}\right] \left(\frac{1}{\sigma_{cc} t}\right)^2 + \left(\frac{\Delta t}{t}\right)^2 \quad (4.8)$$

The thickness (t) of the secondary C target was measured to be 21.771 mm with a standard deviation $\Delta t = 0.0158$ mm. It was measured sampling ≈ 3000 points in the central region of the target (1mm x 1mm raster). Δt was substituted in the last term in equation 4.8. The estimated uncertainties in σ_{cc} due to the target thickness measurement for all oxygen isotopes are given in table 4.4.

4.2.2 Uncertainty from contaminants in the same Z events after the target

As discussed in the previous chapter, the events with N_{sameZ} (i.e. the events that did not interact with the protons of the projectile) were measured by taking ± 3.5 σ of the $Z = 8$ and $Z = 9$ peaks detected by MUSIC42 (MUSIC after the target at F4). However, this selection may also contain some contamination from the $Z = 7$ events which could contribute to the uncertainty in the cross section. We denote this uncertainty by $\Delta\sigma_{cc}^{cont}$. The $Z = 7$ contamination within the $Z = 8$ selection region was estimated by fitting the tail of the $Z = 7$ peak with an exponential function. The energy loss signal of MUSIC42 detector for ^{23}O secondary beam after reaction with the carbon target, is shown as an example in figure 4.4. The exponential function fit

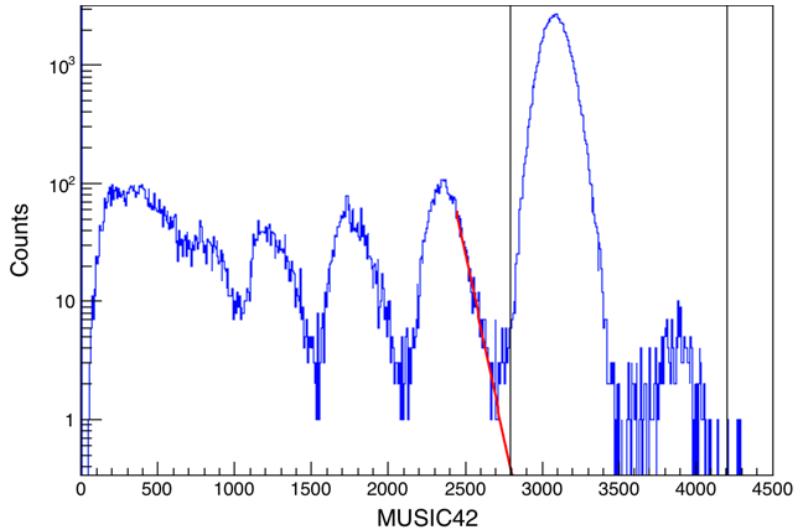


Figure 4.4: The MUSIC42 detector spectrum for the ^{23}O secondary beam. The red curve shows an exponential function fit of the tail of the $Z = 7$ peak.

is shown by the red curve in figure 4.4. The estimated contamination from $Z = 7$

within the N_{sameZ} selection is 5×10^{-5} . The $Z = 7$ contamination within the $Z = 8$ peak of MUSIC42 spectrum without the reaction target was estimated to be 8×10^{-5} . The $\Delta\sigma_{cc}^{cont}$ was estimated to be ± 0.07 mb in the measured σ_{cc} of ^{23}O . The estimated $\Delta\sigma_{cc}^{cont}$ of each isotope is listed in table 4.4.

4.3 Secondary beam energies

The velocity (β) of the particles at F4 was measured by SC41 (the first scintillator detector at F4). β of the ^{23}O incident beam at SC41 is shown as an example in figure 4.5, in which the mean of the peak = 0.857 which corresponds to $E = 874.34$ MeV. The energy loss of the particles in the matter between SC41 and the target was

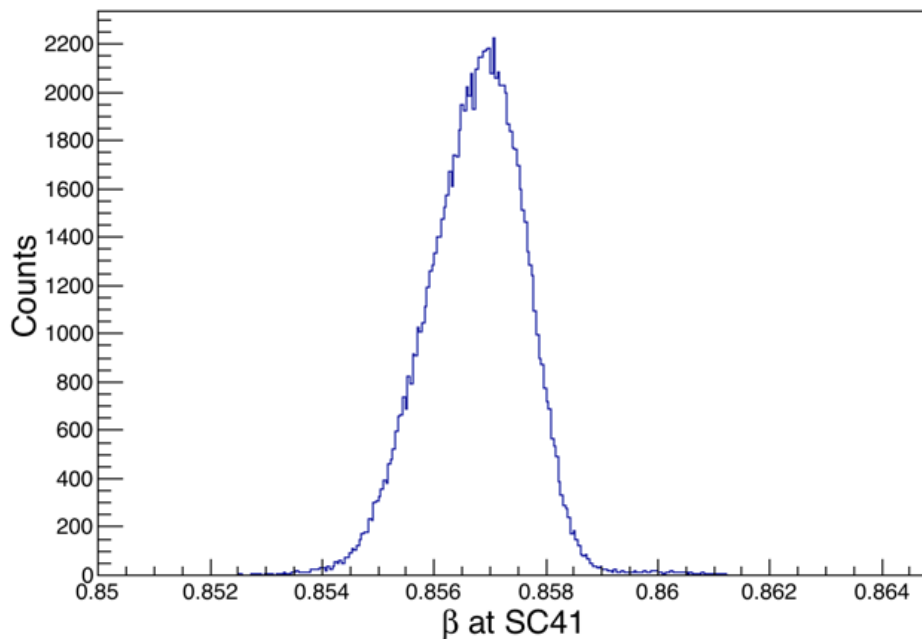


Figure 4.5: The measured velocity (β) of the particles at SC41 for the ^{23}O secondary beam.

calculated using the LISE code [89]. The total energy loss was subtracted from the beam energy measured at SC41 to obtain the beam energy at the entrance of the target and the values are given in table 4.2.

^A O	<i>E/A</i> in MeV				
	At SC41	E_{loss}^{MUSIC}	E_{loss}^{TPCs}	E_{loss}^{air}	In front of target
¹⁶ O	863	2.18	3.13	0.36	857
¹⁸ O	877	1.93	2.77	0.32	872
¹⁹ O	961	1.79	2.57	0.30	956
²⁰ O	884	1.73	2.49	0.29	880
²¹ O	938	1.63	2.34	0.27	934
²² O set 1	869	1.58	2.27	0.26	865
²² O set 2	941	1.55	2.23	0.26	937
²³ O	875	1.51	2.17	0.25	871
²⁴ O set 1	870	1.45	2.08	0.24	866
²⁴ O set 2	870	1.45	2.08	0.24	866

Table 4.2: The energy losses in materials placed between SC41 and the carbon reaction target at F4.

4.4 MUSIC42 detection efficiency correction

The efficiency of the MUSIC detector after the reaction target was determined using the TPC detector and the scintillator detector placed after it. The efficiency (ϵ) of a detector is given

$$\epsilon = \frac{N_i}{N_T} \quad (4.9)$$

where N_i is number of particles detected by a detector and N_T is the total number of particles incident on a detector. If we denote the efficiencies of TPC6, SC42 and MUSIC42 for oxygen isotope detection by ϵ_1 , ϵ_2 and ϵ_3 , respectively, then eq. 4.9 for each of these detector becomes

$$\epsilon_1 = \frac{N_1}{N_T}, \quad \epsilon_2 = \frac{N_2}{N_T}, \quad \epsilon_3 = \frac{N_3}{N_T} \quad (4.10)$$

where N_1 , N_2 and N_3 are number of oxygen nuclei detected in the corresponding detector. The efficiency of MUSIC42 detector can be found using the correlation of number of oxygen nuclei detected in the three detectors. Figure 4.6 (a) shows the SC42 energy loss signal vs TPC energy loss signal for the ²³O incident beam. The red geometric contour region shows the selection of oxygen nuclei where both TPC6 and SC42 are hit. The energy loss signal of the MUSIC detector with the selection condition from the left figure applied to it is shown in figure 4.6 (b). The number

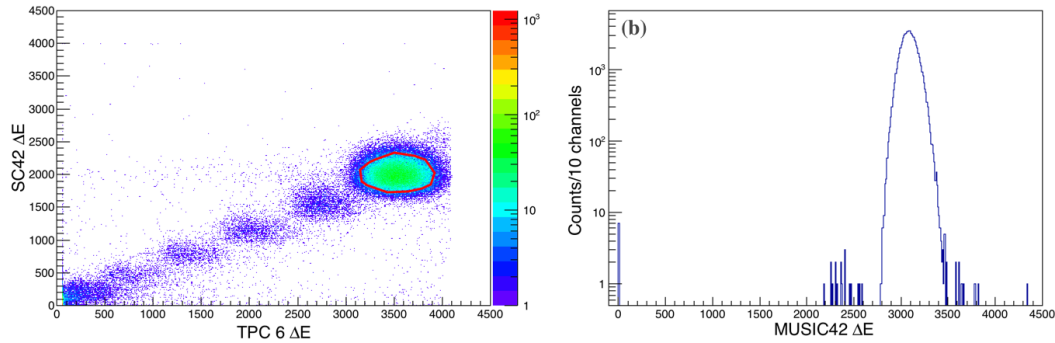


Figure 4.6: (a) The TPC detector energy loss vs. SC42 energy loss. The black geometric cut represents the selection of oxygen nuclei. (b) The energy loss spectrum of MUSIC after the detector with a selection cut from the left figure.

of counts in the MUSIC detector under oxygen peak represent the number of nuclei which hit all three detectors. By dividing the number of counts under the oxygen peak in figure 4.6 (b) by the number of nuclei in the enclosed selection in figure 4.6 (a) ϵ_3 was determined for both with and without the reaction target. The efficiency of the MUSIC detector was found to be 99.99% for ^{23}O for “with target” case. The σ_{cc} of $^{16-18,24}\text{O}$ were corrected for the detection efficiency of MUSIC42 and the efficiency correction values are listed in table 4.3. The efficiency corrected σ_{cc} are given in table 4.4.

Isotope	ϵ_{corr} (mb)
^{16}O	2.14
^{18}O	-0.05
^{19}O	-0.05
^{20}O	-0.23
^{21}O	0.24
^{22}O set 1	0.39
^{22}O set 2	0.86
^{23}O	-0.06
^{24}O set1	0.63
^{24}O set2	1.20

Table 4.3: The MUSIC42 detection efficiency corrections to σ_{cc} for $^{16-18,24}\text{O}$.

4.5 Table of charge-changing cross sections

The efficiency corrected σ_{cc} values with the uncertainties and the secondary beam energies in front of the target for $^{16,18-24}\text{O}$ are listed in table 4.4. The σ_{cc} of ^{22}O and ^{24}O were found by taking a weighted average of σ_{cc} from the two sets of data.

Isotope	E/A	σ_{cc}	statistical	<i>Systematic</i>		Total
	<i>MeV</i>			<i>mb</i>	$\Delta\sigma_{cc}^{stat}$	
			<i>mb</i>			
^{16}O	857	848	3.8	0.082	0.62	3.9
^{18}O	872	879	4.4	0.46	0.64	4.5
^{19}O	956	852	7.1	0.59	0.62	7.2
^{20}O	880	846	4.5	0.06	0.61	4.5
^{21}O	934	847	5.8	0.64	0.62	5.9
^{22}O set1	865	838	5.0	0.14	0.61	5.0
^{22}O set2	937	837	4.4	0.05	0.61	4.4
^{22}O wt.av		837				3.3
^{23}O	871	857	7.8	0.07	0.62	7.8
^{24}O set1	866	842	13.8	1.14	0.61	13.9
^{24}O set 2	866	834	18.9	1.11	0.61	18.9
^{24}O wt.av		839				11.2

Table 4.4: The measured σ_{cc} with the uncertainties and secondary beam energies in front of the target.

The σ_{cc} values listed in table 4.4 show a significant variation with increasing neutron number. The σ_{cc} of $^{16-24}\text{O}$ were also measured by Chulkov et al. [77]. The σ_{cc} reported in Ref. [77] have higher uncertainties and are inconsistent with the σ_{cc} derived using R_p from e^- scattering experiments. Therefore the measured σ_{cc} in Ref. [77] are unsuitable for studying nuclear structure evolution. The proton radii were not determined from the measured charge-changing cross section in Ref. [77]. The finite range Glauber Model was used to determine proton radii from charge-changing cross sections. In the following section, the determination of the proton radii from σ_{cc} is discussed.

4.6 Proton radii determination

The evolution of the experimentally determined proton radii with increasing neutron number allows us to test the predictions from newly developed models of nuclear

structure based on the *ab initio* theory. The proton radii are also necessary to determine the nuclear skin thickness. The proton radii were determined using the Glauber model framework, described in section 1.5. The density distribution of target nucleus, ^{12}C , is well known from e^- scattering. Therefore, the only unknown quantity in $P_{cc}(\mathbf{b})$ according to equation 1.12, is the projectile's proton density. When calculating the σ_{cc} , we used the harmonic oscillator density [96] for both the projectile and the target. Figure 4.7 shows σ_{cc} calculated for three different oscillator widths for

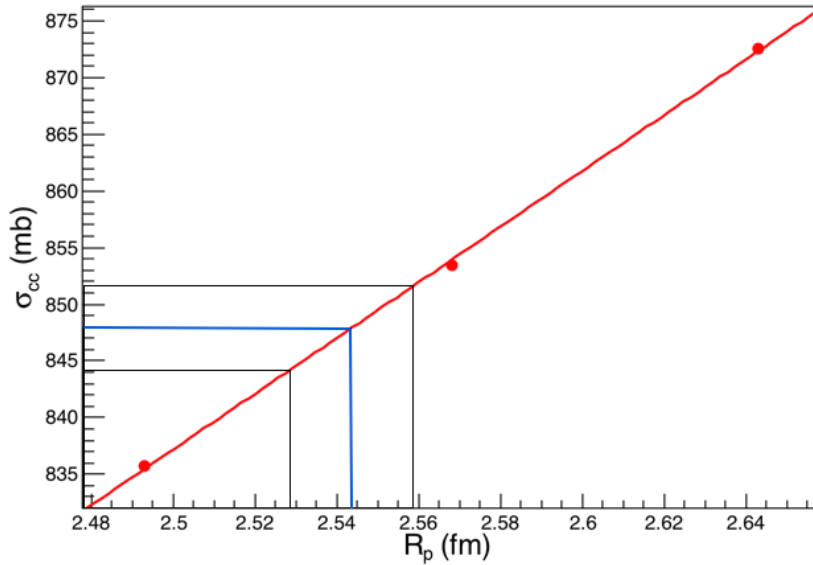


Figure 4.7: The σ_{cc} for ^{16}O calculated using three different harmonic oscillator widths for the density distributions with different R_p . The blue horizontal line represents the central value of the measured σ_{cc} . The black lines represent the uncertainties. The vertical lines show the rms proton radii corresponding to the measured σ_{cc}

proton density of ^{16}O . These three oscillator widths correspond to three different rms proton radii that are shown in figure 4.7. The bright red line is a linear fit of these three points. The measured σ_{cc} for $^{16}\text{O} = 848 \pm 3.9$ mb is shown by the horizontal band in figure 4.7. The vertical band shows proton radii corresponding to the measured σ_{cc} i.e. the measured point proton radii from the measured σ_{cc} (R_p^{cc}). The value of the extracted proton radius for ^{16}O is given in table 4.5. Similarly, the proton radii of $^{18-24}\text{O}$ isotopes were extracted by comparing the measured σ_{cc} to the Glauber Model calculations and are listed in table 4.5. This is the first determination of the proton radii of the neutron-rich oxygen isotopes. The point proton radii of $^{16,18}\text{O}$ are

consistent with the those determined from electron scattering [37]. The R_p^{cc} for ^{10}B , $^{12-14}\text{C}$ [82,84] and ^{14}N [85] determined using the finite-range Glauber Model framework are also consistent with point proton radii determined from the electron scattering experiments. These demonstrate the successful use of the Glauber model to extract radii at 800-900A MeV. The study of σ_{cc} for $^{12}\text{C} + ^{12}\text{C}$ at energies around 900A MeV in Ref. [80] shows that the uncertainty from profile function parameters is less than 1%. In Ref. [56], for a 2% uncertainty in σ_R , the uncertainty in the matter radius due to different densities was estimated to be 5%. The uncertainty due to different densities largely comes from the extended neutron density tail. As the protons are deeply bound, the density distribution of protons do not have extended tail. Hence, the uncertainty in the proton radius due to the different projectile densities with the same radius may be expected to be small in comparison to matter radii. Yamaguchi et al. [83] measured the charge-changing cross sections of $^{16-18}\text{O}$ at 300A MeV and employed the zero range Glauber Model to determine the proton radii. However, they had to introduce a scaling factor to reproduce the proton radii consistent with the e^- scattering experiments.

Isotope	R_p^{cc} (fm)	$R_p^{(e^-)}$ (fm)
^{16}O	2.54(2)	2.55(1)
^{18}O	2.67(2)	2.66(1)
^{19}O	2.55(3)	
^{20}O	2.53(2)	
^{21}O	2.53(2)	
^{22}O	2.50(1)	
^{23}O	2.58(3)	
^{24}O	2.51(4)	

Table 4.5: The measured R_p^{cc} of $^{16-18,24}\text{O}$ extracted from the measured σ_{cc} . The $R_p^{(e^-)}$ for $^{16-18}\text{O}$ are from Ref. [37].

4.7 Discussion of results

The point proton radii determined from the measured σ_{cc} (R_p^{cc}) are shown in figure 4.8 and are represented by the black filled circles. The point proton radii from e^- scattering [37] are also shown in figure 4.8 (red filled squares). The R_p^{cc} increases from

^{16}O to ^{18}O in agreement with the e^- scattering results. The R_p^{cc} shows a decrease for ^{19}O and following that the R_p^{cc} of $^{19-21}\text{O}$ do not show any variation with increasing neutron number within the uncertainties.

However, the R_p^{cc} of ^{22}O decreases followed by an increase in R_p^{cc} of ^{23}O . The decrease in R_p^{cc} at $N = 14$ is an indication of the presence of a shell gap at this neutron number. The shell gaps can be visible as local minima in the radii along an isotopic chain [11]. The high-lying first excited state in ^{22}O at 3.17 MeV [43, 44] also supports the shell closure at $N = 14$. This finding is also supported by a small deformation factor (β) = 0.26(4) for ^{22}O which was derived from the phenomenological analysis of proton inelastic scattering [46]. The new magic numbers in neutron-rich nuclei can be considered to originate due to the strong monopole interaction of the nuclear force [41]. The monopole interaction between the protons and neutrons ($T = 0$) orbit pairs with $j = l + 1/2$ and $j = l - 1/2$ is stronger than the $j = l + 1/2$ and $j = l + 1/2$ (or $j = l - 1/2$ and $j = l - 1/2$) pairs. Therefore, the strong attractive monopole proton-neutron interaction between the $p(1p_{1/2})$ and $n(1d_{5/2})$ causes the lowering of the $n(1d_{5/2})$ orbital, creating the energy gap. This shell gap between $1d_{5/2}$ and $2s_{1/2}$ in ^{22}O was found to be 2.8 (1) MeV [45]. This attraction also causes the lowering of $p(1p_{1/2})$ and thus the observed decrease in R_p^{cc} of ^{22}O . In ^{23}O , the neutron is expected to be in the $2s_{1/2}$ level in its ground state. The $2s_{1/2}$ spectroscopic factor was found to be 0.97(19) in Ref. [48] from the one-neutron knockout of ^{23}O and 0.78(13) from the Coulomb dissociation [49]. Both of the values agree within uncertainties and support the $2s_{1/2}$ single particle structure of ^{23}O . Therefore, the observed increase in R_p^{cc} of ^{23}O is a result of its extended neutron density for the valence neutron in the $2s_{1/2}$ orbital with a closed-shell core of ^{22}O . The center-of-mass ($c.m$) of ^{23}O is therefore different from that of the core (^{22}O) causing the $c.m$ motion smearing of the core density and hence an increased proton radius.

The measured R_p^{cc} of ^{24}O show a decrease, affirming the shell closure at $N = 16$. The study of the of neutron separation energies with increasing neutron number [9], systematic study of the beta decay Q values, and the energies of the first excited state for even-even neutron-rich nuclei, showed sharp discontinuities and confirmed the shell closure at $N = 16$ [10]. The spectroscopic factor (S) has been measured through the neutron removal reaction of ^{24}O [12]. A nearly pure $2s_{1/2}$ neutron spectroscopic factor

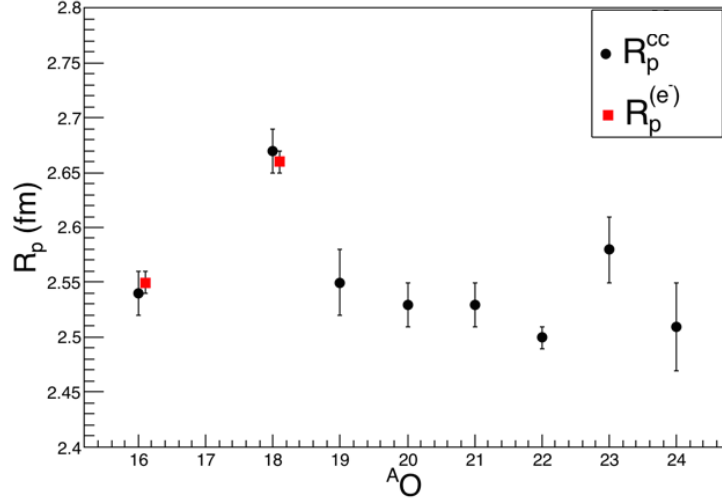


Figure 4.8: The measured point proton radii (R_p) where the black circles represent R_p^{cc} and the red squares represent $R_p^{(e^-)}$.

of 1.74 ± 0.19 was determined which established the spherical shell closure at $N = 16$ in ^{24}O . A quadrupole deformation parameter β_2 of the first 2^+ excited state of ^{24}O was determined by proton inelastic scattering to be 0.15 ± 0.04 [13]. The small β_2 is in agreement with the spherical nature of the shell closure at $N = 16$. The decrease in R_p^{cc} of ^{24}O within the uncertainties is a signature of the reduction in deformation due to the large shell gap (~ 4.8 MeV from Ref. [40]) between the $1d_{5/2}$ and $2s_{1/2}$ neutron orbitals. The emergence of this new magic numbers is thought to be related to the missing $T = 0$ monopole interaction between $n(1d_{3/2})$ neutrons and $p(1d_{5/2})$ [42]. The $p(1d_{5/2})$ orbit is vacant in oxygen isotopes, which causes the $1d_{3/2}$ orbital to move up, thus creating a shell gap at $N = 16$. The shell gap at $N = 16$ disappears for stable nuclei because the $p(1d_{5/2})$ shell is almost filled.

4.7.1 Comparison with theory

The three-nucleon interaction is required to reproduce the magic number at ^{22}O ($N = 14$) and the position of the oxygen drip-line at ^{24}O ($N = 16$) [24, 27, 29]. The *ab initio* models have been successful in reproducing the binding energies of neutron-rich oxygen isotopes [27–31, 34]. However, these theories have not been tested for the proton radii as there were no data. A simultaneous reproduction of binding energies

and radii in stable and neutron-rich nuclei is important for the complete understanding of nuclear forces and therefore also for nuclear structure. In figure 4.9 and 4.10 the proton radii extracted from σ_{cc} are compared to proton radii using different *ab initio* approaches. Figure 4.9 shows the comparison of R_p calculated using the $NNLO_{sat}$

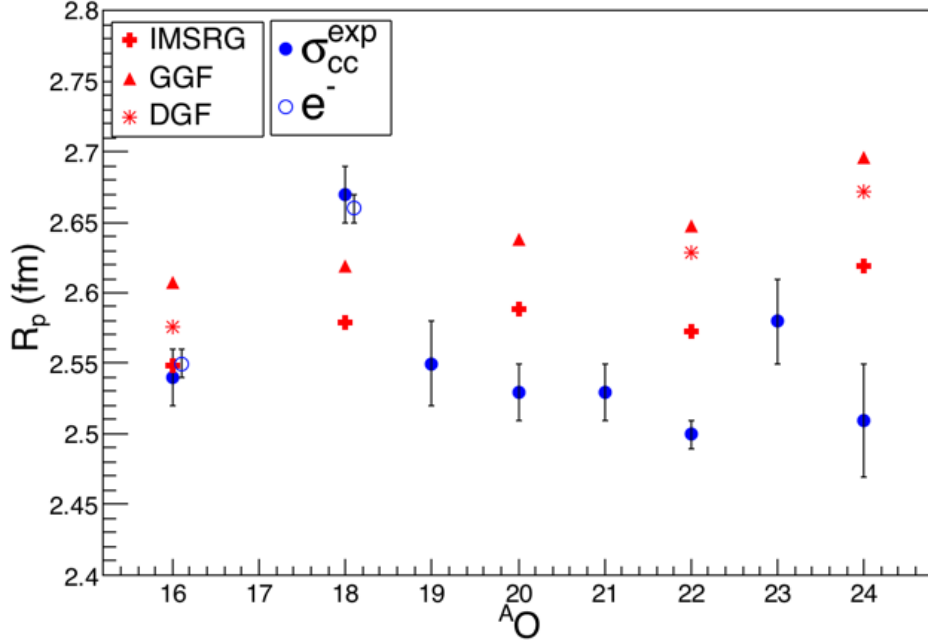


Figure 4.9: R_p from Ref. [34] calculated using $NNLO_{sat}$ interaction with three different many-body approaches compared to the measured R_p^{cc} (blue circles).

interaction with three different many-body approaches from Ref. [34] to the measured R_p^{cc} . The blue filled circles are experimental R_p^{cc} whereas the blue open circles represent the experimental R_p derived from e^- scattering [37]. The measured charge radius of ^{16}O is included in the set of LECs for the $NNLO_{sat}$ interaction. The calculated R_p with all three many-body approaches: Dyson SCGF (DGF, represented by stars), in-medium similarity renormalization group (IMSRG, represented by pluses) and Gorkov SCGF (GGF, represented by triangles) show some difference in the calculated radii but the common feature is that these do not show any significant variation of R_p between ^{16}O and ^{18}O which is contrary to the experimental observations. In 1979 Brown et al. [97] calculated nuclear charge and matter distributions using the Hartree-Fock method by taking into account shell model configuration mixing. The $6p - 4h$ excitations were included in the psd wave functions for ^{18}O to reproduce

the difference in rms radii between ^{16}O and ^{18}O , in agreement with the experiments. Therefore, we believe in order to explain the increase in charge radii of ^{18}O from first principles, it is necessary to take into account the configuration mixing in the *ab initio* calculations. Our collaboration is undertaking new coupled-cluster calculations with the $NNLO_{sat}$ interaction to have a better understanding of the measured R_p^{cc} .

The observed decrease in R_p^{cc} for ^{22}O is also predicted by the IMSRG where GGF on the other hand shows a very small increase. The R_p of odd mass nuclei were not calculated which makes it difficult to observe the effect of an increase in the radius of ^{23}O due to transition from the closed $1d_{5/2}$ shell to the odd neutron in $2s_{1/2}$ as seen in the measured R_p^{cc} . Overall, the predicted R_p of $^{19-24}\text{O}$ are higher than measured R_p^{cc} whereas the predicted R_p for ^{18}O is lower than the measured R_p^{cc} and $R_p^{(e^-)}$.

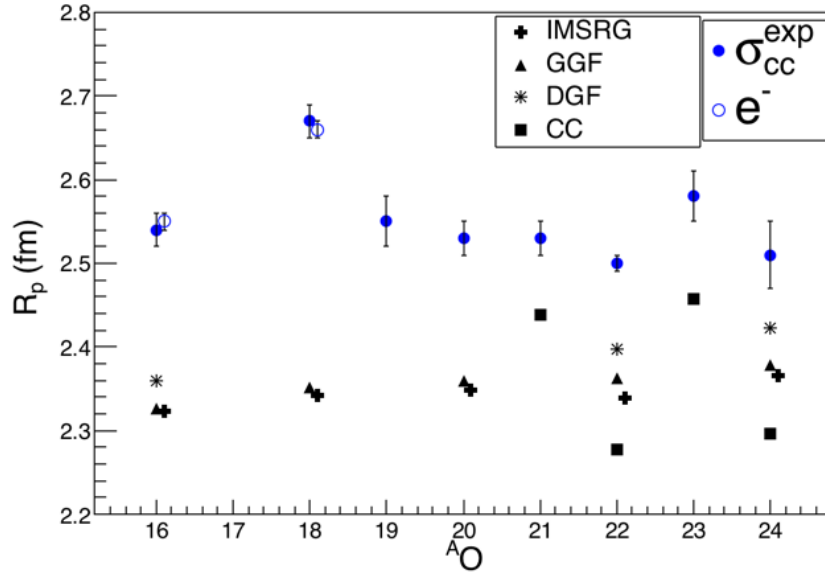


Figure 4.10: The comparison of the measured R_p^{cc} (blue circles) to R_p from Ref. [34] calculated using the EM interaction with three different many-body approaches and R_p from Ref. [27] computed using the coupled-cluster calculation.

Figure 4.10 shows R_p^{cc} compared to the R_p calculated using the same three many-body approaches with EM interaction from Ref. [34] and coupled-cluster computations from Ref. [27]. The stars represent Dyson SCGF (DGF), the plusses represent the in-medium similarity renormalization group (IMSRG), triangles represent the Gorkov

SCGF (GGF) calculations from Ref. [34] whereas the squares represent the coupled-cluster calculation (CC) from Ref. [27]. All four many-body approaches underestimate the measured R_p^{cc} (blue points). However, the trend of the proton radii calculated using the coupled-cluster computations clearly show the dips at $N = 14$ and $N = 16$ consistent with the evolutionary trend of the experimental proton radii, hence supporting the signature of the shell closures at these neutron numbers. The new data presented in this thesis therefore provide grounds for the further development of the *ab initio* theories and the interactions employed in the different calculations. Our collaboration is undertaking new coupled-cluster calculations with the $NNLO_{sat}$ interaction to have a better understanding of the measured R_p^{cc} .

4.8 Neutron skin thickness determination

The matter radii of oxygen isotopes are known from the interaction cross section measurement [55,56]. The neutron radii were determined by substituting the measured matter radii and the measured proton radii reported in this work in equation 1.6. The

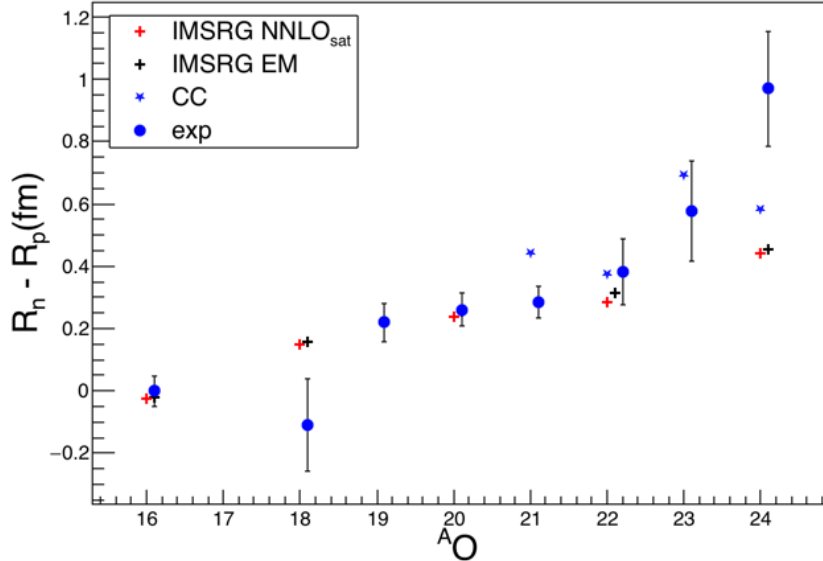


Figure 4.11: The experimental neutron skin (blue circles) determined from measured R_p^{cc} and the measured R_m from Ref. [55, 56]. ΔR calculated using IMSRG approach with EM interaction (black symbols) and $NNLO_{sat}$ interaction (red symbols) from Ref. [34] is shown by pluses and ΔR calculated using radii from coupled-cluster calculation is shown by blue stars.

derived neutron skin thickness for $^{16,18-24}\text{O}$ is shown in figure 4.11. It was found that ΔR rapidly increases from $^{22-24}\text{O}$, approaching the neutron drip-line, and establishing a thick neutron surface for the neutron-rich oxygen isotopes. The comparison of the measured ΔR values to the calculated values is also shown in figure 1.9. The plusses represent ΔR found from calculated radii using the IMSRG approach with EM interaction (black symbols) and $NNLO_{sat}$ interaction (red symbols) from Ref. [34]. The blue stars represent the coupled-cluster calculations from Ref. [27]. These *ab initio* theories underestimate ΔR for ^{24}O . The IMSRG approach overestimates ΔR for ^{18}O and coupled-cluster approach overestimates ΔR for ^{21}O . Further theoretical calculations are ongoing in our collaboration to determine the matter radii from the measured interaction cross-sections [55, 56] using the R_p^{cc} and the Glauber Model framework discussed in Ref [80]. These new matter radii will more accurately determine the neutron skin thickness in the oxygen isotopes.

4.9 Summary

The intent of the work described in this dissertation was to determine the proton radii of neutron-rich oxygen isotopes. These are particularly interesting nuclei, with a new magic number ($N = 16$) [9, 10, 12, 13] at the neutron drip-line [15–19]. We have determined the proton radii using the measured charge-changing cross sections (σ_{cc}), which is the cross-section for the reactions in which the atomic number of the projectile nucleus is decreased. The σ_{cc} measurement can therefore be used to determine R_p of neutron-rich isotopes with short half-lives.

The experiment was performed at GSI, Darmstadt, Germany with exotic neutron-rich projectiles of $^{16,18-24}\text{O}$. These projectiles were produced by fragmentation of a ^{40}Ar primary beam accelerated to 1A GeV. The charge-changing cross sections were measured using a 4.010 g/cm^2 thick carbon target placed at the final focus of FRS. The measured σ_{cc} show a significant variation with increasing neutron number and have much smaller uncertainties compared to the σ_{cc} values reported in Ref. [77].

The R_p for $^{16,18-24}\text{O}$ were extracted from the measured σ_{cc} using the Glauber Model framework [80]. The R_p determined from σ_{cc} for ^{16}O and ^{18}O are consistent with radii determined from the electron scattering. The systematic trend of R_p with increasing neutron number indicates minima at $N = 14$ and $N = 16$, that could be possible

signatures of shell closures at these neutron numbers. The appearance of the $N = 14$ gap between the $n(1d_{5/2})$ and $n(2s_{1/2})$ orbits in ^{22}O could be understood to arise from attractive monopole proton-neutron interaction between the spin-flip orbits $p(1p_{1/2})$ and $n(1d_{5/2})$. This causes lowering of these levels and therefore a decrease in R_p . The observed increase in R_p of ^{23}O is a result of its extended neutron density for the valence neutron in the $2s_{1/2}$ orbital with a closed-shell core of ^{22}O . The shell closure at $N = 16$ can be understood with the missing $T = 0$ monopole interaction between the $n(1d_{3/2})$ neutrons and $p(1d_{5/2})$ as the $p(1d_{5/2})$ orbit is vacant in oxygen isotopes.

A simultaneous reproduction of binding energies and radii in stable and neutron-rich nuclei is crucial for understanding the nuclear structure. We compared the measured data of R_p to the predictions of two different interactions from the χ EFT, EM [35] and $NNLO_{sat}$ interaction [36], calculated in different many-body *ab initio* approaches; Dyson SCGF (DGF), in-medium similarity renormalization group (IMSRG), Gorkov SCGF (GGF) calculations from Ref. [34] and the coupled-cluster calculation (CC) from Ref. [27]. The difference between the two interactions is that in $NNLO_{sat}$ interaction, the NN and $3N$ forces are optimized simultaneously in contrast to the EM interaction [35] in which the $3NF$ s are optimized subsequently. Another difference is that the determination of the low-energy coupling constants in the $NNLO_{sat}$ interaction includes data on the binding energies and radii of ^3H , $^3,^4\text{He}$, ^{14}C and ^{16}O isotopes whereas the EM interaction includes data on light elements ($A \geq 4$) only. The values of R_p predicted with a given interaction but calculated using different many-body approaches are somewhat similar. R_p of $^{19-24}\text{O}$ predicted by $NNLO_{sat}$ interaction are higher than the measured R_p whereas R_p predicted using EM interaction underestimate the measured R_p for all O isotopes. The relative isotopic trend of the proton radii calculated using the coupled-cluster computations clearly show the dips at $N = 14$ and $N = 16$, which are consistent with the evolutionary trend of the experimental proton radii.

We determined the neutron skin in neutron-rich oxygen isotopes using the measured R_p reported in this work and the measured R_m from Refs. [55, 56]. This first determination of the neutron skin of neutron-rich oxygen isotopes shows that neutron skin thickness rapidly increases from $^{22-24}\text{O}$, as N approaches the neutron drip-line. The experimental neutron skin of ^{24}O is significantly thicker than predicted by the

various *ab initio* models. The new data presented therefore provide valuable evidence on the cause of apparent new shell gaps in neutron-rich oxygen isotopes as well as the evolution of the neutron skin.

The R_p^{cc} data presented in this dissertation, therefore provided grounds for the further development of the *ab initio* theories and the interactions employed in the different calculations. In order to have a better understanding of the measured R_p^{cc} , our collaboration is undertaking new coupled-cluster calculations with the $NNLO_{sat}$ interaction. Further theoretical calculations are ongoing in our collaboration to determine the matter radii from the measured interaction cross-sections [55, 56] using the R_p^{cc} and the Glauber Model framework discussed in Ref [80]. These new matter radii will more accurately determine the neutron skin thickness in the oxygen isotopes.

Bibliography

- [1] G.Hans, “*On the Scattering of α -Particles by Matter*”. Proc. Roy. Soc. A. 81 546 (1908).
- [2] J. Chadwick, “*The existence of a neutron*” Proc. Roy. Soc. A 136 692 (1932).
- [3] H. Yukawa, “*On the Interaction of Elementary Particles. I*” Proc. Phys.Math. Soc. Jpn. 17, 48 (1935).
- [4] C. M. G. LATTES, “Processes involving Charged Mesons” Nature 159: 694-7, (1947).
- [5] CF Von Weizscker, “*Zur theorie der kernmassen*” Z. Phys. 96, 431 (1935).
- [6] Maria Goeppert Mayer, “*On Closed Shells in Nuclei. II*” Phys. Rev. 75, 1969 (1949).
- [7] O. Haxel, J. H. D. Jensen, and H. E. Suess, “*On the ”magic numbers” in nuclear structure*”, Phys. Rev., vol. 75, pp. 1766, (1949).
- [8] T.Otsuka “*Shell Structure of Exotic Nuclei.*” Lect. Notes Phys. 764, 1?25 (2009).
- [9] A. Ozawa et al., “*New Magic Number, $N = 16$, near the Neutron Drip Line*” Phys. Rev. Lett. 84, 5493 (2000).
- [10] R. Kanungo et al., “*Observation of new neutron and proton magic numbers*” Phys. Lett. B 528, 58 (2002).
- [11] I. Angeli et al., “ *N and Z dependence of nuclear charge radii*” Nucl. Part. Phys. 36 085102 (2009).
- [12] R. Kanungo et al., “*One-Neutron Removal Measurement Reveals ^{24}O as a New Doubly Magic Nucleus*” Phys. Rev. Lett. 102, 152501 (2009).
- [13] K. Tshoo et al., “ *$N = 16$ Spherical Shell Closure in ^{24}O* ” Phys. Rev. Lett. 109, 022501 (2012).
- [14] M.Langevin et al., “*Production of neutron-rich nuclei at the limits of particles stability by fragmentation of 44 MeV/u ^{40}Ar projectiles*” Phys. Lett. B 150, 71 (1985).
- [15] D. Guillemaud-Mueller et al., “*Particle stability of the isotopes ^{26}O and ^{32}Ne in the reaction 44 MeV/nucleon $^{48}\text{Ca} + \text{Ta}$* ” Phys. Rev. C 41, 937 (1990).
- [16] O. Tarasov et al., “*Search for ^{28}O and study of neutron-rich nuclei near the $N = 20$ shell closure*” Phys. Lett. B 409 64 (1997).

- [17] C. R. Hoffman et al., “*Determination of the $N=16$ Shell Closure at the Oxygen Drip Line*” Phys. Rev. Lett. 100, 152502 (2008).
- [18] E. Lunderberg et al., “*Evidence for the Ground-State Resonance of ^{26}O* ” Phys. Rev. Lett. 108, 142503 (2012).
- [19] Y. Kondo et al., “*Nucleus ^{26}O : A Barely Unbound System beyond the Drip Line*” Phys. Rev. Lett. 116, 102503 (2016).
- [20] I. Tanihata et al., “*Neutron halo nuclei*” J. Phys. G: Nucl. Part. Phys. 22, 157 (1996).
- [21] C. M. Tarbert et al., “*Neutron Skin of ^{208}Pb from Coherent Pion Photoproduction*” Phys. Rev. Lett. 112, 242502 (2014).
- [22] I. Tanihata et al., “*Revelation of thick neutron skins in nuclei*” Phys. Lett. B 289, 261 (1992).
- [23] J. Fujita and H. Miyazawa, “*Pion Theory of Three-Body Forces*” Prog. Theor. Phys. 17, 360 (1957).
- [24] T. Otsuka et al., “*Three-Body Forces and the Limit of Oxygen Isotopes*” Phys. Rev. Lett. 105, 032501 (2010).
- [25] E. Epelbaum et al., “*Modern theory of nuclear forces*” Phys. 81, 1773 (2009).
- [26] St Kistryn and E Stephan “*Deuteron?proton breakup at medium energies*” J. Phys. G: Nucl. Part. Phys. 40 063101 (2013).
- [27] G. Hagen et al., “*Continuum Effects and Three-Nucleon Forces in Neutron-Rich Oxygen Isotopes*” Phys. Rev. Lett. 108, 242501 (2012).
- [28] H. Hergert et al., “*Ab Initio Calculations of Even Oxygen Isotopes with Chiral Two-Plus-Three-Nucleon Interactions*” Phys. Rev. Lett. 110, 242501 (2013).
- [29] A. Cipollone et al., “*Isotopic Chains Around Oxygen from Evolved Chiral Two- and Three-Nucleon Interactions*” Phys. Rev. Lett. 111, 062501 (2013).
- [30] J. D. Holt et al., “*Chiral three-nucleon forces and bound excited states in neutron-rich oxygen isotopes*” Eur. Phys. J. A 49, 39 (2013).
- [31] A. Cipollone et al., “*Chiral three-nucleon forces and the evolution of correlations along the oxygen isotopic chain*” Phys. Rev. C 92, 014306 (2015).
- [32] G. R. Jansen et al., “*Ab Initio Coupled-Cluster Effective Interactions for the Shell Model: Application to ?Neutron-Rich Oxygen and Carbon Isotopes*” Phys. Rev. Lett. 113, 142502 (2014).
- [33] S. K. Bogner et al., “*Nonperturbative Shell-Model Interactions from the In-Medium Similarity Renormalization Group*” Phys. Rev. Lett. 113 142501 (2014).

- [34] V. Lapoux et al., “*Radii and Binding Energies in Oxygen Isotopes: A Challenge for Nuclear Forces*” Phys. Rev. Lett. 117, 052501 (2016).
- [35] D. R. Entem and R. Machleidt “*Accurate charge-dependent nucleon-nucleon potential at fourth order of chiral perturbation theory*” Phys. Rev. C 68, 041001(R) (2003).
- [36] A. Ekstrm et al., “*Accurate nuclear radii and binding energies from a chiral interaction*” Phys. Rev. C 91, 051301 (2015).
- [37] I. Angeli and K. Marinova, “*Table of experimental nuclear ground state charge radii: An update*” At. Data Nucl. Data Tables 99, 69 (2013).
- [38] J. L. Friar et al., “*Nuclear sizes and the isotope shift*” Phys. Rev. A 56, 4579 (1997).
- [39] R.Kanungo et al., “*A new view of nuclear shells*” Phys. Scr. T152 014002 (2013).
- [40] C.R. Hoffman et al., “*Evidence for a doubly magic ^{24}O* ” Phys. Lett. B 672 17 (2009).
- [41] T. Otsuka et al., “*Magic Numbers in Exotic Nuclei and Spin-Isospin Properties of the NN Interaction*” Phys. Rev. Lett. 87, 082502 (2001).
- [42] T.Otsuka et al., “*Evolution of Nuclear Shells due to the Tensor Force*” Phys. Rev. Lett. 95, 232502 (2005).
- [43] M. Stanoiu et al., “ *$N = 14$ and 16 shell gaps in neutron-rich oxygen isotopes*” Phys. Rev. C 69, 034312 (2004).
- [44] P.G. Thirolf et al., “*Spectroscopy of the 2_1^+ state in ^{22}O and shell structure near the neutron drip line*” Phys. Lett. B 485, 16 (2000).
- [45] A. Schiller et al., “*Selective population and neutron decay of the first excited state of semi-magic ^{23}O* ” Phys. Rev. Lett. 99 112501 (2007).
- [46] E. Becheva et al., “*The $N=14$ shell closure in ^{22}O viewed through a neutron sensitive probe*” Phys. Rev. Lett. 96 012501 (2006).
- [47] C. Rodriguez-Tajes “*One-neutron knockout from light neutron-rich nuclei at relativistic energies*” Phys. Rev. C 82, 024305 (2010).
- [48] D. Cortina-Gil et al., “*Shell Structure of the Near-Dripline Nucleus ^{23}O* ” Phys. Rev. Lett. 93, 062501 (2004).
- [49] Nociforo C et al., “*Coulomb breakup of ^{23}O* ” Phys. Lett. B 605 79 (2005).
- [50] Z. Elekes et al., “*Nuclear structure study of $^{19,20,21}\text{N}$ nuclei by spectroscopy*” Phys. Rev. C 82 027305 (2010).

- [51] P. Diaz Fernandez et al., . “*Quasifree (p,pN) scattering of light neutron-rich nuclei near $N = 14$.*” Phys. Rev. C 97 024311 (2018).
- [52] D. Sohler et al., “*In-beam γ -ray spectroscopy of the neutron-rich nitrogen isotopes $^{19-22}N$* ” Phys. Rev. C 77, 044303 (2008).
- [53] M.J. Strongman et al., “*Disappearance of the $N = 14$ shell*’ Phys. Rev. C 80, 021302(R) (2009).
- [54] C. X. Yuan et al., “*Shell evolution in neutron-rich carbon isotopes: Unexpected enhanced role of neutron-neutron correlation*” Nuc. Phys. A 883, 25 (2012).
- [55] A. Ozawa et al., “*Measurements of interaction cross sections for light neutron-rich nuclei at relativistic energies and determination of effective matter radii*” Nucl. Phys. A691, 599 (2001).
- [56] R. Kanungo et al., “*Exploring the anomaly in the interaction cross section and matter radius of ^{23}O* ” Phys. Rev. C 84, 061304 (2011).
- [57] R Hofstadter et al., “*Electron Scattering and Nuclear Structure*” Rev. Mod. Phys. 28, 214 (1956).
- [58] H. de Vries et al., “*Nuclear charge-density-distribution parameters from elastic electron scattering*” At. Data Nucl. Data Table 36 495 (1987).
- [59] F.-P. Juster, et al., “*Tritium Electromagnetic Form Factors*” Phys. Rev. Lett. 55 2261 (1985).
- [60] F.J. Kline, et al., “*Elastic electron scattering from ^{14}C* ” Nuclear Phys. A 209 381 (1973).
- [61] T. Ohnishi et al., “*The SCRIT electron scattering facility project at RIKEN RI beam factory*” Phys. Scripta T166, 014071 (2015).
- [62] K. Tsukada et al., “*First Elastic Electron Scattering from ^{132}Xe at the SCRIT Facility*” Phys. Rev. Lett. 118, 262501 (2017).
- [63] T. Suzuki et al., “*Neutron Skin of Na Isotopes Studied via Their Interaction Cross Sections*” Phys. Rev. Letters 75, 3241 (1995).
- [64] L.B Wang et al., “*Laser Spectroscopic Determination of the 6He Nuclear Charge Radius*” Phys. Rev. Letters 93, 142501 (2004).
- [65] P. Mueller et al., “*Nuclear Charge Radius of 8He* ” Phys. Rev. Let. 99, 252501 (2007).
- [66] R. Sanchez et al., “*Nuclear Charge Radii of $^{9,11}Li$: The Influence of Halo Neutrons*” Phys. Rev. Let. 96, 033002 (2006).

- [67] W. D. Nrtershuser et al., “Nuclear Charge Radii of ${}^7,9,10\text{Be}$ and the One-Neutron Halo Nucleus ${}^{11}\text{Be}$ ” Phys. Rev. Letters 102, 062503 (2009).
- [68] I. Tanihata et al., “Recent experimental progress in nuclear halo structure studies” Prog. Part. Nucl. Phys. 68, 215 (2013).
- [69] R. F. Garcia Ruiz et al., “Unexpectedly large charge radii of neutron-rich calcium isotopes” Nat. Phys. 12, 594 (2016).
- [70] R. Engfer, et al., “Charge-distribution parameters, isotope shifts, isomer shifts, and magnetic hyperfine constants from muonic atoms” At. Data Nucl. Data Table 14 509 (1974).
- [71] C. S. Wu and L. Wilets *Muonic atoms and nuclear structure* Annu. Rev. Nucl. Sci. 19, 527 (1969).
- [72] G. Fricke, et al., “Nuclear ground state charge radii from electromagnetic interactions” At. Data Nucl. Data Table 60 177 (1995).
- [73] P. Strasser, et al., “Muon spectroscopy with trace alkaline-earth and rare-earth isotopes implanted in solid D_2 ” Hyperfine Int. 193 121 (2009).
- [74] W.R.Webber et al., “Individual charge-changing fragmentation cross sections of relativistic nuclei in hydrogen, helium, and carbon targets” Phys. Rev. C 41 520 (1990) .
- [75] J.R.Cummings et al., “Determination of the cross sections for the production of fragments from relativistic nucleus-nucleus interactions. I. Measurements” Phys Rev. C 42, 2508 (1990).
- [76] B. Blank et al., “Charge-changing cross sections of the neutron-rich isotopes ${}^{8,9,11}\text{Li}$ ” Z. Phys. A - Hadrons and Nuclei 343, 375 (1992).
- [77] L. V. Chulkov et al., “Total charge-changing cross sections for neutron-rich light nuclei” Nucl. Phys. A 674, 330 (2000).
- [78] R. J. Glauber “Lectures in Theoretical Physics” vol.1, ed.W. E. Brittin et al. (New York,1959).
- [79] P. J. Karol, “Nucleus-nucleus reaction cross sections at high energies: Soft-spheres model” Phys. Rev. C 11, 1203 (1975).
- [80] Y. Suzuki et al., “Parameter-free calculation of charge-changing cross sections at high energy” Phys. Rev. C 94 011602 (2016).
- [81] B. Abu-Ibrahim et al., “Reaction cross sections of carbon isotopes incident on a proton” Phys. Rev. C 77, 034607 (2008).

- [82] A. Estrade et al., *Proton Radii of $^{12-17}\text{B}$ Define a Thick Neutron Surface in ^{17}B* Phys. Rev. Lett. 113, 132501 (2014).
- [83] T. Yamaguchi et al. “*Scaling of Charge-Changing Interaction Cross Sections and Point-Proton Radii of Neutron-Rich Carbon Isotopes*” Phys. Rev. Lett.107, 032502 (2011).
- [84] R. Kanungo et al. “*Proton Distribution Radii of $^{12-19}\text{C}$ Illuminate Features of Neutron Halos*” Phys. Rev. Lett. 117, 102501 (2016).
- [85] S.Bagchi et al., “*Evidence of the $N = 14$ shell gap and neutron skin found from measured proton radii of neutron-rich nitrogen isotopes*” Preprint submitted to Physics Letters B
- [86] H. Geissel et al., “*The GSI projectile fragment separator (FRS): a versatile magnetic system for relativistic heavy ions*” Nucl. Instr. and Meth., B 70, 286 (1992).
- [87] R. Kanungo et al., “*Determination of proton radii and neutron skin thickness of p - sd shell nuclei by charge-changing Cross Section measurement*” GSI experiment S395 proposal, (2011).
- [88] <https://www-win.gsi.de/frs-setup/images/SISTAQ2.gif>
- [89] D. Bazin et al., “*The program LISE: a simulation of fragment separators*” Nucl. Instr. Meth. Phys. Res. A 482 307327 (2002).
- [90] G.R. Satchler “*Introduction to Nuclear Reactions Macmillan*” London (1980).
- [91] A. Stolz et al., “*Projectile fragmentation of ^{112}Sn at $E = 1 \text{ A GeV}$ ” Phys. Rev. C 65, 064603 (2002).*
- [92] S. P. Ahlen, “*Theoretical and experimental aspects of the energy loss of relativistic heavily ionizing particles*” Rev. Mod. Phys. 52 121 (1980).
- [93] V. Hlinka et al., “*Time Projection Chambers for tracking and identification of radioactive beams*” Nucl. Instrum. Meth. Phys. Res., Sect. A 419, 503 (1998).
- [94] R. Janik et al., “*Time Projection Chambers with C-pads for heavy ion tracking*” Nucl. Instr. Meth. Phys. Res. A 640 54, (2011).
- [95] B. Voss et al. “*The scintillation-detector equipment of the GSI projectile-fragment separator*” Nucl. Instr. Methods Phys. Res. A 364 150 (1995).
- [96] A. Ozawa et al., “*Nuclear size and related topics*” Nucl. Phys. A 693, 32 (2001)
- [97] B.A. Brown et al., “*The charge distributions of the oxygen and calcium isotopes.*” Phys. Lett. 85B 167 (1979).